UNIVERSITY OF NOVA GORICA
GRADUATE SCHOOL

OPTIMIZATION OF AERODYNAMIC SURFACES USING PRESSURE BASED FUNCTIONALS

DISSERTATION

Matej Andrejašič

Mentor: Assoc. Prof. Gregor Veble

Nova Gorica, 2014

UNIVERZA V NOVI GORICI
FAKULTETA ZA PODIPLOMSKI ŠTUDIJ

OPTIMIZACIJA AERODINAMSKIH POVRŠIN S POMOČJO TLAČNIH FUNKCIONALOV

DISERTACIJA

Matej Andrejašič

Mentor: Izr. Prof. Gregor Veble

Nova Gorica, 2014

To Petra and Iza, my life

Acknowledgement

I would like to express my deepest gratitude to my mentor, Assoc. Prof. Gregor Veble, who has been a faithful source of encouragement, wisdom and support throughout my research work. I would also like to thank the company of Pipistrel d.o.o. Ajdovščina for the opportunity to join a group of such a smart, hard working and good people and for all the technical support given. Special thanks go also to Damjan Zabovnik and the company of Seaway who were kind enough to provide me with the geometries for the case studies.

I would sincerely like to thank my wife Petra and our daughter Iza for all the support and patience during my studies and writing this thesis. I couldn't have done it without you. Finally, I would like to thank my parents for their continuous encouragement and understanding and everybody else who helped me to realize this work.

The work was partly financed by the European Union, European Social Fund (Junior Researchers).

Abstract

A panel based method for automatic optimization of aerodynamic surfaces using pressure based functionals is presented, where a potential flow is used as a valid approximation of the attached flow passing an arbitrary body. The optimization is performed subject to the Stratford separation criterion and geometrical constraints, where a favourable pressure distribution that indirectly leads to a reduced drag represents the solution. The minimization of functionals is done using a sequential quadratic programming algorithm. The method is simple and has low computational demands. Its efficiency is demonstrated in three conceptually different test cases. In case of an optimization of a fairing, enclosing a human powered bicycle, the drag is reduced through a postponement of the transition from laminar to turbulent flow and the thinning of the boundary layer in the pressure recovery region. In case of a fairing of a wing-fuselage junction on an airplane, a minimal drag at the same amount of lift is obtained through an elimination of a massive root flow separation at moderate angle of attack, and in case of an optimization of a bulb keel of a sailboat, a favourable pressure distribution and consequently reduced drag is obtained simply through a smoother and on average slower flow passing the optimized surfaces.

Key words: aerodynamics, numerical optimization, pressure based functional, panel method, favourable pressure distribution, Stratford criterion, laminar-turbulent transition, pressure drag, viscous drag, boundary layer.

Povzetek

V doktorski disertaciji je predstavljena metoda za avtomatično optimizacijo aerodinamskih površin s pomočjo tlačnih funkcionalov. Metoda temelji na panelni metodi za izračun tlačnih porazdelitev, kjer je potencialni tok uporabljen kot veljaven približek prilepljenega toka, ki obteka poljubno telo. V metodi je vključen tudi Stratfordov odcepitveni kriterij ter geometrijske omejitve, njen rezultat pa je ugodna porazdelitev tlaka, ki posredno nakazuje na zmanjšanje upora telesa. Za minimizacijo funkcionalov je uporabljen SQP algoritem. Metoda je enostavna in zahteva malo procesorske moči. Zmogljivost metode je prikazana na treh različnih testnih primerih. Pri optimizaciji zunanje lupine vozila na človeški pogon se upor zmanjša zaradi premika laminarno-turbulentnega prehoda proti koncu telesa in zaradi stanjšanja mejne plasti v območju tlačnega okrevanja. Pri drugem testnem primeru, optimizaciji prehoda krila na trup letala, je minimalni upor pri isti velikosti vzgona pri srednje velikih vpadnih kotih dosežen z eliminacijo odcepljenega toka na korenu krila. Pri zadnjem testnem primeru, optimizaciji kobilice jadrnice, pa izračunana ugodna porazdelitev tlaka vpliva na zmanjšan upor posredno preko enakomernejše in v povprečju počasnejše porazdelitve hitrosti.

Ključne besede: aerodinamika, numerična optimizacija, tlačni funkcional, panelna metoda, ugodna porazdelitev tlaka, Stratfordov odcepitveni kriterij, laminarno-turbulentni prehod, tlačni upor, viskozni upor, mejna plast.

Contents

Nomenclature

Latin symbols

a_0 = Stratford number "soft" maximum parameter
$a_{1,2}$ = Stratford number parameters
b = bias number
B = Bernstein polynomial
c = chord length, m
c_f = local skin friction drag coefficient
C_D = drag coefficient
C_{D_f} = skin friction drag coefficient
C_{D_p} = pressure drag coefficient
C_p = pressure coefficient
C_p' = canonical pressure coefficient
C_L = lift coefficient
$\boldsymbol{d}$ = deformation vector field, m
F = cost function
$\boldsymbol{f}$ = external specific force, N/kg
G = Stratford number
G_M = Stratford number “soft” maximum
$\boldsymbol{g}$ = spatial vector, m
h = Bézier surface value
I = turbulence intensity
k = optimization variable
l = reference body length, m
L = lift, N
M = Mach number
N = number of surface panels
N_C = number of cells

$\boldsymbol{n}$ = surface normal vector, m
p = pressure, Pa
P = an arbitrary point in space
R = sphere radius, m
Re = Reynolds number
Re_c = Reynolds number, based on the length c
$Re_{x'}$ = Reynolds number, based on the length x'
$\boldsymbol{r}$ = position vector, m
S = surface, m^2
St = Strouhal number
$\boldsymbol{s}$ = integration path, m
t = time, s
T = reference time, s
u, v = surface coordinates
V_s = velocity of sound, m/s
$\boldsymbol{V}$ = velocity vector, m/s
$\mathcal{V}$ = volume, m^3
x, y, z = Cartesian coordinates, m
x' = effective length of the boundary layer, m
x_m = the beginning of the pressure recovery, m
w = weight

Greek symbols

α = angle of attack, °
β = turbulent viscosity ratio
γ = vortex distribution, m/s
Γ = circulation, m^2/s
δ = boundary layer thickness, m
ζ = vorticity vector, /s
μ = doublet strength, m^2/s
ν = kinematic viscosity, m^2/s
ρ = density, kg/m^3
σ = sink/source strength, m^3/s
τ_w = wall shear stress, Pa

Φ = velocity potential, m^2/s

Φ_i = internal velocity potential, m^2/s

ω = inverse turbulent time-scale, /s

ω' = angular velocity, /s

Ω = solid angle

Subscripts

AN = analytical

B = body

D = doublet

lam = laminar

low = lower

max = maximal value

min = minimal value

new = new value

old = old value

opt = optimal

$orig$ = original

S = source

$turb$ = turbulent

TE = trailing edge

up = upper

U = uniform

x, y, z = x, y, z direction

W = wake

∞ = freestream

Superscripts

$\dagger$ = dimensionless

$*$ = perturbation

Acronyms

ec = equality constraints

lb = lower optimization variable boundary, m

nec = nonequality constraints

RHS = right hand side of an equation

ub = upper optimization variable boundary, m

Chapter 1

Introduction

Automatic aerodynamic optimization is an ongoing field of research. It couples the fields of computational fluid dynamics (CFD) and numerical optimization. In order to obtain an optimal aerodynamic shape (e.g. at minimal drag), many flow computations are needed. A lower degree of a CFD method complexity therefore results in a faster and more practical optimization method. Furthermore, a simpler method typically focuses on only certain aspects of the flow (e.g. laminar-turbulent transition), which helps to focus the optimization process.

The use of calculus of variations, which is the basis of all modern aerodynamic optimization methods, for the optimal aerodynamic shape design was explored already in 1965 by Miele [1]. Its application in optimal control theory for control of systems governed by partial differential equations [2] was later used in compressible potential flow problems [3]. Independently it was also used in aerodynamic design via CFD by Jameson [4] who proposed to treat the design problem as a control problem in which the control is the shape of the boundary.

A class of methods developed to study the design of nonplanar wing surfaces concerns mostly the study of induced drag by analysing the vorticity distribution in the Trefftz plane, a virtual plane far enough downstream from the body [5]. Such methods are also suitable for multidisciplinary approaches where further aspects such as structural weight and viscous drag are taken into account [6–8].

Another class of methods deals with a problem of studying the two dimensional airfoil sections [9, 10] and optimizing them for best drag at given lift. These sections can then form the basis of more complex wing analyses.

The largest amount of work has been dedicated to optimization of full three dimensional aerodynamic configurations. Some of the studies are presented and described in overview papers [11–13]. A number of studies [14–17] focus on the full set of Navier-Stokes equations, devising methods for the calculation of ideal shapes, and often also taking into account structural considerations. These studies require significant computational resources. A simplification of the fluid model is therefore often desirable, and work has been done in employing the nonviscous, Euler equations in the transonic regime [18–21]. A further reduction in the fluid model can be performed by using potential based methods, such as the panel method [22–27] which is a class of boundary element methods (BEM) [28–30]. Since a volume mesh surrounding the aerodynamic surface is at the panel method replaced by a surface mesh, the problem is simplified and the optimization procedure accelerated significantly. In such studies, drag is estimated using the boundary layer equations via pressure distributions as supplied from the potential flow. The fluid model can be reduced even further by using a meshless method of fundamental solution (MFS) which shows prominent results for potential flows [31–33]. But since the surface of the body being optimized still needs to be discretized in order to be able to reshape, the MFS method is not very practical from the surface optimization point of view.

In all optimization methods, once the fluid model is chosen, an optimization of a cost function can be performed using various minimization schemes [34]. Most commonly, schemes that require a calculation of a gradient of a cost function with respect to surface parameters are applied, such as the quasi-Newton method. The gradients can be calculated by direct numerical differentiation, however, many studies employ the so called adjoint formulation, where the gradients can be computed via a calculation of additional flow equations that correspond to surface perturbations [14,18–20]. On the other hand, the calculation of gradients can be avoided by choosing a method that only requires the calculation of the functional itself. In recent years, genetic algorithms are gaining prominence [16].

The regime of interest of the present work is a low Mach number ($M < 0.3$), moderate to high Reynolds number ($10^6 \leq Re \leq 10^7$) type of flow. In this regime, the flow can be considered incompressible. For well designed aerodynamic surfaces, the flow can be also well separated into the essentially inviscid region away from the aerodynamic surface, with viscous effects being dominant only in the thin boundary layer close to the surface (on the order of hundredths of the typical dimension in this regime), and in the (thin) wake behind the surface. The external flow outside the boundary layer and the wake can be therefore described by one of the potential flow methods, the most prominent of these being the panel method. The boundary layer flow is then dominated by the inviscid external pressure distribution and, if there is no separation of flow present, the boundary layer only loosely affects the external flow by increasing the effective thickness of the present aerodynamic surface [35].

The main idea behind the present work is that the calculation of the boundary layer may not be necessary for obtaining a low drag aerodynamic shape. As the boundary layer flow is driven by the pressure distribution, one can tailor pressure distribution directly in order to promote good boundary layer behaviour. The problem can therefore be transferred from the direct calculation of drag using boundary layer equations towards designing pressure functionals which, when minimised, will give pressure distributions that promote favourable boundary layer flows.

For two dimensional airfoils, a successful pressure functional that minimizes the integral of the absolute value of the pressure gradient has already been employed [9]. A similar formulation, that depends on a surface pressure distribution and a surface gradient of this distribution, is in present work extended to three dimensional shapes. In order to obtain pressure distributions across the aerodynamic surface, in-house panel method codes were developed on the basis of a constant doublet singularity surface distribution. The trade-off between accuracy and simplicity was sought. The minimization of the functionals was done using sequential quadratic programming (SQP) algorithms, which are considered to be among the most efficient methods for solving nonlinear constraint optimization problems [36, 37].

The main result of the present work is therefore a fast and practical method for optimization of three dimensional low speed aerodynamic shapes. A novel approach towards aerodynamic optimization employs a fully inviscid formulation that promotes efficient boundary layer flow, even though an information about the actual boundary layer flow is deliberately lost. This approach is consistent with the typical task of an aerodynamic designer, where surface pressure distributions are tailored manually in order to obtain smoothly varying flows.

The theory that lies behind the proposed surface optimization method is described in Chapter 2. The method itself is presented in Chapter 3, which is divided into two main components for the present work, the panel method and the surface optimization. In Chapter 4, the method is tested on three fundamentally different examples, such as a fairing of a human powered vehicle, a fairing of a wing-fuselage junction at the airplane and two fairings (hull-fin and fin-bulb) at the keel of a sailboat. The results are validated with full Reynolds averaged

Navier-Stokes (RANS) calculations.

Chapter 2

Theory

2.1 Potential Flow

A fixed finite control volume with a constant volume and surface area submerged in a flow field with density distribution ρ is considered first. Since the flow is moving through the control volume the time rate of change of mass and momentum can be observed in it. If the conservation of mass and Newton's second law is applied to the control volume and transformed to differential form, the *continuity equation* is written as

$$\frac{\partial \rho}{\partial t} + \nabla \cdot \rho \mathbf{V} = 0 \tag{2.1}$$

and the full *Navier-Stokes equation* as

$$\rho \left(\frac{\partial \mathbf{V}}{\partial t} + \mathbf{V} \cdot \nabla \mathbf{V} \right) = \rho \boldsymbol{f} - \nabla p + \rho \nu \nabla^2 \mathbf{V} + \frac{1}{3} \rho \nu \nabla (\nabla \cdot \mathbf{V}). \tag{2.2}$$

The continuity equation states that the mass can neither be created nor destroyed or in other words the mass must be conserved. The momentum equation on the other hand describes the time rate of change of momentum due to the sum of all forces acting on observed control volume. The Navier-Stokes equation (Eq. (2.2)) is written in Cartesian coordinates and in this form holds true for Newtonian fluids only. These two statements, together with the equation of state, present the fundamental equations of aerodynamics and allow us to describe any kind of motion of a Newtonian fluid.

The present work applies to the regime of high *Reynolds number*

$$Re = \frac{lV}{\nu} \tag{2.3}$$

and low *Mach number*

$$M = \frac{V}{V_s} \tag{2.4}$$

flows ($10^6 \leq Re \leq 10^7$ and $M < 0.3$ for the typical cases presented in this work), where l and V_s represent a reference body length and the velocity of sound, respectively. Low Mach number indicates that we are dealing with incompressible flow where density doesn't change with time and space. The continuity equation (Eq. (2.1)) for incompressible or constant density fluid can therefore be written as

$$\nabla \cdot \mathbf{V} = 0. \tag{2.5}$$

High Reynolds numbers, as it will be shown next, enables one to neglect the viscous effects in the outer region of the flow. The Navier-Stokes equation for incompressible flow and without body forces can be written in dimensionless form as

$$St\frac{\partial \mathbf{V}^\dagger}{\partial t^\dagger} + \mathbf{V}^\dagger \cdot \nabla^\dagger \mathbf{V}^\dagger = -\nabla^\dagger p^\dagger + \frac{1}{Re}\nabla^{\dagger 2}\mathbf{V}^\dagger, \tag{2.6}$$

where the dimensionless characteristic quantities used are $\nabla^\dagger = l\nabla$, $\mathbf{V}^\dagger = \mathbf{V}/V_\infty$, $t^\dagger = t/T$ and $p^\dagger = p/\rho V_\infty^2$, where V_∞ represents a freestream velocity magnitude. The ratio between inertial and viscous forces is presented by the freestream Reynolds number $Re = V_\infty l/\nu$ and the importance of time-dependent phenomena by a form of the Strouhal number $St = l/TV_\infty$.

All the terms in Eq. (2.6) are of order of one except the last term on the right hand side of equation, which is for high Reynolds numbers negligible compared to the other terms. In regions further away from solid boundaries, where velocity approaches the freestream velocity V_∞ of undisturbed flow, shear stress derivative is of the order of one ($\nabla^{\dagger 2}\mathbf{V}^\dagger \approx 1$) and for high Reynolds numbers this viscous term can be neglected. In thin layer adjacent to body surface (Fig. (2.1)), on the other hand, the shear stress derivative can be quite substantial and the viscous term in Eq. (2.6) becomes comparable to the other terms and can't be neglected even for high Reynolds numbers.

Consequently, there are two distinctive regions surrounding the body in high Reynolds number flows [38]. In the immediate vicinity of the body there is a thin *boundary layer*, where the viscous effects play a significant role in flow development. In this region boundary layer equations [35] need to be solved in order to obtain the shear stress distribution and corresponding friction forces. Since the viscous effects are effectively confined in this thin boundary layer, the

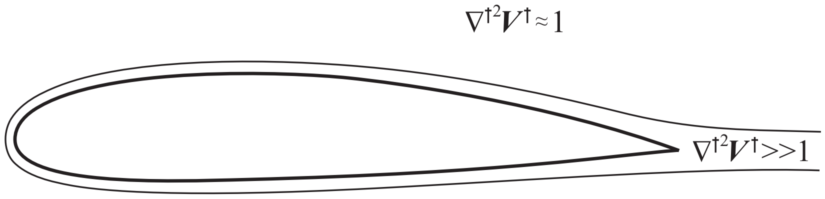

Figure 2.1: High Re attached flow around an arbitrary body can be approximated by two distinctive regions: a boundary layer with characteristic viscous effects and an outer potential flow region.

flow further away from the solid surface is said to be viscous free. The flow in this *outer region* can therefore be described with incompressible and inviscid aerodynamic equations whose solution provides a pressure distribution on the boundary of the region. The same pressure distribution is felt by the observed body since for attached flows an assumption can be made that the pressure doesn't change across the boundary layer [35].

A high-Reynolds number approximation is a valid assumption for numerous problems such as low speed aerodynamics in general aviation, hydrodynamics of marine vessels, etc. It simplifies the flow description and allows one to obtain a pressure distribution on a body surface with less difficulty than does a Navier-Stokes solution. Another important aspect to be considered is rotation of the flow. A simplification of the flow description in the outer region, that will be introduced next, allows one to write the aerodynamic equations in a form that will be used through the remainder of present work.

As a consequence of velocity variations within the fluid, each fluid element experiences translation, rotation and deformation while moving with the flow. Its rotation can be effectively described by vorticity vector, which is defined through angular velocity vector as

$$\zeta = 2\omega' = \nabla \times \mathbf{V}. \tag{2.7}$$

When fluid elements rotate while moving with the flow, the flow is considered to be *rotational* or $\nabla \times \mathbf{V} \neq 0$. On the other hand, after Kelvin's theorem [22]

$$\frac{D\Gamma}{Dt} = 0, \tag{2.8}$$

which states that the time rate of change of circulation Γ around a closed curve consisting of the same fluid elements is zero, previously nonrotating ideal fluid elements can not start rotating in the region of negligible viscous forces. This kind of flow is called *irrotational* and can be described by expression

$$\zeta = \nabla \times \mathbf{V} = 0 \tag{2.9}$$

The flow in the outer inviscid region can be therefore denoted as irrotational where Eq. (2.9) holds true. Since a curl of a gradient of any scalar function is identically zero, we can write the velocity vector as a gradient of a *velocity potential* Φ as

$$\mathbf{V} = \nabla\Phi, \tag{2.10}$$

where

$$\mathbf{V} = (V_x, V_y, V_z) = (\frac{\partial\Phi}{\partial x}, \frac{\partial\Phi}{\partial y}, \frac{\partial\Phi}{\partial z}). \tag{2.11}$$

Since an irrotational flow can be described by velocity potential, it is also called a *potential flow.*

The incompressible continuity equation (Eq. (2.5)) for an irrotational fluid can be further written as

$$\nabla \cdot \mathbf{V} = \nabla \cdot \nabla\Phi = \nabla^2\Phi = 0. \tag{2.12}$$

This linear elliptical differential equation is *Laplace's equation*, whose solution is a potential field. Once the velocity distribution is calculated from Eq. (2.10), the pressure distribution on body surface needs to be obtained in order to calculate the aerodynamic forces and moments.

In order to do that, the incompressible, inviscid and steady Navier-Stokes equation without body forces needs to be rewritten with the help of equation

$$\mathbf{V} \cdot \nabla\mathbf{V} = \nabla\frac{V^2}{2} - \mathbf{V} \times \zeta \tag{2.13}$$

as

$$-\mathbf{V} \times \zeta + \nabla\frac{V^2}{2} = -\nabla\frac{p}{\rho}. \tag{2.14}$$

For an irrotational flow ($\zeta = 0$) Eq. (2.14) can be further simplified to

$$\nabla\left(\frac{V^2}{2} + \frac{p}{\rho}\right) = 0, \tag{2.15}$$

which holds true for a steady flow only if the expression in the parentheses is a spatial constant

$$\frac{V^2}{2} + \frac{p}{\rho} = \text{const.} \tag{2.16}$$

The derived equation is called a *Bernoulli's equation.* It connects magnitude of velocity and pressure of every point in the flow, which enables one to compute the pressure distribution directly from the velocity distribution. By comparing Eq. (2.16) at two points in the flow, where one is at infinity, the following expression for pressure coefficient holds true

$$Cp = \frac{p_\infty - p}{\frac{1}{2}\rho V_\infty^2} = 1 + \frac{V^2}{V_\infty^2}. \tag{2.17}$$

2.2 Drag

All aerodynamic forces and moments a body situated in a fluid flow experiences have two root causes:

- pressure surface distribution and
- shear stress surface distribution.

The fluid moving along a solid boundary acts on the body solely through these two mechanisms. Both distributions represent an average force distribution per unit area. The pressure distribution represents a normal stress with forces oriented normal to the body surface, whereas shear stress acts tangential to the body surface. By integrating them over the whole body surface, total force and moment acting on the body can be obtained. The force can be further resolved into two components, one in direction of a freestream called a *drag*, and one in direction perpendicular to the freestream called a *lift*.

There are three contributions to a total drag force: *pressure drag*, *skin friction drag* due to shear stress, and *induced drag* due to lift. In this work we are interested only in the first two contributions, even though induced drag can have a major contribution to total drag in some cases, e.g. an airplane on take-off [39].

According to d'Alembert's paradox [40], a completely attached inviscid flow passing a nonlifting body with an arbitrary shape doesn't cause drag on the body. This can be observed by taking into consideration only the outer region of the flow described by the potential theory (Section 2.1). As soon as viscosity in the boundary layer is taken into consideration, viscous effects produce skin friction and possibly also flow separation which together always produce a finite drag.

A no-slip condition at the body surface, due to a frictional force between the surface and the fluid, causes a retarded flow right above the surface. In the region of an adverse pressure gradient it can happen that the flow, already slowed down by the frictional forces, may no longer sustain an increasing pressure. The flow can stop or even reverse its direction and start moving upstream (Fig. (2.2(a))), which causes the flow to separate from the surface and create a large wake of recirculating flow behind the body. At the region of separated flow the pressure drops (Fig. (2.2(b))) and can therefore no longer cancel the pressure distribution over the reminder of the body. A result is a pressure drag force due to a flow separation. A separated flow should be avoided since besides a large drag, it produces also a major lift decrease or even a stall.

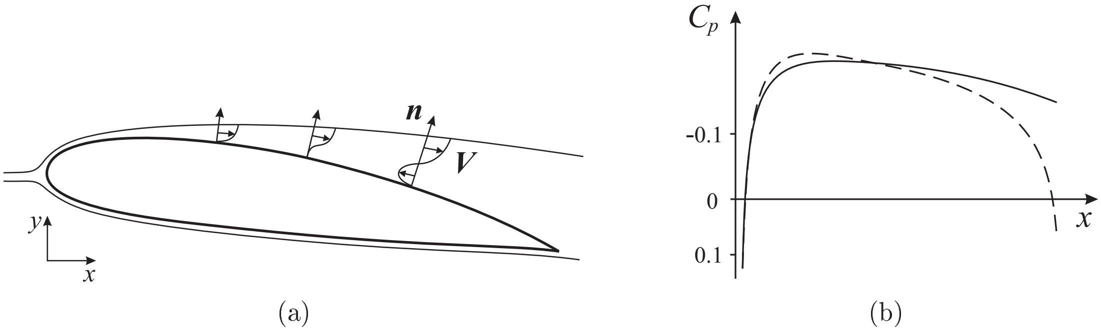

Figure 2.2: (a) Boundary layer velocity profiles of a separated flow, due to adverse pressure gradient. (b) Pressure distribution on the upper side of the airfoil of an attached (dashed) and separated flow (solid).

Over the range of Reynolds number between 10^6 and 10^7, where the main interest of the present work lies, the external flow passing a slender body usually experiences a laminar to turbulent boundary layer transition. Since a laminar boundary layer has smooth and regular streamlines, whereas the motion of a flow in a turbulent boundary layer is very irregular and full of vertices of all sizes, the two flows have different characteristics and produce a different amount of drag.

Because of a high diffusivity of a turbulent boundary layer, the fluid elements with higher velocity can approach the surface closer and the elements with smaller velocity can digress further away from the surface. Turbulence therefore produces an exchange of momentum and energy which thickens the boundary layer. A flat plate at a zero incidence has a thickness of a laminar boundary layer according to H. Blasius [41] proportional to the square root of a distance x along the plate and inversely proportional to the square root of the Reynolds number (based on the length of the plate c)

$$\delta_{lam} = 5.0c^{1/2}\frac{x^{1/2}}{Re_c^{1/2}}. \tag{2.18}$$

This result presents an exact solution of the L. Prandtl's laminar boundary layer equations [38]. On the other hand, there is no pure theory to describe a turbulent boundary layer. The thickness of the turbulent boundary layer is therefore given approximately by [40]

$$\delta_{turb} = 0.37c^{1/5}\frac{x^{4/5}}{Re_c^{1/5}}. \tag{2.19}$$

The boundary layer thickness δ is in these cases defined as a distance from the solid surface to the point in the flow in surface normal direction $\mathbf{n}$, with a velocity magnitude equal to 99% of the freestream velocity V_∞ (Fig. (2.3)). For the example of a flat plate at zero incidence the relation $\delta_{turb} > \delta_{lam}$ indeed holds true for every x along the plate.

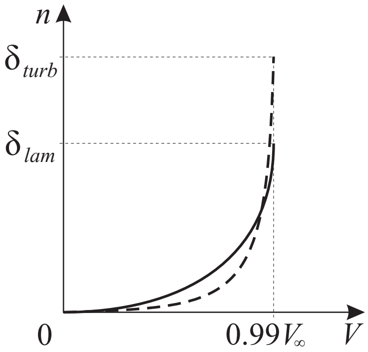

Figure 2.3: A typical velocity profile in a laminar (solid) and a turbulent boundary layer (dashed) and corresponding boundary layer thicknesses.

A high degree of mixing of fluid elements in turbulent boundary layer also produces different velocity profiles adjacent to the body surface compared to the laminar flow. A typical velocity profile in boundary layer before and after transition is presented in Fig. (2.3). The turbulent boundary layer has a larger velocity gradient $(\partial V/\partial n)_{n=0}$ at the wall than laminar boundary layer [35] and since a shear stress of a Newtonian fluid is directly proportional to the velocity gradient

$$\tau_w = \rho\nu\left(\frac{\partial V}{\partial n}\right)_{n=0}, \tag{2.20}$$

also the frictional stress is greater for turbulent boundary layer. By integrating the skin friction coefficient $c_f = \tau_w/\frac{1}{2}\rho_\infty V_\infty^2$ over the complete surface of the body, the friction drag coefficient of the body can be calculated. In the case of a flat plate with a length c at zero incidence in a laminar boundary layer, the friction drag can be expressed after [41] as

$$C_{D_{f,lam}} = \frac{1.328}{Re_c^{1/2}}, \tag{2.21}$$

and for a plate in a turbulent boundary layer after [40] approximately as

$$C_{D_{f,turb}} = \frac{0.074}{Re_c^{1/5}}. \tag{2.22}$$

The friction drag of turbulent boundary layer can be therefore much larger than the friction drag of laminar boundary layer, in case of an attached flow passing an arbitrary body. Due to mixing and the associated momentum transfer the average flow velocity near the body surface is higher for turbulent flow. Fluid elements of a turbulent flow near the body surface have more energy and can better overcome skin friction and therefore withstand larger adverse pressure gradients. For this reason the turbulent flow doesn't separate from the surface as readily as laminar flow. If the flow does eventually separate, the separated region is smaller for the turbulent flow and consequently the pressure drop less explicit [35]. The pressure drag of the separated turbulent boundary layer is therefore smaller than the pressure drag of the separated laminar boundary layer.

It depends on the shape of the body or the part of the body what kind of flow is preferred. If the body is blunt, laminar flow causes large laminar bubbles [42] that lead to flow separation and consequently large pressure drag. For blunt bodies turbulent flow is desired, whereas for slender bodies usually laminar flow is preferable since its friction drag component is larger than its pressure drag component. If there is a chance the flow will separate, e.g. at the pressure recovery region, the transition from laminar to turbulent flow should occur right before the separation. In this way, in order to achieve the smallest drag possible, laminar flow with smaller skin friction is preferred in the region of favourable pressure gradient, where the flow is usually attached, and a turbulent flow with smaller pressure drag in the pressure recovery region.

Laminar-Turbulent Transition. An exact laminar to turbulent flow transition location is not a trivial thing to predict, since it is affected by many parameters such as Reynolds number, pressure distribution of the outer flow, the roughness of the wall, the turbulence intensity of the outer flow, etc. In fact, the transition doesn't happen at a point but over a region of a finite length. Any real flow is in one way or another subject to smaller or bigger disturbances and the viscosity is the factor that acts to restrain produced instabilities. Above a certain limit of the Reynolds number, the inertial forces are so large in relation to the viscous ones that the disturbances are not sufficiently damped and will start to grow. The transition process starts and the flow goes through different stages before it becomes a completely turbulent flow. The transition is most noticeable by a great increase in the boundary layer thickness and in the wall shear stress (Eqs. (2.18) - (2.22)).

A transition that starts with two dimensional *Tollmien-Schlichting waves* that are superimposed on the laminar flow is called a *natural transition* [35]. The basic laminar flow is therefore distorted by the growth of the unstable two dimensional primary instabilities that get amplified downstream in the boundary layer and eventually transform into three dimensional secondary instabilities that lead to Λ-*structure formations*. These are replaced by *turbulent spots*, which are the last phase before the fully turbulent boundary layer develops.

If the amplitude of the turbulence intensity in the freestream is larger than the amplitude of the two dimensional primary instabilities at the natural transition, this beginning phase of the transition can be by-passed. In case of an intense freestream turbulence or even high degree of surface roughness, the transition starts directly with three dimensional secondary instabilities or even with turbulent spots. This type of transition is called a *by-pass transition* [43–45].

In order to postpone the transition and consequently reduce the drag of the body, the likelihood for the formation of the instabilities in the flow should be as low as possible. The *stability theory* of a laminar flow states that the curvature of the velocity profile at the body surface is the crucial factor for the stability of the laminar flow [35]. According to the boundary layer equation at the wall [35]

$$\rho\nu\left(\frac{d^2V}{dn^2}\right)_{n=0}=\frac{dp}{dx}, \tag{2.23}$$

the pressure gradient directly controls the curvature of the velocity profile and therefore considerably influences the stability of the laminar flow. A negative pressure gradient can lower the amount of instabilities in the flow and postpone the transition, whereas a positive pressure gradient can not only strongly amplify the disturbances but even initiate the transition. Streamwise instabilities that lead to Tollmien-Schlichting waves can be therefore controlled by using a favourable pressure gradient and by minimizing the extent of the pressure recovery region.

If the direction of pressure gradient is inclined at an angle with respect to the freestream direction, the boundary layer and the outer region will try to follow different paths. If there is a rather large angle between the two directions, the *cross-flow* instabilities can occur in the boundary layer that can, similar to Tollmien-Schlichting waves, begin the transition process. A typical example of this phenomenon is a swept wing or a rotating disk [46, 47]. In order to avoid cross-flow instabilities, the strong pressure gradient component in direction perpendicular to the freestream should be minimized. This is another instability source that can be controlled by using a suitable pressure gradient.

Both contributions of drag, pressure drag due to flow separation and skin friction drag due to shear stress, are a consequence of viscosity of the fluid. Even though the potential flow doesn't produce drag, the potential flow theory can still be used to indirectly influence on the amount of drag through pressure distribution (as was shown in the present section), which presents the base of the surface optimization method in the present work.

2.3 Solution of Laplace's Equation

In order to compute a pressure distribution caused by the potential flow passing an arbitrary body, Laplace's equation (Eq. (2.12)), a second-order linear partial differential equation, needs to be solved. The fact that the Laplace's equation is linear is particularly important, because a sum of any number of elementary solutions is also a solution of this equation. For example if each of n separate solutions Φ_1, Φ_2, ..., Φ_n solves Laplace's equation, then also the sum $w_1\Phi_1 + w_2\Phi_2 + ... + w_n\Phi_n$ represents a solution, where $w_1, w_2, ..., w_n$ represent an arbitrary set of real numbers.

2.3.1 Elementary Solutions

A solution composed of a surface distribution of elementary singularity solutions also satisfies Laplace's equation. In this way the problem reduces to finding only the strengths of each elementary solution on the body's surface. The problem therefore becomes a boundary-value problem where the boundary conditions are satisfied with proper elementary solution strengths. Since we are dealing with a simple steady potential flow, where no viscous and compressible effects need to be accounted, using this method is computationally much less demanding, compared

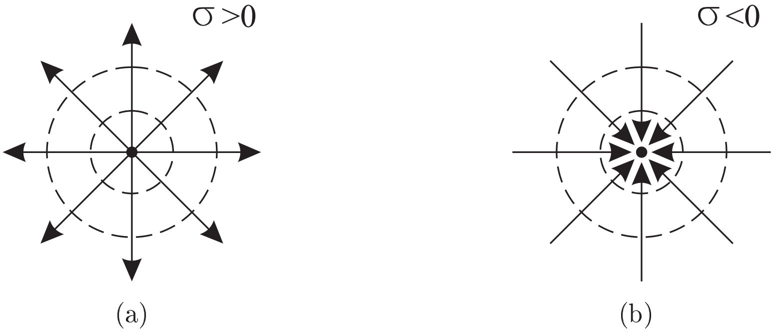

Figure 2.4: A two dimensional representation of (a) a source and (b) a sink elementary solution, denoted with streamlines (lines with arrows) and equipotential circles (dashed circles).

to methods that solve equations for the whole fluid domain $\mathcal{V}$, such as e.g. finite volume methods.

There exists a number of elementary solutions, that by definition produce irrotational and incompressible flow and at the same time limit to zero at an infinite distance from their origin (where the influence of the body's presence diminish to zero) and can be summed into a general solution. One of the examples is a *source/sink* flow where all the streamlines are straight lines emanating from/ sinking into a central point (Fig. (2.4)). The potential at an arbitrary point P in a three dimensional domain $\mathcal{V}$ at a distance r from the sink/source center location is then [22]

$$\Phi_S = -\frac{\sigma}{4\pi r}. \tag{2.24}$$

The velocity caused by this point source/sink can be obtained by using Eq. (2.10). The velocity has only the radial component that varies inversely with distance from the central point

$$\mathbf{V} = \frac{\sigma}{4\pi}\frac{\mathbf{r}}{|\mathbf{r}|^3}. \tag{2.25}$$

A positive σ represents a source, whereas a negative σ a sink. In case of a source elementary solution the flow is introduced from a point and in case of a sink the flow is diminishing into a point. This phenomenon violates the conservation of mass and the point must be, in case of e.g. surface integration, excluded from integration.

Another example of an elementary flow is a *doublet flow*. It is composed out of a source and a sink a distance g apart, as depicted in Fig. (2.5(a)). The velocity potential at a point P, a distance r from the source-sink pair, can be obtained as

$$\Phi(P) = -\frac{\sigma}{4\pi}\left(\frac{1}{|\mathbf{r}|} - \frac{1}{|\mathbf{r}-\mathbf{g}|}\right). \tag{2.26}$$

In a limit, when the distance g between the source and the sink goes to zero, while keeping a product $g\sigma$ finite and equal to μ, the potential goes to

$$\Phi(P) = \lim_{\substack{g\to 0\\ g\sigma\to\mu}} -\frac{\sigma}{4\pi}\left(\frac{|\mathbf{r}| - |\mathbf{r}-\mathbf{g}|}{|\mathbf{r}||\mathbf{r}-\mathbf{g}|}\right). \tag{2.27}$$

The numerator of Eq. (2.27) $|\mathbf{r}| - |\mathbf{r}-\mathbf{g}|$ goes in the limit to $g\cos\theta$ and denominator $|\mathbf{r}||\mathbf{r}-\mathbf{g}|$ to r^2. If the doublet points in direction normal to the surface (in direction of $\mathbf{n}$), the potential can be written as

$$\Phi = -\frac{\mu\mathbf{n}\cdot\mathbf{r}}{4\pi r^3}. \tag{2.28}$$

As in the case of a source or a sink, the doublet flow can be interpreted as a flow being induced by a discrete doublet of a strength μ placed at an arbitrary point. Therefore, a doublet is a singularity that induces about itself the double-lobed circular flow pattern shown in Fig. (2.5(b)). The potential can be further rewritten to take a form of a normal derivative of a source potential as

$$\Phi_D = \frac{\mu}{4\pi}\mathbf{n}\cdot\nabla\left(\frac{1}{r}\right). \tag{2.29}$$

The third elementary flow example is a *vortex flow*, with all the streamlines as a concentric circles about an infinite line, as sketched in Fig. (2.6(a)). The velocity along any given circular streamline is constant but varies inversely with a distance from the vortex line and can be expressed in cylindrical coordinates as [22]

$$\mathbf{V} = \left(0, -\frac{\Gamma}{2\pi r}, 0\right), \tag{2.30}$$

where Γ represents the circulation of observed vortex line aligned with the z axis.

The last example of an elementary solution, to be presented in the present work, is a *uniform flow* (Fig. (2.6(b))), e.g. a uniform flow with velocity V_∞ oriented in the positive x direction

$$\Phi_U = V_\infty x \tag{2.31}$$

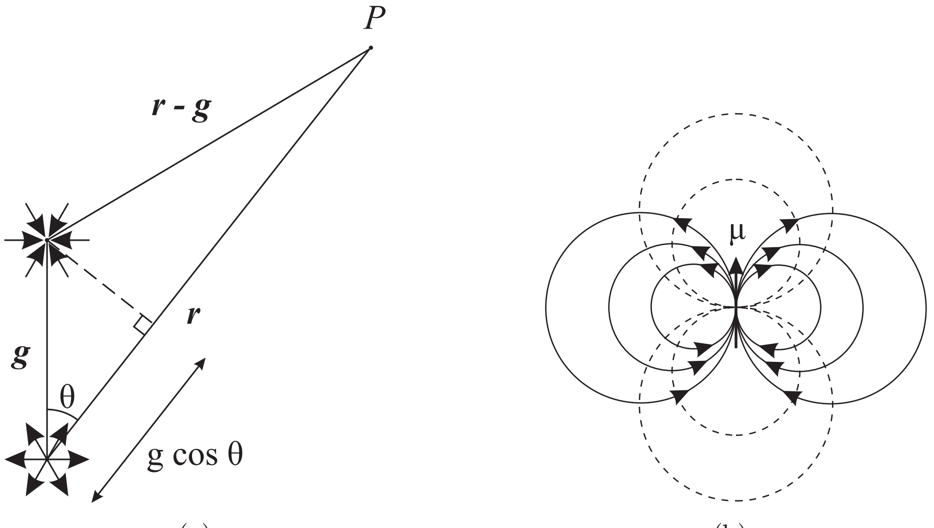

(a) (b)

Figure 2.5: (a) A doublet elementary solution is composed out of a sink and a source a distance g apart. (b) Streamlines (circles with arrows) and equipotential circles (dashed circles) around a doublet of strength μ in a two dimensional representation.

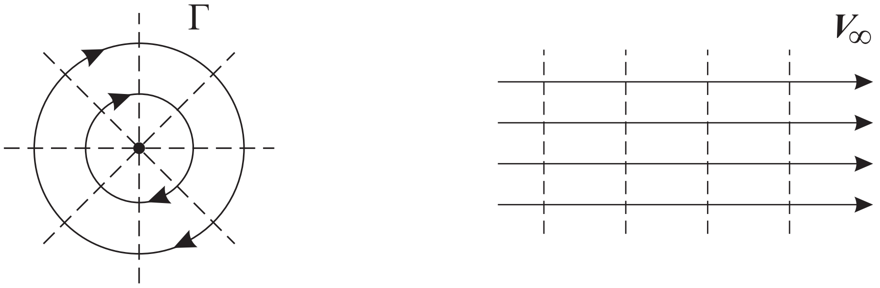

(a) (b)

Figure 2.6: (a) A cross section of a flow about a vortex of strength Γ laying perpendicular to the plane of the paper and (b) a uniform flow in direction of a freestream, denoted with streamlines (curves with arrows) and equipotential lines (dashed lines).

A simple combination of elementary flows can already produce some basic potential flows [22], e.g. a flow over a Rankine oval (uniform flow and a source-sink pair), nonlifting (two dimensional doublet flow) or lifting (two dimensional doublet and vortex flow) flow over a circular cylinder, etc.

2.3.2 Two Dimensional Elementary Solution Distributions

In this subsection some two dimensional cases of elementary solutions distributed along a single axis will be examined and their solution sought. At the end a suitable distribution of singularities will be chosen in order to describe the flow past an arbitrary body.

If a two dimensional source distribution $\sigma(x)$ along the x axis is examined (Fig. (2.7(a))), the velocity in y direction at an arbitrary point, as a sum of the influence of all discrete elementary sources laying in points x_0 (two dimensional form of Eq. (2.25)), has a form of

$$V_y(x,y) = \frac{1}{2\pi}\int_{x_1}^{x_2} \sigma(x)\frac{y}{(x-x_0)^2+y^2}dx. \tag{2.32}$$

In a limit, where y goes to zero, the integral goes to zero at all values of x except at $x = x_0$, therefore only points $\sigma(x_0)$ contribute to the integral. That is why $\sigma(x)$ can be moved out of the integral in Eq. (2.32) and replaced by $\sigma(x_0)$. The integration limits can now be pulled to infinity in both directions and the result doesn't change. The y component of velocity, when y is limiting towards zero from the positive or the negative direction, can be therefore written as

$$V_y(x,0\pm) = \lim_{y\to 0\pm}\frac{\sigma(x)}{2\pi}\int_{-\infty}^{\infty}\frac{y}{(x-x_0)^2+y^2}dx. \tag{2.33}$$

The result is after integration simply [22]

$$V_y(x,0\pm) = \frac{\partial\Phi}{\partial y}(x,0\pm) = \pm\frac{\sigma(x)}{2}. \tag{2.34}$$

For an arbitrary surface source distribution, the result can be rewritten as a difference between normal derivatives of external and internal potential

$$\sigma = \frac{\partial\Phi}{\partial n} - \frac{\partial\Phi_i}{\partial n}, \tag{2.35}$$

where subscript i indicates the limit to surface from under the surface and no subscript the limit to surface from above the surface.

A two dimensional doublet distribution along the x coordinate pointing in y direction (Fig. (2.7(b))) produces at an arbitrary point a velocity potential $\Phi(x,y)$ that can be expressed as a sum of the influence of all discrete elements laying in points x_0 (two dimensional form of Eq. (2.28)) as

$$\Phi(x,y) = -\frac{1}{2\pi}\int_{x_1}^{x_2} \mu(x)\frac{y}{(x-x_0)^2+y^2}dx. \tag{2.36}$$

This potential has a similar form as the y component of velocity resulting as a presence of a source distribution (Eq. (2.32)) and also has a similar solution. When approaching $y = 0$ from positive or negative direction, a jump in potential is created, that can be written as

$$\Phi(x, 0\pm) = \mp\frac{\mu(x)}{2}. \tag{2.37}$$

Strength of a doublet can be therefore expressed as a potential difference in points right under and above the surface as

$$\mu = \Phi_i - \Phi. \tag{2.38}$$

Velocity V_x can be further computed as

$$V_x(x, 0\pm) = \frac{\partial\Phi}{\partial x}(x, 0\pm) = \mp\frac{1}{2}\frac{d\mu(x)}{dx}. \tag{2.39}$$

Since a normal derivative of potential is zero at the body's surface, a doublet distribution results only in tangential flow at the surface of the body.

A two dimensional vortex distribution $\gamma(x)$ can be treated in a similar manner (Fig. (2.7(c))). The component of velocity in x direction at an arbitrary point can be expressed as a sum of the influence of all discrete elements laying in points x_0 (Eq. (2.30)) as

$$V_x(x,y) = \frac{1}{2\pi}\int_{x_1}^{x_2} \gamma(x)\frac{y}{(x-x_0)^2+y^2}dx. \tag{2.40}$$

In a similar manner as at the last two examples, the tangential velocity component right above and right under the surface can be computed as

$$V_x(x, 0\pm) = \frac{\partial\Phi}{\partial x}(x, 0\pm) = \pm\frac{\gamma(x)}{2}. \tag{2.41}$$

For an arbitrary surface vortex distribution, the result can be rewritten as a difference between tangential derivatives of external and internal potential as

$$\gamma = \frac{\partial\Phi}{\partial x} - \frac{\partial\Phi_i}{\partial x}. \tag{2.42}$$

By comparing Eq. (2.39) and Eq. (2.41), it can be observed, that the doublet distribution can replace the vortex distribution such that

$$\gamma(x) = -\frac{d\mu(x)}{dx}. \tag{2.43}$$

A combination of body surface doublet distribution that induces only the tangential component of velocity right at the surface, source distribution that induces a normal velocity jump across the surface together with a freestream flow looks like a good combination to model a flow around an arbitrary body. For wake modeling only doublet distribution is suitable, because it correctly considers a potential jump when crossing the wake, which will be presented in the next subsection. Additional distribution of vortices is in both cases redundant since it is equivalent to doublet distribution.

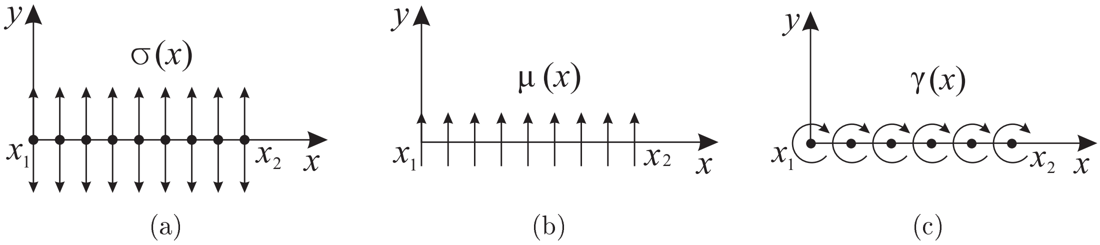

(a) (b) (c)

Figure 2.7: (a) Source, (b) doublet and (c) vortex distribution along x axis.

2.3.3 Kutta Condition

Let us now consider an arbitrary lifting body, e.g. a wing, and observe the irrotational flow passing the body on a cross-section plane parallel to the plane of symmetry and perpendicular to span direction at some chosen span location (Fig. (2.8)). If the velocity vector is integrated over a curve lying on observed plane starting from the point right under the wake going around the body and finishing at a point right above the wake, the bound circulation of the wing is calculated as

$$\Gamma = \int_a^b \mathbf{V} \cdot d\boldsymbol{s} = \int_a^b \nabla\Phi \cdot d\boldsymbol{s} = \int_a^b d\Phi = \Phi_b - \Phi_a. \tag{2.44}$$

Since the wake itself is composed of free vorticity that advects into the flow as a surface emanating from the trailing edge of the wing, it must be excluded from the integration, otherwise the Eq. (2.10) for the potential flow doesn't hold true. The bound circulation is therefore equal to a potential difference in points right above and right under the wake. In the case without a wake, the two potentials cancel each other, and circulation is zero. According to Kutta-Joukowski theorem

$$L = \rho_\infty V_\infty \Gamma \tag{2.45}$$

there clearly needs to be a wake present in order to model a lifting surface.

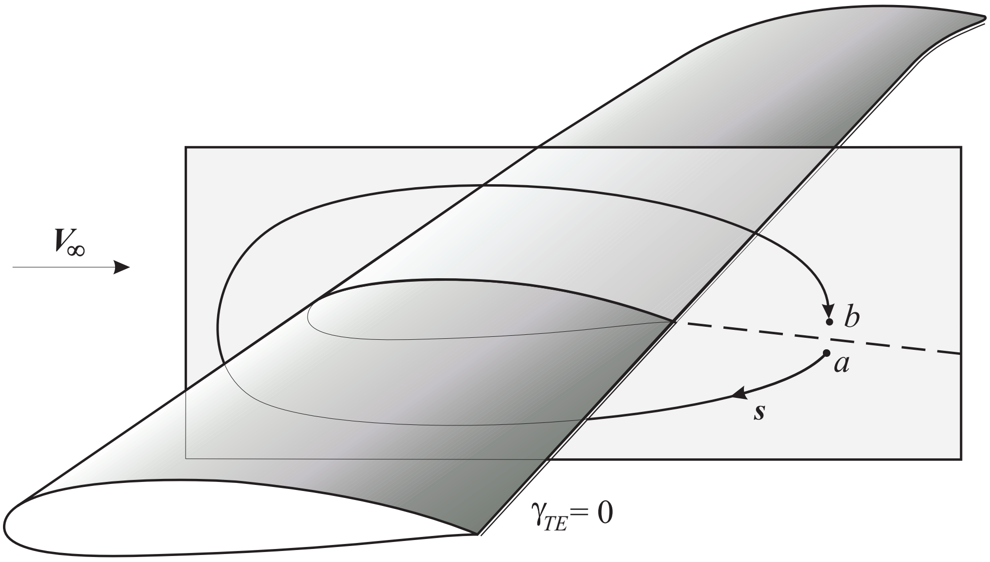

Figure 2.8: A path of integration, in order to calculate the bound circulation, around an arbitrary wing from point a to point b coinciding with a cross-section plane perpendicular to span direction at some chosen span location. The Kutta condition is denoted at the trailing edge of the wing.

By comparing Eq. (2.38) and Eq. (2.44), a linear dependence between the strength of a doublet that models the wake and the bound circulation at an arbitrary span position can be observed

$$\Gamma = -\mu. \tag{2.46}$$

Since the potential flow is defined up to a constant (Eq. (2.10)), there is an infinite number of possible theoretical potential flow solutions corresponding to the infinite choices for values of Γ. In real life a wing at each angle of attack produces a single value of lift. That is why a condition is needed that will give the correct circulation around a particular lifting body at fixed circumstances and in this way one particular solution out of all possible.

This condition comes from the fact that a steady flow is smoothly leaving the upper and the bottom surfaces at the trailing edge (TE) of the lifting body. In a case of a finite angle trailing edge a stagnation line is induced along the trailing edge, whereas in the case of a cusped trailing edge an equal velocity vector (in direction and magnitude) for both flows, coming from the upper and bottom surface, can be observed. For both types of the trailing edge the vorticity along the edge is according to Eq. (2.7) zero and the Kutta condition can be summarized with a single expression (Fig. (2.8)) as

$$\gamma_{TE} = 0. \tag{2.47}$$

By applying just stated Kutta condition in doublet and vorticity distribution relation (Eq. (2.43)), where x direction goes along the wake, it can be seen that the doublet strength must be constant along the wake in the streamwise direction or $\mu_W = \text{const.}$ at an arbitrary span location.

The same result can be demonstrated by looking at the problem from another perspective. It doesn't matter at which point along the wake at a chosen spanwise position the integration of velocity around the body is started (Eq. (2.44)). As long as the starting vortex is excluded from integration, the same amount of circulation will always be embraced, which denotes the same potential difference in points right above and under the wake. The wake isn't a solid surface, that is why it can't produce lift and therefore according to Kutta-Joukowski there are no bound vortices in the wake. The wake is composed only from free vortices whose strength is preserved along the wake in the streamwise direction. The amount of circulation that is released into the wake at some point along the body's span, comes from the upper and the lower surface right at the trailing edge

$$\Gamma_W = \Gamma_{up} - \Gamma_{low} \tag{2.48}$$

or after Eq. (2.46)

$$\mu_W = \mu_{up} - \mu_{low}. \tag{2.49}$$

If Kutta-Joukowski condition is now written for the free vortex distribution γ_W in the wake as

$$\rho \mathbf{V} \times \gamma_W = 0, \tag{2.50}$$

a condition for the wake shape can be derived as

$$\gamma_W \parallel \mathbf{V}. \tag{2.51}$$

Free vortices are therefore according to this linear theory parallel to the flow streamlines and continue to infinity. In real life though, the vortices influence on each other and together with the external flow influence introduce additional nonlinear effects, such as wake roll-up [22] and vortex breakup [48].

Chapter 3

Method

In this chapter, a surface optimization method applied in all test cases (Chapter 4) is presented. First, a classic first-order panel method is summarized after J. Katz and A. Plotkin [22]. Next, an electrostatic analogy of a surface integral over a panel doublet distribution is introduced. This analogy is then used in order to write a novel form of a panel method, a tool for surface potential distribution calculation. A model of a wake and a method for a velocity, pressure and pressure gradient distribution calculation is presented at the end of the first section.

In the second section, a complete procedure of surface optimization is presented, how the transformation of an initial surface is described and implemented, what are the cost functions being minimized in order to obtain optimal results and finally, which constraints are being used at different test cases.

3.1 Panel Method

3.1.1 The Problem

The present work deals with a steady incompressible potential flow in a volume $\mathcal{V}$ with an outer boundary S_∞ enclosing an arbitrary body with surface S_B and possibly also a wake surface S_W behind the body. The problem is treated in a body fixed coordinate system. The velocity and pressure distributions are obtained by the Laplace's equation (Eq. (2.12)) and Bernoulli's equation (Eq. (2.17)), respectively. The problem is a boundary-value problem, where boundary conditions need to be defined.

Because of the inviscid property of the fluid in the potential flow, the no-slip condition on the solid surface isn't satisfied. Furthermore, since the flow can't physically penetrate into the body, the velocity vector must be tangent to the surface and consequently only the normal component of velocity equals zero at the solid surface boundary

$$\mathbf{V} \cdot \mathbf{n} = \nabla \Phi \cdot \mathbf{n} = \frac{\partial \Phi}{\partial n} = 0, \tag{3.1}$$

where **n** is a vector normal to the body's surface. On the other hand, the disturbance in the flow created by the presence of the body should decay with distance **r** from the body. At domain's outer region ($\mathbf{r} \to \infty$) the following limit must hold true

$$\lim_{\mathbf{r} \to \infty} (\nabla \Phi - V_\infty) = 0. \tag{3.2}$$

Far away from the body, toward infinity, the flow therefore approaches the uniform freestream condition. But since an inviscid potential flow is being dealt with, the wake doesn't vanish far from the body. Because of this, the limit Eq. (3.2) doesn't hold true in the immediate vicinity of the wake on domain's outer region.

3.1.2 Classic First-Order Panel Method

Total potential at an arbitrary point P in the observed domain $\mathcal{V}$ as a consequence of a source and a doublet distribution on the surface of the body and the wake can be constructed after J. Katz and A. Plotkin [22] as a sum of a perturbation potential Φ^* and a freestream potential Φ_∞ as

$$\Phi(P) = \Phi^*(P) + \Phi_\infty(P), \tag{3.3}$$

or

$$\Phi(P) = \int_{S_B} (\Phi_D(P) + \Phi_S(P))\, dS + \int_{S_W} \Phi_D(P) dS + \Phi_\infty(P). \tag{3.4}$$

The wake is modeled by a thin doublet sheet and the body by a doublet and a source surface distribution. Physical surface normals **n** always point out of the observed volume, therefore out of the volume $\mathcal{V}$ on boundary S_∞ and into the body on surface S_B. The freestream potential has a form of

$$\Phi_\infty = V_{\infty,x} x + V_{\infty,y} y + V_{\infty,z} z. \tag{3.5}$$

Introducing Eqs. (2.24) and (2.29) for Φ_S and Φ_D into Eq. (3.4) results in

$$\Phi(P) = \frac{1}{4\pi} \int_{S_B + S_W} \mu \, \mathbf{n} \cdot \nabla \left(\frac{1}{r} \right) dS - \frac{1}{4\pi} \int_{S_B} \sigma \left(\frac{1}{r} \right) dS + \Phi_\infty. \tag{3.6}$$

In order to solve this main potential equation the boundary conditions need to be satisfied. The outer boundary condition at surface S_∞ (Eq. (3.2)) requires the derivative of perturbation potential to go to zero due to a small reach of body's influence on the freestream and large distance from the body.

$$\nabla \Phi^*|_{S_\infty} = 0. \tag{3.7}$$

In other words, velocity should be equal to freestream velocity far from the body. Again, this holds true at the whole outer region S_∞ except in the immediate vicinity of the wake. According to Eqs. (2.24) and (2.29), both elementary solutions already satisfy this boundary condition.

On the other hand, the Neumann boundary condition on the observed body's surface S_B (Eq. (3.1)) states that the flow can not go into the solid body and, as a consequence, the normal component of velocity is zero

$$\nabla \left(\Phi^* + \Phi_\infty\right) \cdot \mathbf{n} = 0. \tag{3.8}$$

Now that boundary conditions to the problem are specified, a unique solution still can't be obtained. There is an infinite number of different source and doublet distribution combinations that satisfy these boundary conditions (Eqs. (3.7) and (3.8)). An arbitrary choice therefore has to be made in order to define a desirable combination of elementary solutions and solve the Eq. (3.6). There are also some physical considerations that need to be dealt with in the problem. For example the right amount of circulation around the body needs to be assured in order to model a lifting body. This is achieved by properly modeling the wake and incorporating the Kutta condition (Eq. (2.49)) at the trailing edge.

If the boundary S_B is enclosed, then as a consequence of Neumann boundary condition (Eq. 3.8), the potential inside the body without internal singularities can be a constant

$$\Phi_i = \text{const.} \tag{3.9}$$

An equivalent statement says that velocity inside the body equals zero $\nabla \Phi_i = V_i = 0$. With the help of this observation a Dirichlet boundary condition can be set in terms of the potential inside the body. The inner potential can be then expressed as

$$\Phi_i(x, y, z) = \frac{1}{4\pi} \int_{S_B + S_W} \mu \, \mathbf{n} \cdot \nabla \left(\frac{1}{r}\right) dS - \frac{1}{4\pi} \int_{S_B} \sigma \left(\frac{1}{r}\right) dS + \Phi_\infty = \text{const.} \tag{3.10}$$

Both, the Neumann and Dirichlet boundary conditions equivalently state that normal component of velocity on body's surface must be zero.

Besides choosing different source/doublet combinations in order to satisfy boundary conditions, one must also choose an appropriate constant for inner potential in order to find a solution of Eq. (3.10). As it will be shown next, an inner potential that is not a constant can also be chosen. Following J. Katz and A. Plotkin [22], the inner potential can be set to freestream potential $\Phi_i = \Phi_i^* + \Phi_\infty = \Phi_\infty$, which reduces Eq. (3.10) to the simpler form

$$\frac{1}{4\pi}\int_{S_B+S_W} \mu \mathbf{n} \cdot \nabla \left(\frac{1}{r}\right) dS - \frac{1}{4\pi}\int_{S_B} \sigma \left(\frac{1}{r}\right) dS = 0. \tag{3.11}$$

A difference between normal derivatives of a total potential outside and inside the body is defined according to Eq. (2.35) as a source strength. Considering that the freestream potential is a constant and that a positive normal vector points into the body, the expression for the source can be simplified as

$$-\sigma = \frac{\partial \Phi}{\partial n} - \frac{\partial \Phi_i}{\partial n} = \frac{\partial \Phi^*}{\partial n} - \frac{\partial \Phi_i^*}{\partial n}. \tag{3.12}$$

Since $\Phi_i^* = 0$ everywhere inside the body also $\partial \Phi_i^*/\partial n = 0$ on S_B holds true. If the Neumann boundary condition (Eq. (3.8)) is rewritten as $\partial \Phi^*/\partial n = -\mathbf{n} \cdot \mathbf{V}_\infty$, the source strength can be written as

$$\sigma = \mathbf{n} \cdot \mathbf{V}_\infty. \tag{3.13}$$

Even though a freestream potential that is not a constant is chosen as an inner potential, the Neumann boundary condition (Eq. (3.8)) is still satisfied if the source distribution is defined according to Eq. (3.13).

The source distribution is now chosen and since the freestream distribution for a particular problem is usually known, the doublet distribution is left to be defined. After calculating the body surface doublet distribution that satisfies the boundary condition, the solution is still unique only for a nonlifting body. For a lifting surface the wake doublet distribution needs to be defined as well. As was shown in the previous chapter, the wake doublets can be expressed with body doublets through a Kutta condition (Eq. (2.49)), which assures the correct amount of lift force the flow induces on the body.

The surface of the body and the wake should now be discretized into N_B body surface panels and N_W wake surface panels, respectively (Fig. (3.1)). The

Dirichlet boundary condition (Eq. (3.11)) must be specified for a collocation point, which lies right under the centroid of each body panel. Therefore, for each one of N_B collocation points, the following statement holds true

$$\begin{aligned}\sum_{k=1}^{N_B} \frac{1}{4\pi} \int_{S_{B,k}} \mu \ \mathbf{n} \cdot \nabla \left(\frac{1}{r}\right) dS + \sum_{i=1}^{N_W} \frac{1}{4\pi} \int_{S_{W,i}} \mu \ \mathbf{n} \cdot \nabla \left(\frac{1}{r}\right) dS \\ - \sum_{k=1}^{N_B} \frac{1}{4\pi} \int_{S_{B,k}} \sigma \left(\frac{1}{r}\right) dS = 0.\end{aligned} \tag{3.14}$$

An integral over each individual panel is computed first, where μ, σ and $\mathbf{n}$ are doublet strength, source strength and surface normal of each infinitesimally small surface dS, respectively. Each panel's centroid is a distance r away from the corresponding collocation point. The next step is a summation of contributions of all the panels in order to take into account the influence of the whole doublet and source surface distribution in one collocation point. An assumption can be now made, that each panel has a constant doublet and/or source distribution over its surface. Eq. (3.14) can be rewritten as

$$\sum_{k=1}^{N_B} C_{jk}\mu_k + \sum_{i=1}^{N_W} C_{ji}\mu_i - \sum_{k=1}^{N_B} B_{jk}\sigma_k = 0, \tag{3.15}$$

for each collocation point j. All panel integrals are replaced by coefficients C_{jk}, C_{ji} and B_{jk}, where indices k and i run over all the body and wake panels, respectively.

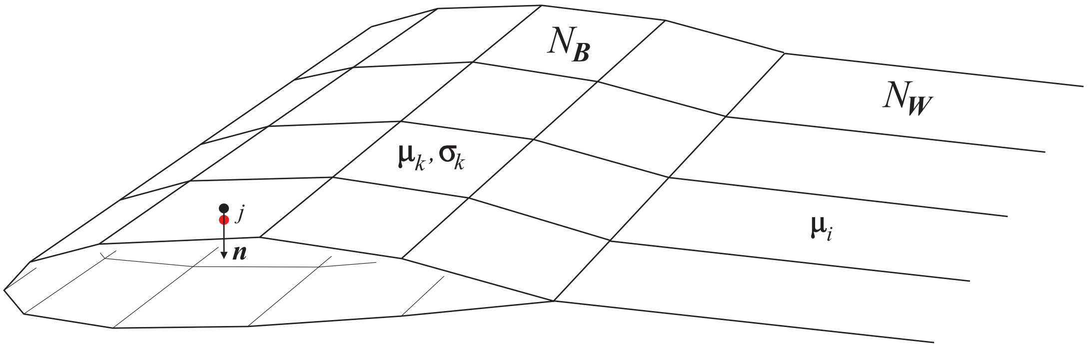

Figure 3.1: Discretization of the body and the wake surface into N_B body panels and N_W wake panels, respectively. All body and wake panels have constant doublet and/or source distribution over their surfaces. The collocation point (red dot) lies right under the centroid (black dot) of each body panel.

If the source strengths are selected according to Eq. (3.13), then coefficients

B_{jk} are known and can be moved to the right hand side (RHS) of the equation. Since there is N_B body doublet strengths and N_W wake doublet strengths, together $N_B + N_W$ unknowns, and only N_B equations, one for each collocation point, the Kutta condition (Eq. (2.49)) needs to be applied in order to connect the body and wake doublets. According to Kutta condition, each wake doublet can be expressed in terms of the body trailing edge doublets as

$$\mu_i = \mu_{i,up} - \mu_{i,low}, \tag{3.16}$$

where $\mu_{i,up}$ is a doublet on the upper and $\mu_{i,low}$ on the lower side of the body surface at the trailing edge, both neighbours of the corresponding wake doublet. The influence of each wake panel can therefore be written as

$$C_{ji}\mu_i = C_{ji}(\mu_{i,up} - \mu_{i,low}). \tag{3.17}$$

If Eqs. (3.17) are inserted into Eq. (3.15), then a new set of coefficients can be introduced as $A_{jk} = C_{jk}$, if body panel is not at the trailing edge and as $A_{jk} = C_{jk} \pm C_{ji}$, if body panel is at the trailing edge.

In this way, the number of unknowns becomes equal to the number of equations. System of equations can now be written as

$$\sum_{k=1}^{N_B} A_{jk}\mu_k = \sum_{k=1}^{N_B} B_{jk}\sigma_k. \tag{3.18}$$

In short, each panel has a constant doublet and/or source distribution which causes a change of potential in an arbitrary point P in the observed volume. If a potential at the point P, as an influence of the whole body and wake, is sought, each panel's distribution needs to be integrated first and the influence of all the panels summed afterwards.

3.1.3 Electrostatic Analogy

A simpler method that can be used in order to compute a potential at an arbitrary point P as a consequence of a presence of a body leans on an analogy to electrostatics. According to the analogy, the electrostatic potential at a point P is, as a consequence of a panel with a constantly distributed electric dipole over its surface, proportional to the solid angle of observed panel looking from the point P [49].

If a doublet distribution replaces the electric dipole distribution, a velocity potential instead of an electrostatic potential can be computed. A potential in j-th collocation point as a consequence of i-th panel is therefore proportional to the doublet strength μ_i of the panel multiplied by the solid angle Ω_{ji} (Fig. (3.2)) at which the point sees this panel

$$\Phi_j^* = -\frac{\mu_i}{4\pi}\Omega_{ji}. \tag{3.19}$$

Since panels with a constant doublet distribution are considered in present work, the electrostatic analogy represents a major simplification to the problem. Moreover, it can be applied to panels of an arbitrary shape.

A Dirichlet boundary condition in a form of a constant inner potential (Eq. (3.9)) is used, where a value of zero is chosen as the constant

$$\Phi_j = \Phi_j^* + \Phi_{\infty,j} = 0. \tag{3.20}$$

In this way, a body source distribution is redundant, which additionally simplifies the method. Of course, any other constant different from zero, could also be used. This would only shift the doublet distribution by a constant, but the results for the external potential would remain the same.

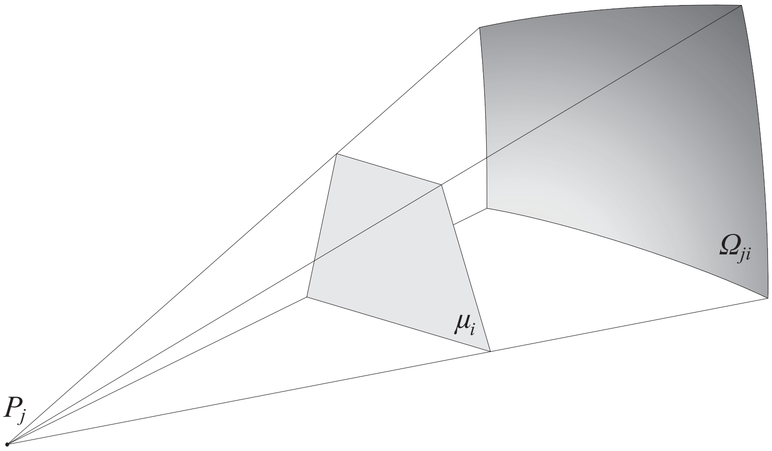

Figure 3.2: Solid angle Ω_{ji} of a panel with a constant doublet surface distribution μ_i, looking from the collocation point P_j.

If the freestream potential is written as an integral of a freestream velocity

$$\Phi_{\infty,j} = V_{\infty,x}x_j + V_{\infty,y}y_j + V_{\infty,z}z_j = RHS_j, \tag{3.21}$$

the base system of equations of the problem can be expressed by combining Eqs.

(3.19) - (3.21) as

$$\frac{1}{4\pi}\Omega_{ji}\mu_i = RHS_j. \tag{3.22}$$

After computing the doublet distribution as a solution of the system of equations (Eq. (3.22)), where additionally the Kutta condition needs to be considered based on the procedure described with Eqs. (3.16) and (3.17), all distributions are known, all boundary conditions are satisfied and the potential Φ at any point in the observed volume $\mathcal{V}$ can be defined. Since a body surface velocity, pressure, and gradient of a pressure distributions are in pursuit, a special interest lies in the value of the potential in each panel centroid.

3.1.4 Wake

An inviscid outer flow is considered as a valid approximation for computing a surface pressure distribution of an attached flow passing a body, but in order to define the potential distribution around the lifting body, the viscosity at its trailing edge can't be neglected. A finite viscosity is incorporated in the problem through Kutta condition (Subsection 2.3.3) and consequently through an nonphysical surface behind the body called a wake.

In the case where a part of the body has no clear trailing edge, e.g. a wing-fuselage configuration, two different wake sections should be used [50]. Behind the wing, a wake denoted as *wake A* is used. Its doublet strength distribution is defined through the Kutta condition. For the fuselage, on the other hand, an assumption can be made that it doesn't shed vorticity into the wake. The doublet distribution of the wake behind the fuselage, *wake B*, must be therefore, according to Eq. (2.43), constant in the spanwise direction. These wake B doublets must also have the strength equal to their first neighbour in the wake A, otherwise there would be a finite vortex in the region of the fuselage-wing junction. Wake A therefore has doublets that are variable in the spanwise direction and constant in the streamwise direction (Subsections 2.3.2 and 2.3.3), whereas wake B has a constant distribution of doublets.

A decision has been made to always use the shape of the wake as a flat plane, therefore neglecting wake roll-up, leaving the trailing edge of the lifting body at an angle cutting the trailing edge angle in half - along bisecting plane. In this way, the same shape of the wake can be used for all angles of attack. Since the surface pressures are insensitive to the angle of inclination of the wake [51], this approximation gives solutions that are essentially as accurate as can be expected from the potential flow assumption. In true nature, the wake is far from the body eventually dissipated by viscous and turbulent effects (vortex breakup). That is why, a reasonable length of the wake should sufficiently describe the real case. In all test cases in present work, the wake therefore extends approximately thirty lifting-body chord lengths behind the body.

3.1.5 Velocity, Pressure, and Gradient of a Pressure Distributions

Since we are dealing with a potential flow, the velocity at the body surface is not equal to zero and is tangent to the surface. Velocity vector of i-th body panel in its centroid point can be computed from its own potential and the potential of its neighbours. An arbitrary panel is a neighbour of the panel i if they share an edge and if an angle between their normals is less that 60°, as it was chosen. Since quadrilateral panels are chosen for this work, the maximal number of neighbours each panel has is four. At sharper edges, e.g. at a wing trailing edge, there are only three neighbours, and at some corners even just two neighbours.

If centroids of all the neighbours, where the potentials are calculated, are projected on i-th panel's local coordinate system (Fig. (3.3)), then i-th panel's potential Φ_i together with its neighbours' potentials can be used to construct a linear approximation. The potential at an arbitrary point in the vicinity of the centroid i can be expressed as

$$\Phi = \Phi_i + \left(\frac{\partial \Phi}{\partial x}\right) x_i + \left(\frac{\partial \Phi}{\partial y}\right) y_i, \tag{3.23}$$

where x_i and y_i represent the local coordinates and expressions $(\partial\Phi/\partial x)$ and $(\partial\Phi/\partial y)$ the velocity components in this coordinate system. If expression Eq. (3.23) is evaluated at projected centroid of each neighbour, the unknown gradients can be computed with a weighted least square method, where the minimum

$$\min \left[\sum_j w_j \left(\Phi_i + \left(\frac{\partial \Phi}{\partial x}\right)_i x_j + \left(\frac{\partial \Phi}{\partial y}\right)_i y_j - \Phi_j \right)^2 \right] \tag{3.24}$$

is sought. The system of equations that needs to be solved in order to compute velocity components in local coordinate system for i-th panel is then

$$\begin{pmatrix} \sum_j w_j x_j^2 & \sum_j w_j y_j x_j \\ \\ \sum_j w_j y_j x_j & \sum_j w_j y_j^2 \end{pmatrix} \begin{pmatrix} (\partial\Phi/\partial x)_i \\ \\ (\partial\Phi/\partial y)_i \end{pmatrix} = \begin{pmatrix} \sum_j w_j \left(\Phi_j - \Phi_i\right) x_j \\ \\ \sum_j w_j \left(\Phi_j - \Phi_i\right) y_j \end{pmatrix}. \tag{3.25}$$

The weight w_j is chosen to be reciprocal square distance between j-th and i-th centroid point in global coordinate system (Fig. (3.3)). Neighbours that are closer to i-th centroid have a greater influence on the result and vice versa. The solution of Eq. (3.25) represents, after a transformation to a global coordinate system, a velocity surface distribution $\mathbf{V}$.

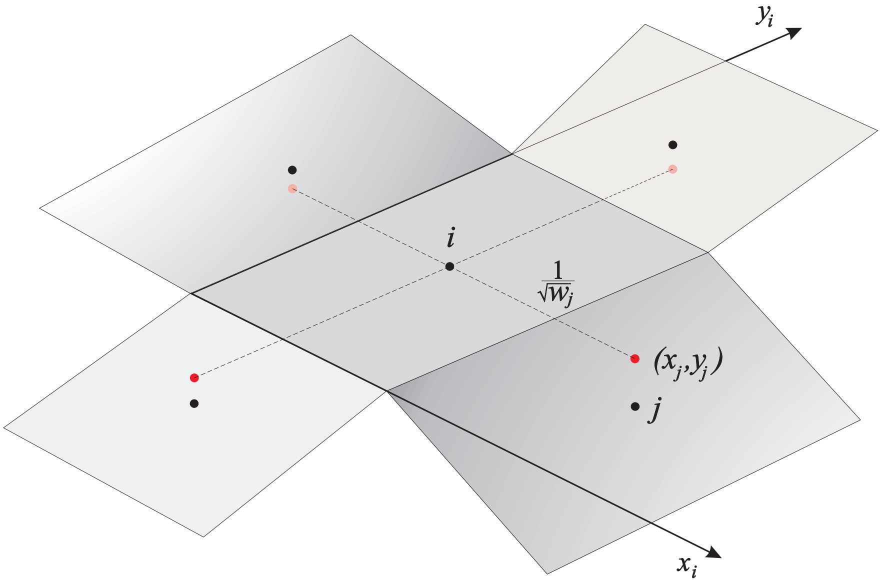

Figure 3.3: i-th panel with its four neighbours. Black dots denote centroids, whereas red dots denote their projection on i-th local coordinate system.

The surface pressure distribution, or more precisely the dimensionless pressure coefficient distribution, can be computed in the next step from the velocity surface distribution using Bernoulli's equation (Eq. (2.17)). Information about the gradient of a pressure distribution over the body surface is also needed, since it is used for the calculation of a cost function that is being minimized during surface optimization. The gradient of a pressure is computed from the pressure distribution in a similar manner to the computation of the velocity from the potential.

3.2 Surface Optimization

In this section, a procedure of surface shape transformation is described that takes place during surface optimization. Next, the cost functions are presented that are used in present work in order to obtain a favourable pressure distribution. Optimization constraints that enable increased control of surface transformation are introduced at the end of this section.

A mathematical expression that describes the optimization problem can be written as

$$\min_{k} F(k) \quad \text{such that} \begin{cases} nec(k) \leq 0 \\ ec(k) = 0 \\ lb \leq k \leq ub. \end{cases} \tag{3.26}$$

Here, the optimization variables k, that minimize the cost function $F(k)$ under different constraints are in pursuit. $nec(k)$ and $ec(k)$ are nonequality and equality constraints, while lb and ub represent the lower and the upper optimization variable boundaries, respectively.

Surface optimization can be done for the whole body, or just for a part of its surface, called a *patch*. During the whole body optimization the complete body surface is free to change, whereas during the optimization of a selected surface patch, only the patch can take a new shape and the rest of the body has a fixed surface.

3.2.1 Bézier Surface and Deformation Vector Field

As it was already stated, the surface of the observed body is meshed with quadrilateral panels. A point common to all neighbouring panels lying around it is called a *node*. This meshed original surface represents an initial condition for the surface optimization. The shape of the patch is changed by moving its node points according to the deformation vector field and magnitude of change surface function. Deformation vector field sets the direction and additionally the fixed share of shift for each node. Magnitude of change surface function on the other hand sets the varying share of node shift and is defined by a *Bézier surface* [52].

Bézier surface is therefore used only to describe the magnitude of the translation of our patch and not to describe its surface directly. A Bézier surface multiplied by a deformation vector field $\mathbf{d}$ is added to the original patch and together they form a new shape, which is depicted in Fig. (3.4). For a position of an arbitrary node i the following equation then holds true

$$\mathbf{r}_{i,new} = \mathbf{r}_{i,old} + h(u_i, v_i)\mathbf{d}_i, \tag{3.27}$$

where $0 \leq u_i \leq 1$ and $0 \leq v_i \leq 1$ represent surface coordinates of i-th node on the patch and $h(u_i, v_i)$ a scalar value of a Bézier surface. $\mathbf{r}_i$ is a position of i-th node in global Cartesian coordinate system. The Bézier surface $h(u, v)$ that is used to translate all the nodes on the patch parametrized with surface coordinates (u, v) is defined as

$$h(u, v) = \sum_{i=1}^{n} \sum_{j=1}^{m} B_i^n(u) B_j^m(v) k_{i,j}, \tag{3.28}$$

where one of the Bernstein polynomials is

$$B_i^n(u) = \binom{n-1}{i-1} u^{i-1} (1-u)^{n-i} \tag{3.29}$$

with binomial coefficient as

$$\binom{n-1}{i-1} = \frac{(n-1)!}{(i-1)!(n-i)!}. \tag{3.30}$$

Indices i and j run through all the $n \times m$ scalar control points $k_{i,j}$, that represent the optimization variables. With a proper value of each control point a minimal cost function can be achieved and therefore an optimal patch shape designed. From the stated it can be seen, that only a small number of variables is needed to smoothly change the shape of the original surface, instead of a few hundreds or even thousands in order to shift each node separately.

If all control points are equal to zero, then also the values of Bézier surface in all the nodes are zero and the patch preserves its shape. The same result can be observed if the deformation vector is zero. Since a shift of each node is controlled in two ways, different shape features can be assured. With Bézier surface a smooth patch shape change is achieved, whereas with a proper choice of the deformation vector field e.g. a tangency to the fixed surface around the patch can be preserved. Since a deformation vector field, instead of a Bézier surface, is used in order to preserve the tangency, a smaller number of control points is needed and a patch is able to take a more dynamic shape close to its edge. A smaller number of control points consecutively means a computationally less demanding problem.

A direction of deformation $\mathbf{d}$ is defined for every node in advance and it doesn't

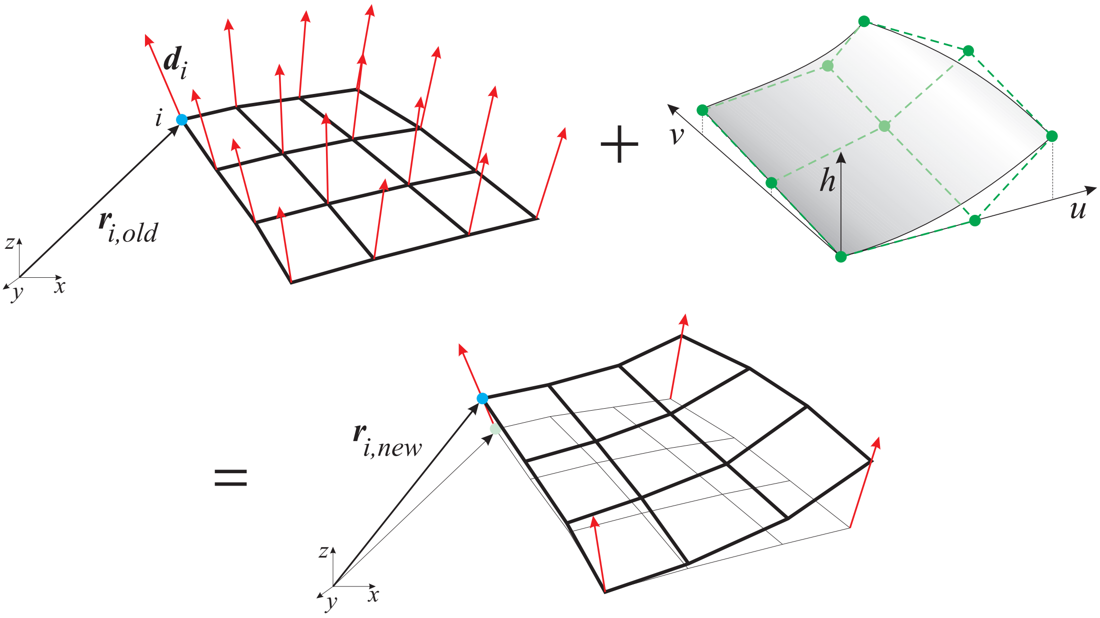

Figure 3.4: Each node on the surface (i-th node depicted in blue colour) is during optimization process transformed in space by adding to its position vector $\mathbf{r}_i$ a deformation vector $\mathbf{d}_i$ (red vector field) multiplied by a value of the Bézier surface $h(u, v)$ (its control points k are depicted in green colour) at that position.

change during the optimization. On the other hand, for the Bézier surface control points, since they are optimization variables, only the initial values are defined at the beginning of the optimization process.

In the present work, a case dependent deformation vector field is used, since a nature of each case is different. In general, a deformation vector field must give enough freedom for the patch to take an optimal shape, but it still needs to properly constrain and direct the translation of nodes in order to achieve physically reasonable results. In some cases a deformation in direction of a surface normal is a good choice, e.g. it enables a bluff body to expand and contract in all directions, but it usually needs to be constrained in order not to push the surfaces together. Although this reduces the influence of a body on the flow and consequently the drag, the zero-cross-section solution is physically not acceptable. On highly curved surfaces a deformation in normal direction can also result in an intersection of panels, which additionally leads to some numerical problems.

A tangency to the fixed surface around the patch can be preserved by multiplying a normalized deformation vector field by a function that tangentially descends to zero at the patch edge. Away from the edge, this function should have a value of one, so that the amount of deformation in this region is controlled mainly by the Bézier surface. A proper deformation vector field choice is, as was stated, of great importance in order to achieve optimal results without problems during optimization.

3.2.2 Cost Functions

According to the potential flow theory, the flow passing an arbitrary body doesn't produce drag (Section 2.2). Because of this reason, the proposed optimization theory can be used to minimize drag only in an indirect way, e.g. through a surface pressure distribution. A functional or a combination of functionals (*cost function*) should therefore be used, which will, when minimized, produce a favourable pressure distribution.

A minimization of a cost function in a form of an integration of a pressure gradient across the body's surface

$$F = \int \left| \nabla C_p \right| dS \tag{3.31}$$

smoothens the pressure distribution [9], which prevents unnecessary fluctuations of the flow velocity. In a discretized form the cost function can be written as

$$F = \sum_i \left| \nabla C_p \right|_i S_i, \tag{3.32}$$

where S_i is a surface area of i-th panel. As it will be shown in Chapter 4, a minimization of a cost function in a form of Eq. (3.32) results in a plateau-like pressure distribution in a streamwise direction across the body. At the leading edge of the body, the pressure quickly drops to the plateau pressure value and at the pressure recovery region it quickly increases back to the freestream pressure. In this way a minimal amount of acceleration and deceleration of the flow is achieved, which reduces instabilities in the boundary layer and can lead to a thinner boundary layer.

Why the minimization of Eq. (3.32) leads to a plateau-like pressure distribution can be best seen in a two dimensional case, where the integral of the pressure gradient can be written as

$$\int \left| \frac{\partial C_p}{\partial x} \right| dx = \sum_i \left| C_{p,i} - C_{p,i+1} \right|, \tag{3.33}$$

where $C_{p,i}$ represent pressure coefficient values in points with zero pressure gradient. Imagine now a pressure distribution around an airfoil, where only the upper side of the shape is being optimized with a fixed lift force constraint (Fig. (3.5(a))). It is clear that the sum in Eq. (3.33) reaches the minimal value when the maximal $C_{p,min}$ is obtained. Since the surface under the pressure distribution curve must remain constant because of the fixed lift force constraint, the optimal pressure distribution on the upper side of the airfoil must obtain a plateau-like shape with a plateau pressure value at maximal $C_{p,min}$ (Fig. (3.5(b))). Even though test cases in present work (Chapter 4) don't have fixed lift force constraint, the surface under the pressure distribution curve, because of the geometrical constraints and the nature of the deformation vector field, is still constrained and a finite maximal $C_{p,min}$ exists.

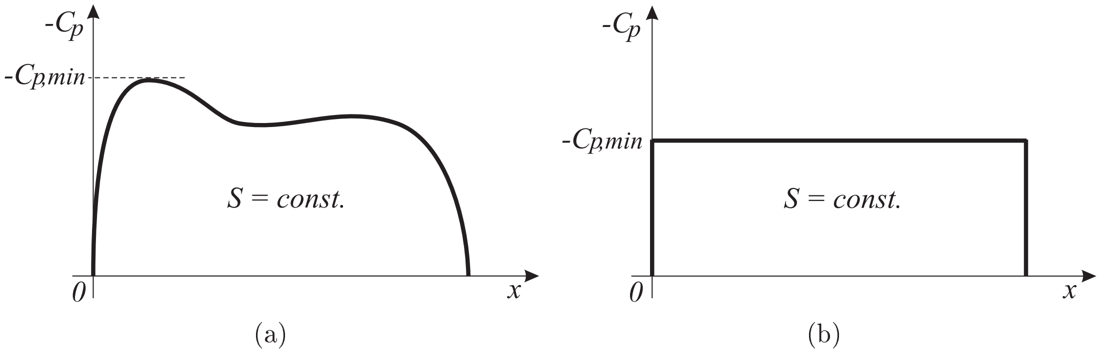

(a) (b)

Figure 3.5: Two dimensional pressure distribution over the upper side of (a) an airfoil and (b) its optimal distribution.

If a parameter b, called a *bias*, is added to the pressure gradient in the streamwise direction as

$$F = \sum_i \sqrt{\left(\nabla_{\parallel} C_p - b\right)_i^2 + \left(\nabla_{\perp} C_p\right)_i^2}\; S_i, \tag{3.34}$$

the minimization will try to achieve a streamwise pressure gradient value equal to b on as many panels as possible. An appropriate value of bias will change the plateau-like region of a pressure distribution to a ramp-like distribution, which will gradually accelerate the flow as far back to the end of the body as possible. A favourable pressure gradient therefore postpones the transition and may also prevent the flow separation.

As can be seen from Eq. (3.34), a gradient of a pressure surface distribution is composed out of a streamwise component and its transverse component. Since the latter is responsible for introducing a cross-flow instabilities into the boundary layer, the sum of both components should be minimized. The pressure distribution becomes therefore smoother in all directions. In all test cases of present work both components have been treated equally regarding the minimization of the cost function, as per Eq. (3.34).

Introduced cost functions should have after minimization a positive impact on the amount of instabilities in the boundary layer, but nevertheless, additional steps should be taken in order to properly design also the pressure recovery region. In next subsection a criterion will be introduced as a constraint, that considers especially this part of the surface.

3.2.3 Constraints

Stratford criterion. In some cases the pressure recovery region can be so severe that the flow detaches from the body surface and tremendously increases the drag. In order to prevent this from happening a *Stratford criterion* [53] is additionally incorporated as a constraint during optimization process.

The Stratford criterion is a rather simple method to estimate a point where the laminar or turbulent flow will detach from the body surface on the basis of the Reynolds number, the pressure distribution and the gradient of the pressure distribution. It is a conservative criterion that predicts the separation just a bit before the methods based on the full boundary layer equations [54]. Even though it is a simple and easy to implement method, it still enables one to compute a pressure distribution that is everywhere on the edge of the separation, which permits a maximum extent of laminar flow and a rapid pressure recovery region.

Since the laminar and the turbulent flows have different characteristics, the criterion forms for both flows also differ. In case of a flow transition right before the recovery region, the Stratford criterion for separation of a turbulent flow

$$G = Cp'\sqrt{x'\frac{dCp'}{dx}}\left(\frac{10^6}{Re_{x'}}\right)^{0.1} = \begin{cases} 0.35, & \frac{d^2p}{dx^2} < 0 \\ 0.39, & \frac{d^2p}{dx^2} > 0 \end{cases}, \tag{3.35}$$

but with a “history” of a laminar flow

$$x' = \int_0^{x_m} \left(\frac{V}{V_{max}}\right)^5 dx + (x - x_m), \tag{3.36}$$

should be used. x' in Eq. (3.36) represents an effective length of the boundary layer, where the integral takes into consideration what happened to the flow along the body's surface up to the beginning of the pressure recovery. C_p' is a canonical pressure coefficient

$$C'_p = 1 - \frac{V^2}{V_{max}^2} = \frac{C_p - C_{p,min}}{1 - C_{p,min}}, \tag{3.37}$$

whose derivative is

$$\frac{dC'_p}{dx} = -\frac{1}{V_{max}}\frac{dV}{dx} = \frac{1}{1 - C_{p,min}}\frac{dC_p}{dx}. \tag{3.38}$$

x' is an effective boundary length that goes along the body in a streamwise direction, x_m is a value of a streamwise coordinate indicating the beginning of the pressure recovery, and $C_{p,min}$ and V_{max} are the corresponding minimal pressure and maximal velocity magnitude, respectively. Reynolds number is constructed from the maximal velocity V_{max} and effective length x'.

The Stratford criterion (Eq. (3.35)) is valid only for canonical pressure coefficients $C'_p < 4/7$. For larger numbers it doesn't hold true, but it can still serve as a reference. The criterion was used at all recovery regions of the present work, even if there is an absence of a theoretical justification of its validity.

There are two different critical values of a Stratford number G, at which the flow suppose to separate, depending on the shape of the pressure recovery region (Eq. (3.35)). For a concave recovery 0.35 is used and for a convex 0.39.

The aim of this constraint is to keep the Stratford number of each panel under this critical value, but since the number of constraints should be as small as possible in order to shorten the computation time, each panel shouldn't be constrained separately.

Moreover, neither should a single panel with the maximal Stratford number be constrained. If only one panel with currently the largest number is constrained, only that panel will receive attention during an optimization step, in order to be put under constraint. But in the next step some other panel could have the largest number and that one will be in the spotlight. During the optimization process jumping from panel to panel can occur, which can bring some convergence problems. To avoid this problems, the best way is to constrain an average of a few panels with the largest Stratford numbers. The function that is therefore put under constraint is

$$G_M = \frac{\int_{S_B} G(\mathbf{r}) e^{a_0(G_{max} - G(\mathbf{r}))} d\mathbf{r}}{\int_{S_B} e^{a_0(G_{max} - G(\mathbf{r}))} d\mathbf{r}}. \tag{3.39}$$

G_{max} is the maximal Stratford number and the parameter a_0 defines how many panels with largest Stratford numbers are taken into consideration. The bigger the parameter $a_0 > 0$ the smaller number of panels will influence on the number

G_M. The number G_M is always smaller compared to the maximal panel Stratford number, except in a limit, when $a_0 \rightarrow \infty$, they are equal. In this way all the Stratford number peaks scattered through the patch will be smoothly and gradually put under constraint and fewer problems with convergence should occur.

The Stratford number patch distribution is in the first test case (Section 4.2) weighted also with a "soft" Heaviside function of pressure as

$$G_{i,new} = \frac{G_{i,old}}{1 + \exp\left(\frac{Cp_i - a_1}{a_2}\right)}, \tag{3.40}$$

so that the region with maximal pressure, such as at the trailing edge, isn't taken into consideration during the optimization. At the trailing edge region the flow leaves the body into the wake and can produce a short high pressure impulse. Since it is not possible to get rid of this anomaly, it is better to ignore it, otherwise the optimization can spend a lot of time optimizing that region and at the end diverge or produce unusable results. This procedure is, because of some convergence problems, omitted at the latter two test cases (Sections 4.3 and 4.4).

Another modification of the Stratford criterion is introduced into the method because of some convergence problems at the final stage of the optimization. The optimization is first run with parameters x_m, $C_{p,min}$ and V_{max} (Eqs. (3.36)-(3.38)) defined at each iteration successively. After a few iterations of optimization, when the method finds an approximate optimal shape and these parameters settle down, the optimization is deliberately stopped. Parameters x_m, $C_{p,min}$ and V_{max} defined at the last iteration and the integral in Eq. (3.36) calculated considering also these parameters are then used as constants at the complete optimization procedure. These parameters therefore don't vary from iteration to iteration any more, but remain fixed through the whole optimization. Without this simplification, the solution tends to diverge in some cases. For the sake of generality, the same simplification is used in all test cases. In cases without convergence problems the method is verified to produce identical solutions with or without this modification.

Geometrical constraints. One way of controlling the amount of modification of a patch is by bounding the size of control points of Bézier surface (Eq. (3.28)) that defines the change of the patch shape. Since there is a small number of control points, their size has an influence on a wider region of the patch. In some cases a very local control of shape modification is needed, usually because of some packaging problems, but also in other applications, e.g. to maintain the shape of a trailing or leading edge. These geometrical constraints are therefore useful at controlling the exact magnitude of translation at some chosen points and in this way preventing the surface to contract or indent at those points.

The Stratford criterion (Eq. (3.35)) and these geometrical constraints are introduced into optimization process as nonequality nonlinear constraints (Eq. (3.26)).

Chapter 4

Results

In this chapter, a convergence analysis of the panel method with an example of a sphere is made first. Next, the results of proposed surface optimization analysis on three conceptually different test cases are presented and evaluated with results obtained by CFD analysis. All three test cases originate from real world cases.

At all test cases, the body surface was first meshed using a program called *Salome*, which is an open-source software that provides a generic platform for pre- and post-processing for numerical simulation. This original mesh was then used as an initial condition for the surface optimization process, for which a program was written in *Matlab* environment. During this process a Matlab's function called *fmincon*, which uses a superlinear convergent sequential quadratic programming method (SQP) with an active-set method as a quadratic programming subproblem solver [34], has been used in order to find a minimum of a constrained nonlinear multivariable cost function. A solution of the subproblem is then used for a line search procedure [55] for a new major iteration. Function *fmincon* therefore requires predefined initial estimate and boundaries of all optimization variables, and pointers to the code of the cost function and all possible constraints that are used at each iteration of the optimization process.

CAD models were then constructed from the optimized surface meshes and together with the original surfaces put into the CFD analysis in order to evaluate the results. For CFD computations a finite volume program called *OpenFOAM* with its RANS solver for incompressible and viscous flows, *simpleFoam*, was used. The meshes for this purpose were constructed with the *snappyHexMesh* subroutine.

In the first test case, where a laminar-turbulent transition plays an important role, a $k-k_L-\omega$ *turbulence model* [56] was used in order to predict the location of transition. In the remaining two cases the simpler one equation *Spalart-Allmaras turbulence model* [57] was used, because it has already shown good performance in junction flows [58]. All the CFD computations were run to full convergence, which was determined by the flattening of all residuals (at values smaller than 10^{-5}) and forces.

4.1 Panel Method Verification

The proposed panel method is verified using an example of a potential flow passing a sphere. In order to reduce the computation time, the case is considered as a symmetrical problem, where only a half of a sphere surface is discretized into different number of quadrilateral panels N_B. The system of equations (Eq. (3.22)) is in this way halved, but the second half of the sphere with symmetrical doublet distribution is still taken into consideration. The inflow is parallel to the symmetry plane that cuts the sphere on two halves. The property of a symmetry plane is that none of the streamlines can cross it and that the streamline that starts on this plane at the inflow will stick to it all the way around the body and onwards.

At each number N_B a relative difference between panel method results and analytical solution for a potential

$$\Phi_{AN}(r,\theta) = V_\infty \cos\theta \left(r + \frac{R^3}{2r^2} \right) \tag{4.1}$$

and a velocity surface distribution

$$V_{\theta,AN}(r,\theta) = -V_\infty \sin\theta \left(1 + \frac{R^3}{2r^3} \right) \tag{4.2}$$

is computed as

$$\frac{\sum_i^{N_B} S_i \left| \Phi_i - (\Phi_{AN})_i \right|}{\sum_i^{N_B} S_i |(\Phi_{AN})_i|} \tag{4.3}$$

and

$$\frac{\sum_i^{N_B} S_i \left| V_i - (V_{\theta,AN})_i \right|}{\sum_i^{N_B} S_i (V_{\theta,AN})_i}. \tag{4.4}$$

Each summation runs over all the panels with surface areas S_i. Each analytical solution is, the same as panel method results, computed in centroid of corresponding panel. Sphere radius and inlet velocity are chosen as $R = 1$ and $\mathbf{V}_\infty = (1, 0, 0)$.

It can be seen from Fig. 4.1(a) that the relative difference between the computed and the analytical solution is inversely proportional to the number of panels N_B. With increasing number of panels, the panel method converges to the analytical solution. On the other hand the time of computation (c. time) increases faster than N_B^2 in this case. A decision has to be made as to what is a reasonable number of panels in order to acquire results with a satisfactory accuracy, but at the same time not to increase the computation time excessively.

An example of computed velocity surface distribution where a half of a sphere is discretized into $N_B = 578$ panels is presented in Fig. 4.1(b). The inflow travels from the left to the right side of the figure. Since a potential flow without viscosity effects is applied, the velocity surface distribution at the impact side equals the one at the recovery region. The force acting on the sphere is therefore equal to zero (d'Alembert paradox).

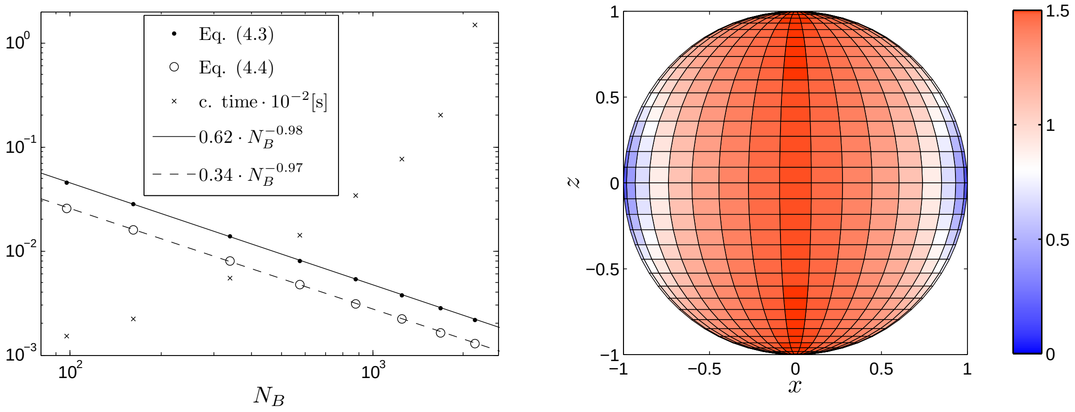

(a)

(b)

Figure 4.1: (a) A relative difference between computed and analytical solution of a potential and a velocity surface distribution for a sphere and an indicated computation time with respect to the number of panels N_B. (b) Velocity surface distribution over a sphere discretized into $N_B = 578$ panels.

4.2 Test Case No. 1: Laminar-Turbulent Transition

In the first test case an optimization of a surface of a human powered vehicle is treated (Fig. 4.2). Besides rolling resistance of the tyres, the fairing of this bicycle (propelled by a person lying inside) causes all the drag of the vehicle.

An optimization of the shape of the fairing should therefore notably improve the bicycle performance.

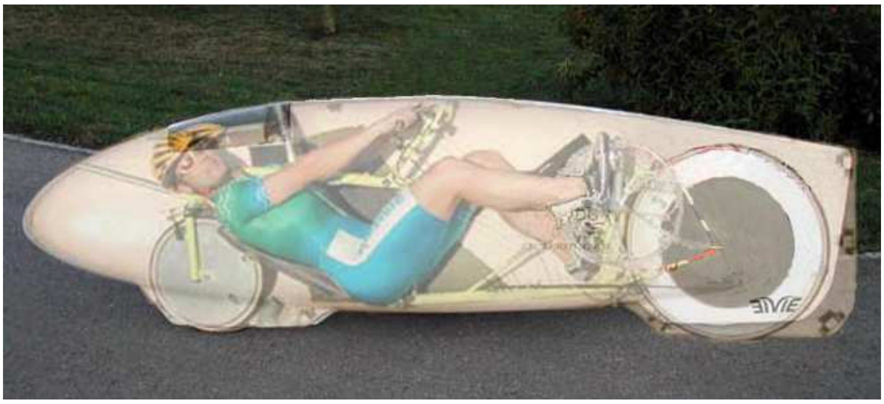

Figure 4.2: A bicycle propelled by a person lying inside a completely closed fairing.

The bicycle is usually driven under small cross-wind conditions, and since its shape is slender, the flow stays attached. The major component of a drag force is therefore skin friction, where the laminar-turbulent transition location plays a significant role on its size (Section 2.2). In order to reduce the skin friction drag, the laminar flow needs to be promoted as far back to the end of the bicycle as possible.

A favourable surface pressure distribution is therefore in pursuit, that will gradually accelerate the flow as long as possible and in a pressure recovery region not just prevent the flow from separation, but also thin the boundary layer. With a smoother pressure distribution, a smaller pressure drag can be attained. An average speed of the bicycle is 90km/h and its length is 2.5m, which means that it is driven approximately at $Re = 4.2 \cdot 10^6$. The wheels and their fairings aren't taken into the consideration in this test case.

4.2.1 Verification

In the optimization process a complete surface of the fairing is optimized, but because of the bilateral symmetry of the problem, the system of equations (Eq. (3.22)) needs to be written only for a half of the body. The ground effect is introduced through another symmetry plane at the ground level. The imaginary doublet distribution under the ground symmetry plane enables one not to include the ground surface into the simulation. In case of a real viscous flow, the turbulence produced at the ground is in this way neglected, but the results of the potential flow calculations aren't changed because of this simplification. Since we are more interested in a favourable pressure distribution and its influence on the transition position, the same simplification is used in CFD analyses.

In this test case a zero angle of attack is considered and since the shape has bilateral symmetry, there is no need for the wake to be modeled. A deformation vector points in direction of a surface normal at each node position (Fig. (4.3)). The deformation vector field is normalized in the middle of the body and gradually decreases to zero toward the nose and the trailing edge of the bicycle. This property is achieved by multiplying the normalized deformation vector field by a proper function, which alters the deformation vector field as

$$\mathbf{d}_{new} = \frac{u^2(1-u)^2}{(1/2)^4}\,\mathbf{d}_{old}, \tag{4.5}$$

where the surface coordinate $0 \leq u \leq 1$ runs along the body surface in a streamwise direction. The nodes at the nose and the trailing edge are in this way fixed and the length of the bicycle remains unaltered.

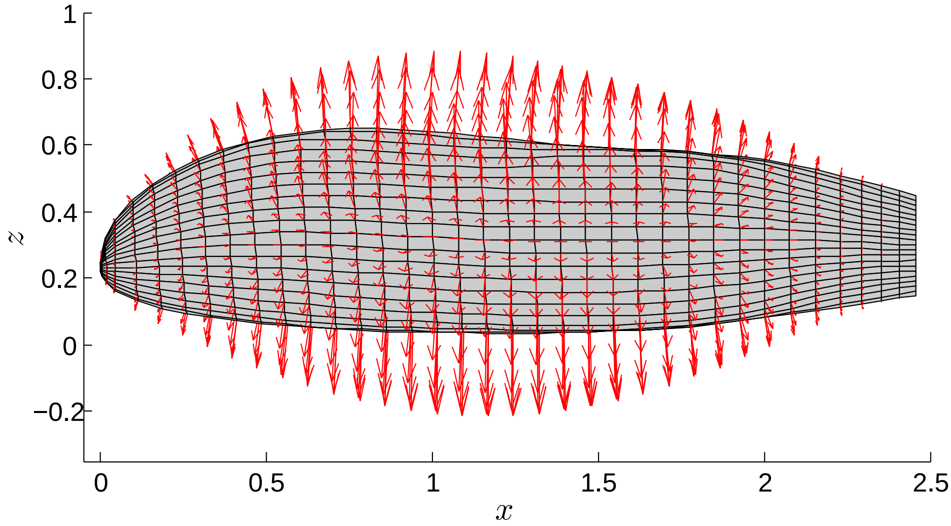

Figure 4.3: Deformation vector field scaled by a factor of 0.25.

In order for the fairing to enclose all the mechanical and structural parts, and also to give the cyclist enough space inside the fairing to sit, pedal and steer, geometrical constraints at some critical points are added to the problem. The constraints don't allow the surface to contract at these points, but the surface is free to expand everywhere. In the pressure recovery region the Stratford criterion constraint (Eq. (3.35)) is used in order to prevent the flow over the modified shape from separating. The "soft" maximum (Eq. (3.39)) is constrained with a concave pressure recovery critical Stratford number $G_M < 0.35$, where $a_0 = 130$, $a_1 = 0.2$ and $a_2 = 0.01$ are used. In this way the pressure recovery region takes a shape that allows the pressure to recover to the freestream value in as short distance as possible while remaining attached.

Since the pressure recovery region starts at approximately the same streamwise location over the whole body surface, the same constant integral from Eq. (3.36) is used for all recovery region panels. Its value is computed as an averaged integral value over three equally spaced surface streamlines that run from the nose of the body to the pressure recovery region. It is computed after a few steps of optimization (Subsection 3.2.3), averaged over all optimizations in this test case, and then used as a constant at all complete optimization procedures.

The magnitude of change surface function (Bézier surface) is at all optimization computations controlled with 12×7 number of control points, unless otherwise stated. Twelve points are in a streamwise direction and seven in its transverse direction. The size of all control points is completely unconstrained (undefined lb and ub in Eq. (3.26)).

One of the optimizations was first carried at three different numbers of surface panels in order to chose a proper surface mesh density for the rest of the optimizations. Relative differences of cost function values between the original and the optimized surfaces with respect to the number of surface panels is presented in Fig. (4.4(a)). A mesh density with $N_B = 720$ panels is a reasonable choice, because the relative difference of the cost function differs from the finer mesh result only by about 0.1%, the computation times, on the other hand, are reduced significantly. Similar search for an appropriate volume mesh density was done also for the CFD analysis, where computations were carried for an original surface at three different numbers of volume cells composing the mesh. The relative difference of forces between all meshes and a mesh with the highest density with respect to the number of cells is presented in Fig. (4.4(b)). A mesh with 17.3 million cells was chosen to be used at the rest of the simulations in this test case. With a finer mesh, the pressure force changes by 1.3%, whereas the friction and the lift force by less than 0.23%, which is an acceptable computation error.

An example of a volume mesh surrounding the original surface used for the CFD analysis is shown in a top view in Fig. (4.5(a)). A body surface and a slice through a volume field are coloured in pressure and magnitude of velocity colour schemes, respectively. Since a low Reynolds number $k - k_L - \omega$ turbulence model with no wall functions was employed for the CFD computations, a very

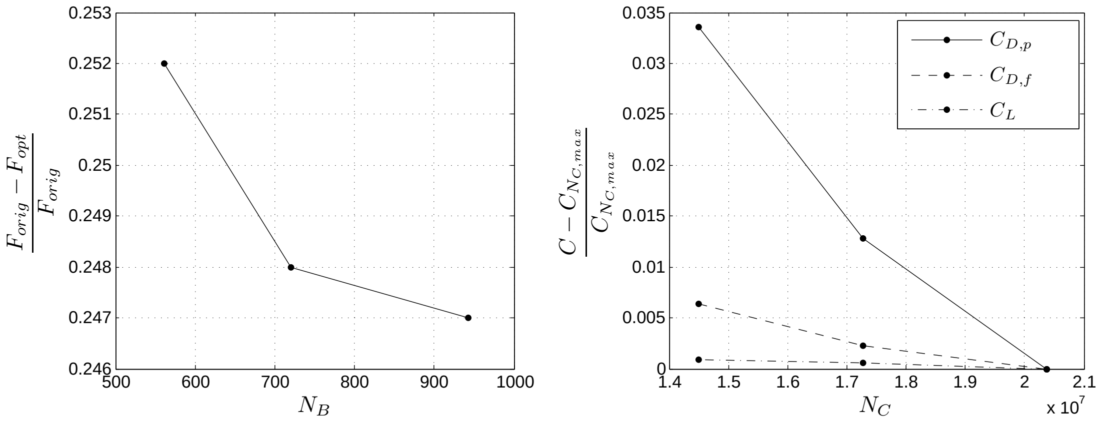

(a) (b)

Figure 4.4: (a) A convergence of a relative difference between initial cost function value and its minimized value with respect to the body surface mesh density at optimization process. (b) A convergence of the force coefficients with respect to the volume mesh density for the CFD analysis.

high density mesh had to be constructed at the body surface. Because of this, 15 layers of cells parallel to the surface shape were used to surround the whole body, whose thickness smoothly increases with factor 1.3 to the outer mesh size. A zoomed in part of a mesh right next to the surface wall coloured in a magnitude of velocity colour scheme is presented in Fig. (4.5(b)). A gradual increase of velocity from zero at the wall to the freestream velocity can be observed, which indicates a proper mesh density at the wall.

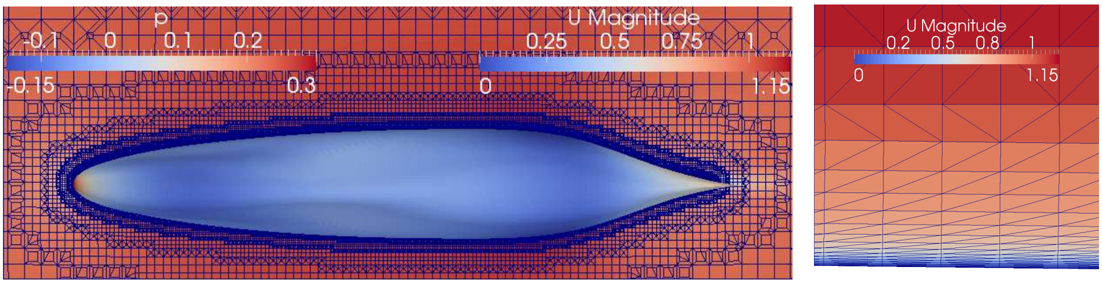

(a) (b)

Figure 4.5: (a) A slice through a mesh in a top view, surrounding the original surface, used in the CFD analysis. (b) High density wall mesh layers, coloured in magnitude of velocity colour scheme, smoothly increase to the outer mesh size.

As already stated, minimization of the cost function equal to the sum of pressure gradient reduces the variation of the pressure distribution in the flow around a body. Furthermore, giving the optimization method enough freedom to move surface nodes, a pressure distribution equal to undisturbed pressure p_∞ should result. In order to check if the proposed optimization method produces results according to this statement, an optimization without geometrical constraints was run. The deformation vector field pointed, only for this test, in the direction normal to the symmetry plane. The result of the optimization is presented in Fig. (4.6(a)). The optimization method produced the optimal result under the given circumstances. It flattened the fairing surface to coincide with the symmetry plane, which produced a freestream pressure distribution over all surface area. Consequently, a zero pressure drag and a minimal friction drag, due to the remaining of the surface, was achieved.

Giving the optimization method more freedom to move the surface nodes therefore produces a smaller cross section of the body. If the freedom is given through a larger number of control points (15 × 10), while still satisfying the geometrical constraints, a wave-like surface shape results. A front view of the optimized surface is presented in Fig. (4.6(b)). The surface embraces the constraint points (red dots in Fig. (4.6(b))), while at the same time tries to minimize the cross section of the fairing. The "amplitude" of the wave-like surface is not severe, because pressure gradients also in a direction perpendicular to the freestream are incorporated in the cost function.

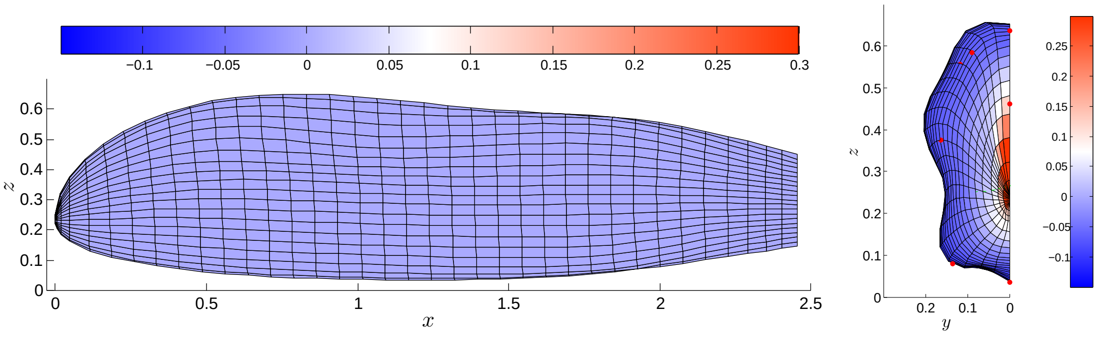

(a) (b)

Figure 4.6: A result of an optimization with (a) no geometrical constraints - flat surface coinciding with the symmetry plane, (b) larger number of control points - wave-like surface embracing the geometrical constraint points (red dots).

4.2.2 Results

The resulting optimal surfaces were evaluated using a CFD analysis. In order to simulate a natural transition from laminar to turbulent flow, a very small turbulence intensity (defined as the ratio of the root-mean-square of the velocity fluctuations to the mean freestream velocity) $I = 0.01\%$ and turbulent viscosity ratio (defined as the ratio of turbulent to laminar (molecular) viscosity) $\beta = 0.01$ were used at the inflow. The relative differences of drag and surface areas between original and optimal surfaces at different bias numbers and the corresponding pressure coefficient distributions over a streamline across all surfaces are presented in Fig. (4.7(a)) and Fig. (4.7(b)), respectively. A comparison of surface pressure distributions between panel method computations and CFD analyses for the original surface and the optimal surfaces at $b = 0$ and $b = -0.2$ are presented in Fig. (4.8), Fig. (4.9) and Fig. (4.10).

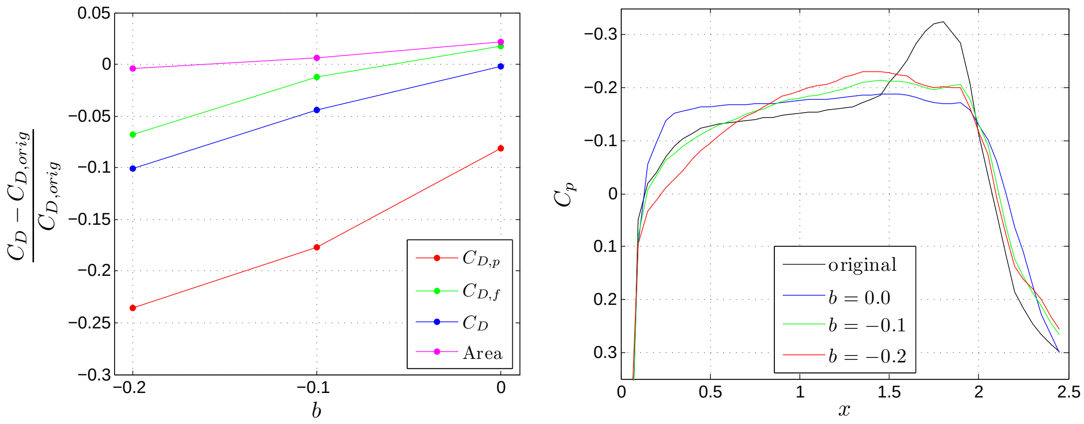

(a) (b)

Figure 4.7: (a) Relative difference of drag and surface areas of all optimized surfaces compared to the original surface, computed with OpenFOAM. (b) A pressure distribution over a streamline across the original and all optimal surfaces.

Surface area used in coefficient calculations is the area of the original surface shape. The streamlines (green curve) and the geometrical constraint points (red dots) are depicted in panel method calculation Figs. (4.8(a)), (4.9(a)) and (4.10(a)). The symmetry plane at all CFD calculations (Figs. (4.8(b)), (4.9(b)) and (4.10(b))) is coloured in magnitude of velocity colour scheme.

As can be seen from Fig. (4.7(a)), the pressure drag of solutions at all values of bias were reduced from 10% and up to 25%. Such a high pressure drag reduction becomes apparent by comparing surface pressure distributions of the original shape (Fig. (4.8)) and both optimal shapes (Fig. (4.9) and Fig. (4.10)). Instead of high and low pressure local regions at the original surface, a much steadier pressure distribution can be observed for the optimized shapes. A much

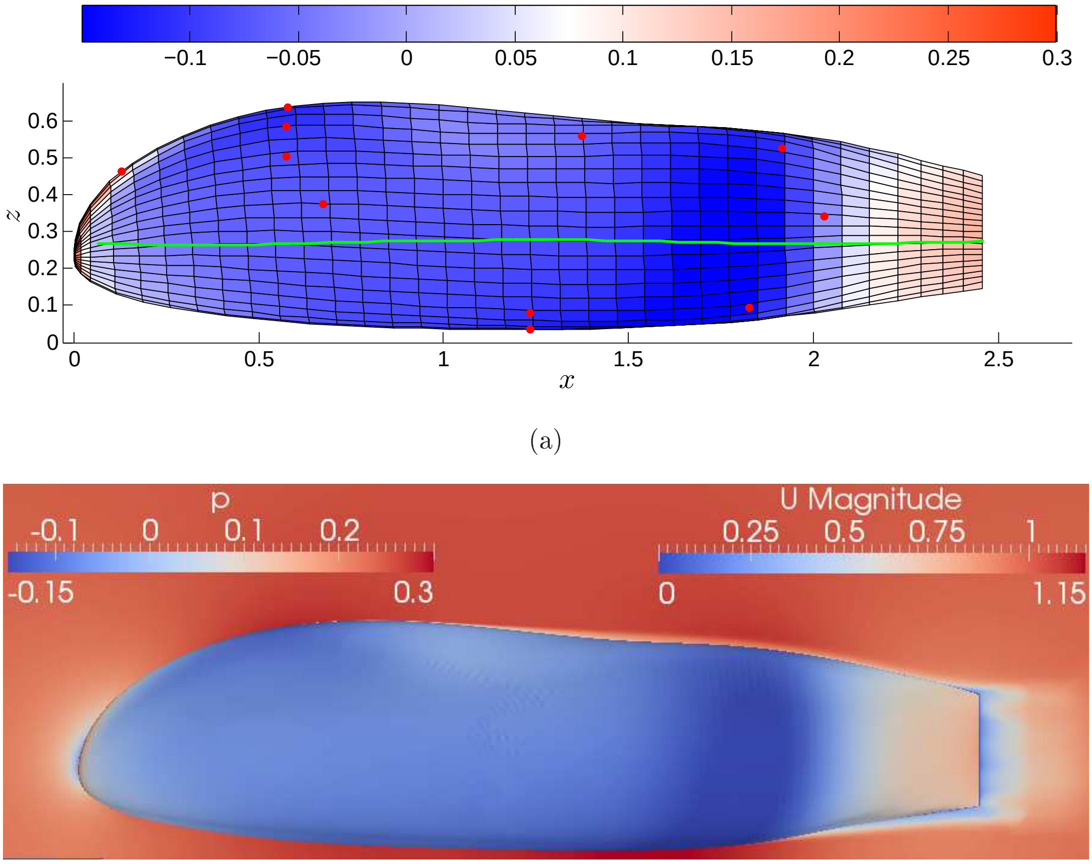

(a)

(b)

Figure 4.8: Surface pressure distribution of an original surface computed with (a) a panel method (b) a CFD analysis.

smoother pressure distribution reduces the amount of instabilities in the flow, which consequently also thins the boundary layer. A major contribution to the reduction of the pressure drag is also due to the unsatisfied Stratford criterion at the pressure recovery region of the original surface.

If a basic cost function in a form of a sum of pressure gradient distribution (Eq. (3.32)) is used, a minimization of its value produces a plateau-like pressure distribution in a streamwise direction across the body (blue curve in Fig. (4.7(b))). An even pressure distribution on a major part of the fairing can be also observed in Fig. (4.9). If a small bias is added to the pressure gradient in a streamwise direction (Eq. (3.34)), the plateau changes into a ramp-like pressure distribution (green and red curves in Fig. (4.7(b))). A gradual decrease of surface pressure up to the recovery region can also be observed in Fig. (4.10). The minimization would like to achieve as many panels with a pressure gradient value equal to bias as possible. In this way local acceleration and deceleration of the

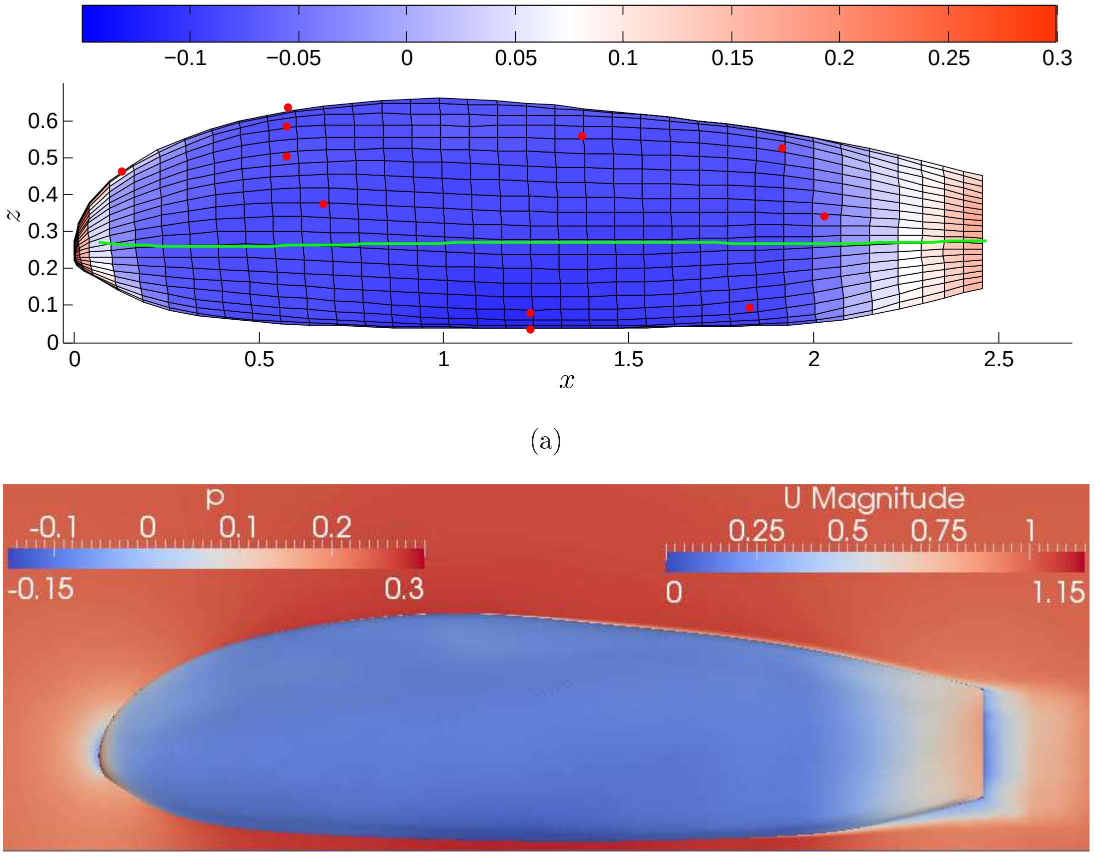

Figure 4.9: Surface pressure distribution of an optimal surface at $b = 0.0$ computed with (a) a panel method (b) a CFD analysis.

flow is reduced, but as a consequence of the geometrical constraint points, there are still some regional variances of pressure that can not get diminished.

How the optimization deforms the surface shape in order to achieve the plateau- and ramp-like pressure distribution can be observed in Fig. (4.11). The figure presents three horizontal slices through the flow passing the original and two optimal ($b = 0.0$ and $b = -0.2$) surfaces in a top view. The slices lie at the mid height of bodies and are coloured in magnitude of velocity colour scheme. At $b = 0.0$ (Fig. (4.11(b))) the optimization produced a blunt nose and an almost constant body thickness all the way to the recovery region, which moved all the acceleration of the flow to the front of the body. At $b = -0.2$ case (Fig. (4.11(c))) a much pointier nose and a gentle surface shape slope behind it can be noticed. In this way a gradual acceleration of the flow on first two thirds of the surface was achieved.

Another shape characteristic that can be observed in Fig. (4.11) is a smaller maximal width of optimal bodies compared to the original surface. The position

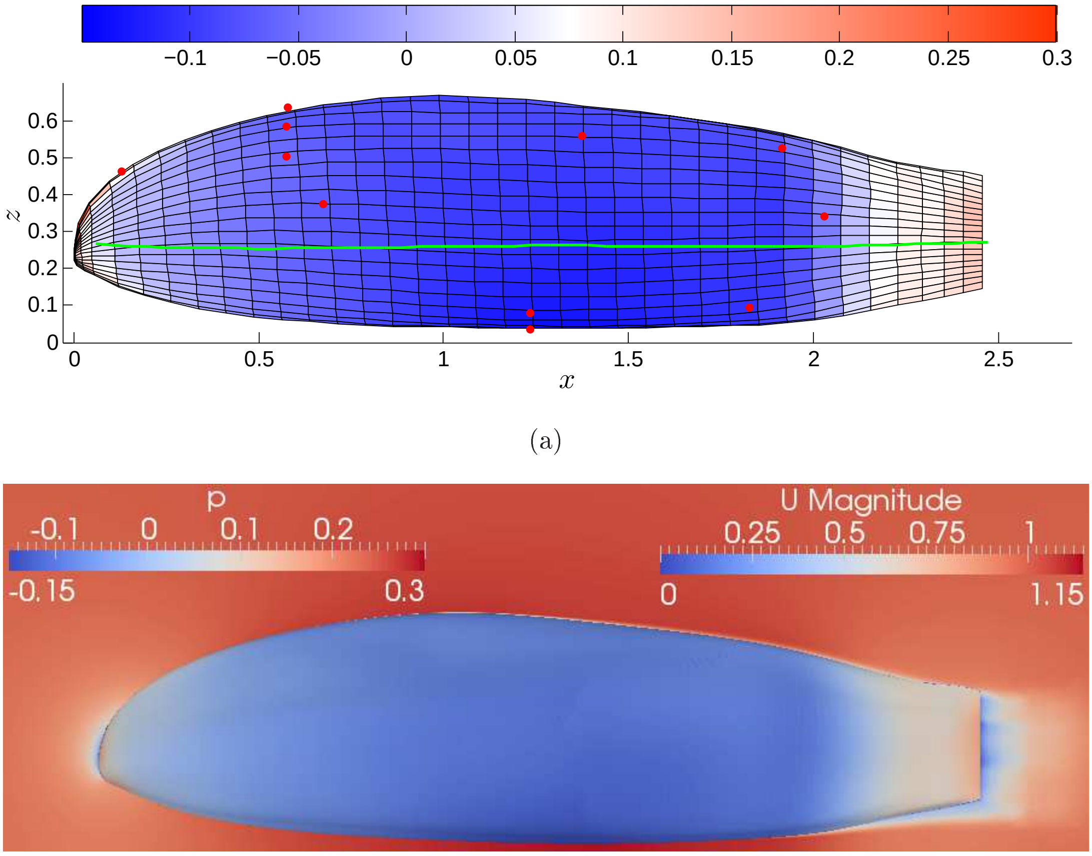

(a)

(b)

Figure 4.10: Surface pressure distribution of an optimal surface at $b = -0.2$ computed with (a) a panel method (b) a CFD analysis.

of the maximal width is also moved forward. In this way a high trough of negative pressure at approximately $x = 1.75$m of the original shape (black curve in Fig. (4.7(b))) is diminished and consequently a shorter recovery region achieved. For both optimal surfaces, a slightly thinner boundary layer with a faster flow at the recovery region was produced (Fig. (4.11)), which additionally helps to reduce the pressure drag. At the trailing edge of the body, on the other hand, the situation changes. Because of the larger trailing edge angle, the optimal surfaces produce slightly thicker boundary layer compared with the original surface.

A smoother flow influences also the amount of the friction drag. A favourable pressure distribution delays the formation of the instabilities, which postpones the transition from laminar to turbulent flow (Fig. (4.12)). The original and two optimized surfaces ($b = 0.0$ and $b = -0.2$) are coloured in inverse turbulent time-scale ω [56] colour scheme (denoted as omega in Fig. (4.12)), where a step in a value of ω indicates the point of transition. An average location of a transition is in the case of a $b = 0.0$ optimal surface at approximately the same longitudinal

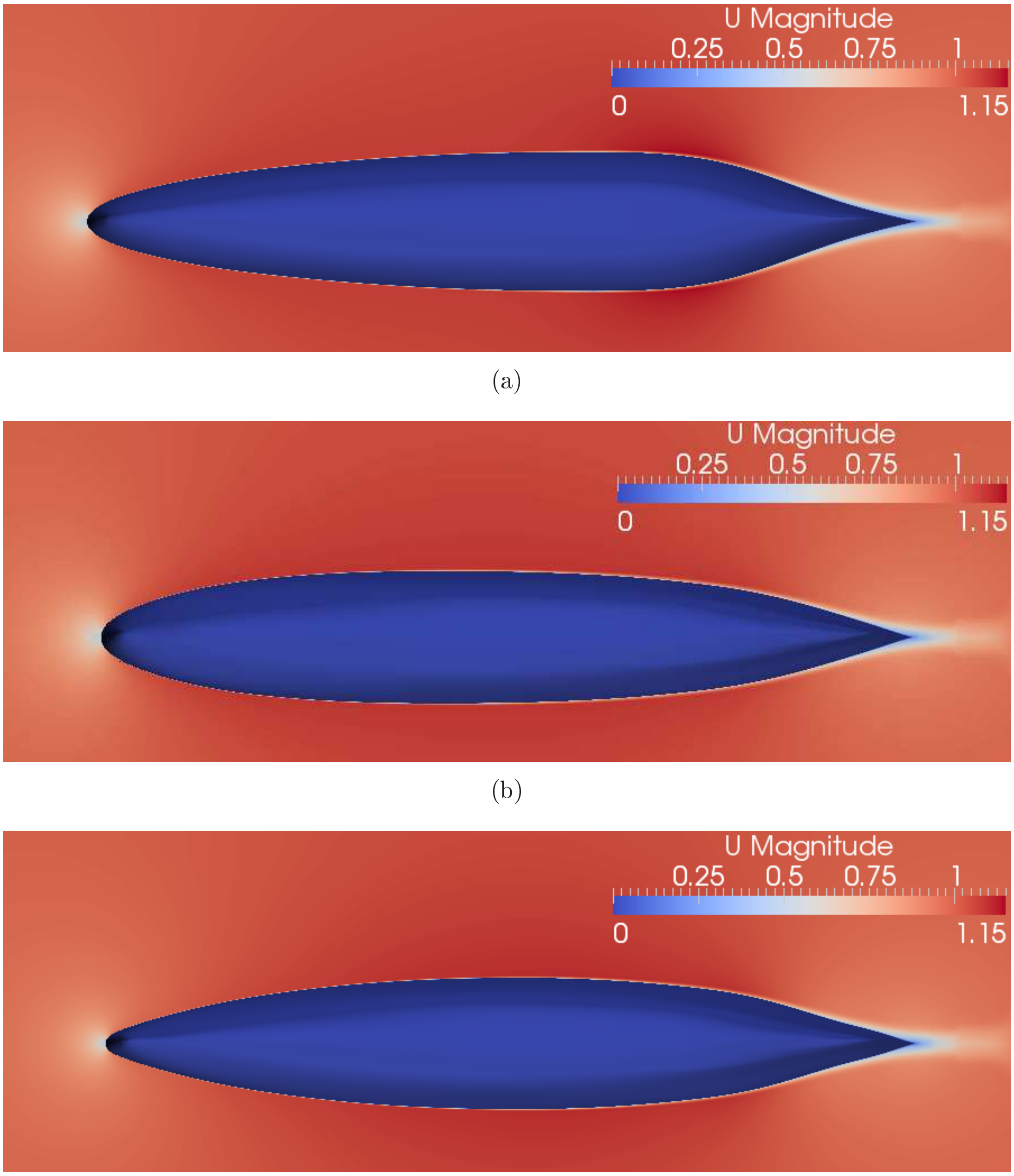

(a)

(b)

(c)

Figure 4.11: A horizontal slice through the flow passing the (a) original surface, (b) optimal surface at $b = 0.0$ and, (c) optimal surface at $b = -0.2$. The slices lie at the mid height of bodies.

distance x as in the case of an original shape. An increase of skin friction drag of an optimal surface at $b = 0.0$ is therefore a consequence of an increase of the surface area. The correlation of the two quantities is in this case obvious from Fig. (4.7(a)). At smaller bias numbers, on the other hand, the postponement of the transition impacts the amount of friction drag by a larger extent than the change of the surface area. The average location of transition for the optimal surface with $b = -0.2$ (Fig. (4.12(c))) is noticeably moved back to the end of the fairing compared to the original shape. Its skin friction drag is, mostly because of this reason, reduced by 7% (Fig. (4.7(a))).

At this test case it was shown, that proposed optimization method can be successfully used at reducing a drag force of a sleek body having an attached flow. The optimization produces a much smoother pressure distribution, which thins down the boundary layer and reduces the pressure drag. A favourable pressure gradient over a major part of the surface that postpones the transition and consequently reduces the amount of the friction drag, is possible by incorporating an amount of streamwise pressure gradient bias into the cost function.

4.3 Test Case No. 2: Wing-Root Separation

An optimization of a fairing that modifies the shape of the wing-fuselage junction is treated in this case. A shape of a wing-fuselage configuration was modeled, for which it was anticipated that it has problems with wing root flow separation as a cause of a wing-fuselage flow interference. With this test case it will be shown that the proposed surface optimization can be used to eliminate this massive root flow separation. Moreover, the resulting surfaces have similar features as proposed by numerous papers on the topic [59–62], that is, a smoother surface blending of a wing to a fuselage instead of a sharp corner junction, slight indenting of a fuselage over and under the wing, and a chord-wise extended wing leading and trailing edge in the root region.

The outer part of the wing experiences a freestream flow angle of attack decreased by the induced angle, as a consequence of a finite wing. On the other hand, the root part of the wing in reality feels an increased angle of attack, because of the cylindrical shape of the fuselage. At a moderate freestream angle of attack, the flow accelerates around the fuselage in the vertical direction and experiences the highest velocity right at the wing (for a mid wing-fuselage configuration). Because of this increase in the vertical component of velocity, the root of the wing flies at an effective angle of attack that is greater than the freestream one. This causes the flow to separate more readily even at moderate freestream flow angles of attack and at relatively smaller angles than the rest of the wing. Since the flow separation at the wing root propagates in a delta shape along the wing and the fuselage, it increases the drag substantially and can even reduce the responsiveness of the airplane control surfaces [63]. This effect should therefore

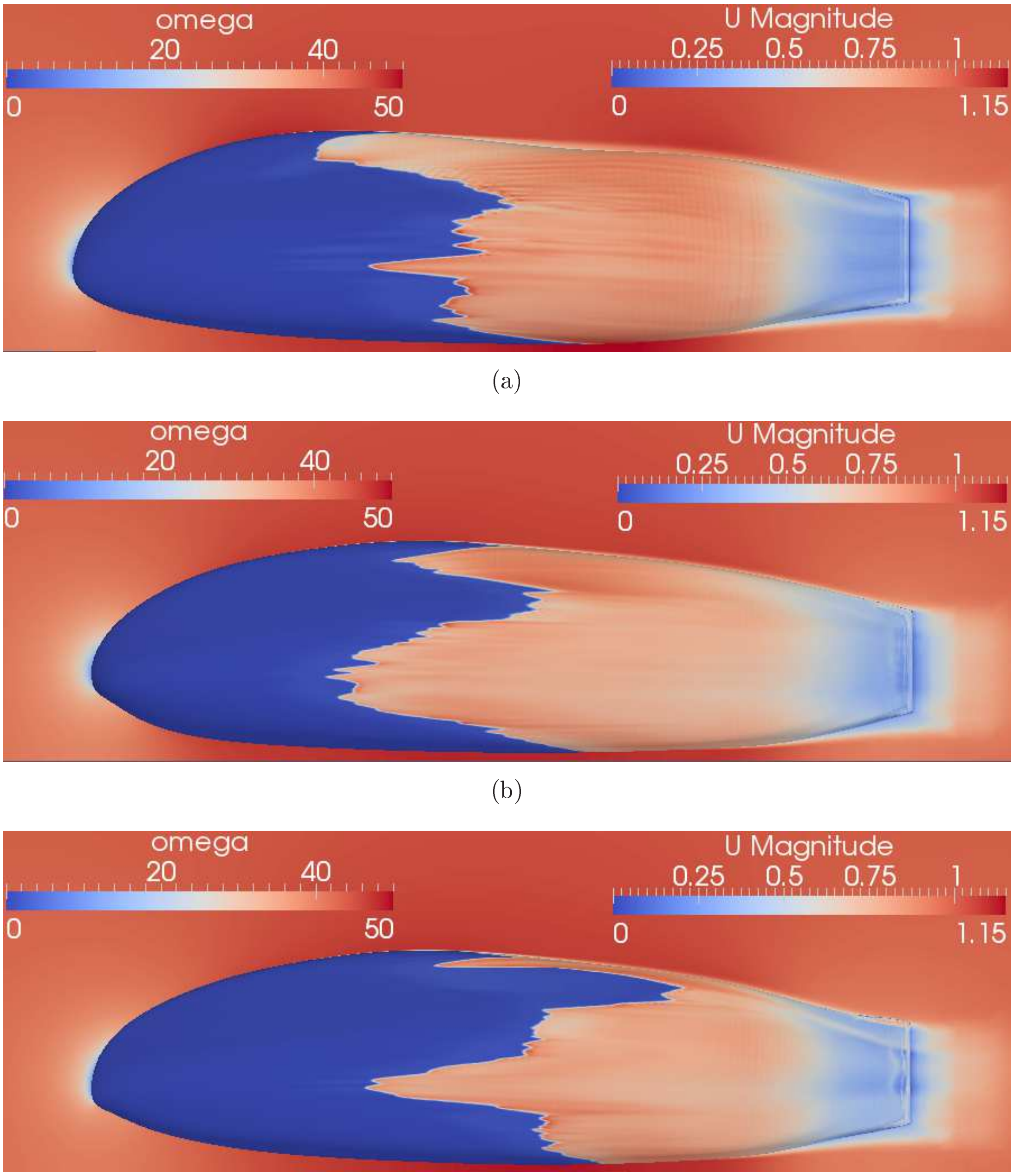

(a)

(b)

(c)

Figure 4.12: Surface distribution of inverse turbulent time-scale ω [56] for (a) original surface, (b) optimal surface at $b = 0.0$ and, (c) optimal surface at $b = -0.2$.

be avoided.

Even though the main goal of the second test case is to eliminate the wing root separation, the case is evaluated also at an angle off attack equal to zero. As it will be shown in this section, the optimization in case of $\alpha = 0$ reduces the pressure drag, but slightly increases the skin friction drag due to the increase of the surface areas.

4.3.1 Verification

The evaluated geometry has a bilateral symmetrical shape. The airfoil used at the wing design is on the other hand not symmetrical. In order to simplify the model, the tail isn't taken into consideration. Its absence has little influence on the solution, since its location is far from the fairing.

The case is considered as a lifting problem, where both the wing and the fuselage, because of their nonsymmetry and/or finite angle of attack, produce some amount of lift. This is why there is a wake modeled behind the whole body, but the Kutta condition is satisfied only on wing's trailing edge. For the fuselage, the assumption is made that it doesn't shed vorticity into the wake, which results in a constant doublet wake strength. The wake has a shape of an inclined flat plane that is leaving the trailing edge of the body along the wing's trailing edge bisector plane and extends approximately thirty wing-chord distances behind the body. The surfaces of the body and the wake are discretized into N_B and N_W panels, respectively. The surface mesh, where only the beginning of the wake is depicted, is presented in (Fig. (4.13)). The panels are coloured in doublet strength distribution for a zero angle of attack case. The wake doublet strength clearly shows its linear relationship to the bound circulation strength (Eq. (2.46)). Since the fuselage produces less lift compared to the root of the wing, its bound circulation must be, according to Kutta-Joukowski theorem, smaller, which means also a smaller absolute value of a doublet strength. A similar relationship can be written for the wingtip where the lift distribution goes to zero. As it can be seen in Fig. (4.13), at the end of the wing the doublet strength also goes to zero. On the other hand, the maximum absolute value of doublet strength lies at the wing span location with the maximum lift.

Since the main interest is eliminating the separation, the basic cost function (Eq. (3.32)) together with the Stratford separation criterion (Eq. (3.35)) is used in an optimization analysis. The Stratford constraint for the pressure recovery region has, in this case, a significant role in removing the separated flow. Even though a slightly higher critical Stratford number (Eq. (3.35)) of 0.50 is used to assure the convergence, favourable results are still achieved and will be presented. In this case $a_0 = 50$ is used in order to compute G_M (Eq. (3.39)). Since the pressure recovery region starts at different streamwise locations on the fairing surface, a linearly decreasing value of the integral from Eq. (3.36) is used for recovery region panels, where the maximum is at the fuselage and the minimum

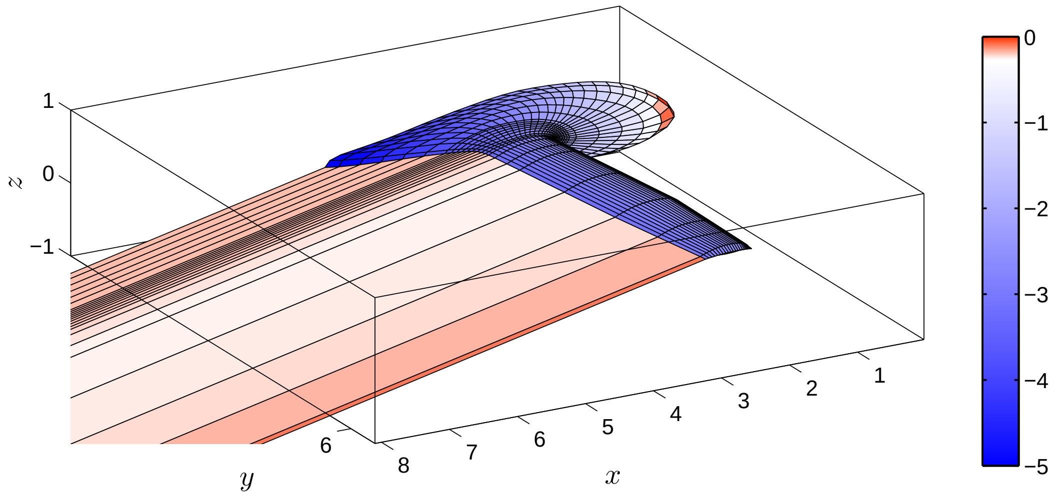

Figure 4.13: Body and wake doublet distribution at $\alpha = 0°$, computed with panel method. Only a part of the wake is presented.

at the wing. The minimal integral value is computed as an integral over the streamline at the wing-fairing junction that runs from the point right above the stagnation point to the pressure recovery region. The maximal integral value is on the other hand computed as an integral over the streamline that runs from the nose of the fuselage to the pressure recovery region on the fairing-fuselage junction. They are computed after a few steps of optimization (Subsection 3.2.3), averaged over all optimizations at the same angle of attack and used as a constant at all complete optimization procedures at the same angle of attack.

In all optimization computations, unless otherwise stated, 12×4 number of control points in order to compute the magnitude of change surface function (Eq. (3.28)) is used, of which twelve are around the fairing in a streamwise direction and four are in a spanwise direction. All control points are slightly constrained ($lb = -0.4$m and $ub = 0.4$m in Eq. (3.26)) in order to prevent coincidence of nodes and also to assure a physically acceptable surface shape.

The deformation vector of each node on the fairing that is being optimized points in the spanwise direction (Fig. (4.14)), which preserves the geometry of the wing. Vectors in nodes, that lie close to the leading edge of the wing point in direction of the leading edge, whereas vectors that lie close to the trailing edge point parallel to the trailing edge direction. Vectors are normalized, but on the half of the fairing closer to the fuselage ($0 \leq u \leq 0.5$) multiplied by a decreasing function (Eq. (4.5)) in order to remain tangential to the fixed fuselage surface.

In order to achieve a proper precision of the results, the optimization of a case at a moderate angle of attack ($\alpha = 8°$) has been run at three different

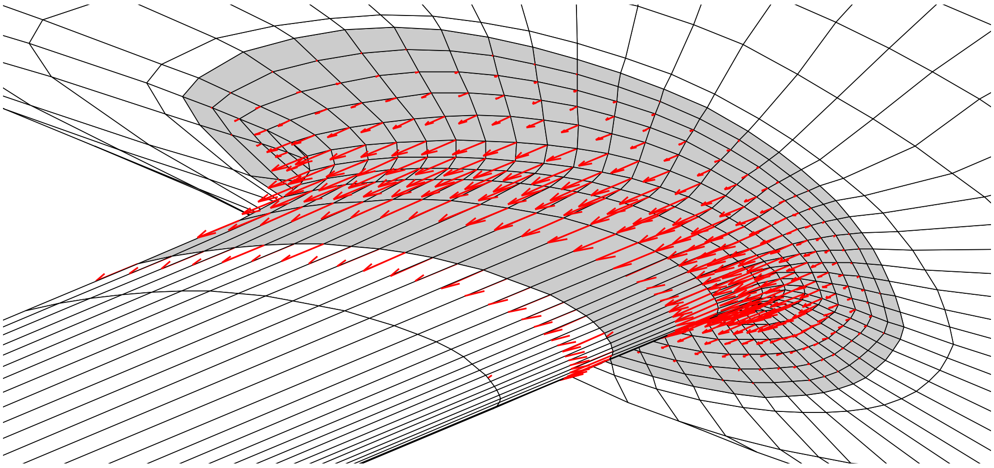

Figure 4.14: Patch that is being optimized (grey panels) and its deformation vector field scaled by a factor of 0.125 (red vectors).

surface mesh densities. After a comparison of a relative difference between the initial value of the cost function and its final converged value for different mesh densities (Fig. (4.15(a))), a mesh with a number of panels equal to $N_B = 1150$ was chosen for all optimization computations. In this way the results differ from the finer mesh results only by a few tenths of a percent, but the computation times are reduced significantly.

All optimization results at all chosen angles of attack together with the original surface shape have been verified in a CFD analysis using the OpenFOAM program. A proper volume mesh density had to be chosen also for the CFD analysis. An airflow around one of the optimal surfaces at an angle of attack equal to $8°$ with three different mesh densities has been simulated. A relative difference of pressure and friction drag coefficient and lift coefficient between simulations with different mesh density and a simulation with the highest mesh density is presented in Fig. (4.15(b)). From the figure it can be seen that the case with approximately five million cells is a reasonable choice for the simulation, since all the coefficients change less than 0.2% if the mesh gets refined even further. The same number of cells was used at the rest of the simulations in this test case. Since a high Reynolds number Spalart-Allmaras turbulence model was used, a value of y^+ [64] was also checked after choosing the mesh density. A y^+ surface distribution together with a slice through a mesh coinciding with the symmetry plane is presented in Fig. (4.16). The values of y^+ confirm an appropriate surface mesh density choice.

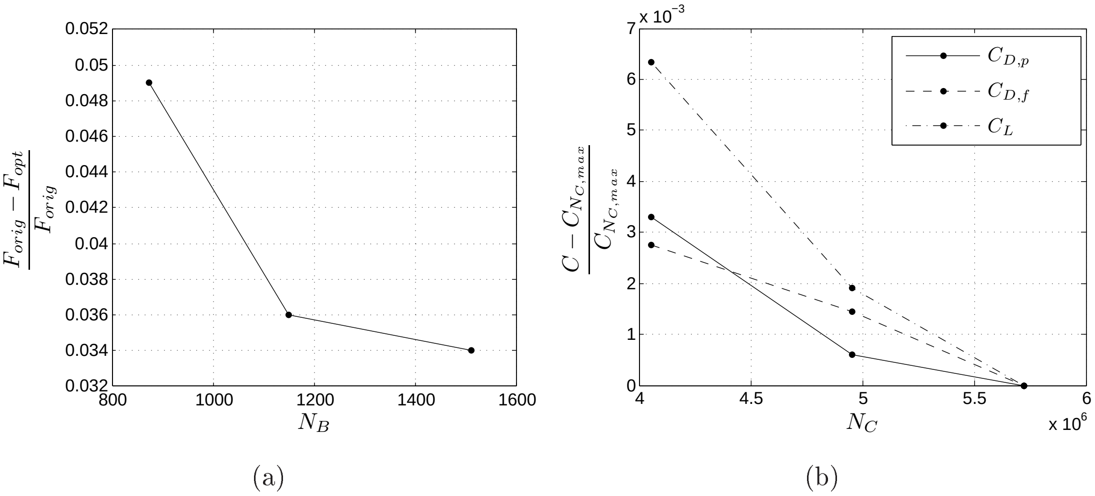

Figure 4.15: (a) A convergence of a relative difference between initial cost function value and its minimized value, with respect to the body surface mesh density at optimization process. (b) A convergence of the force coefficients with respect to the volume mesh density at CFD analysis.

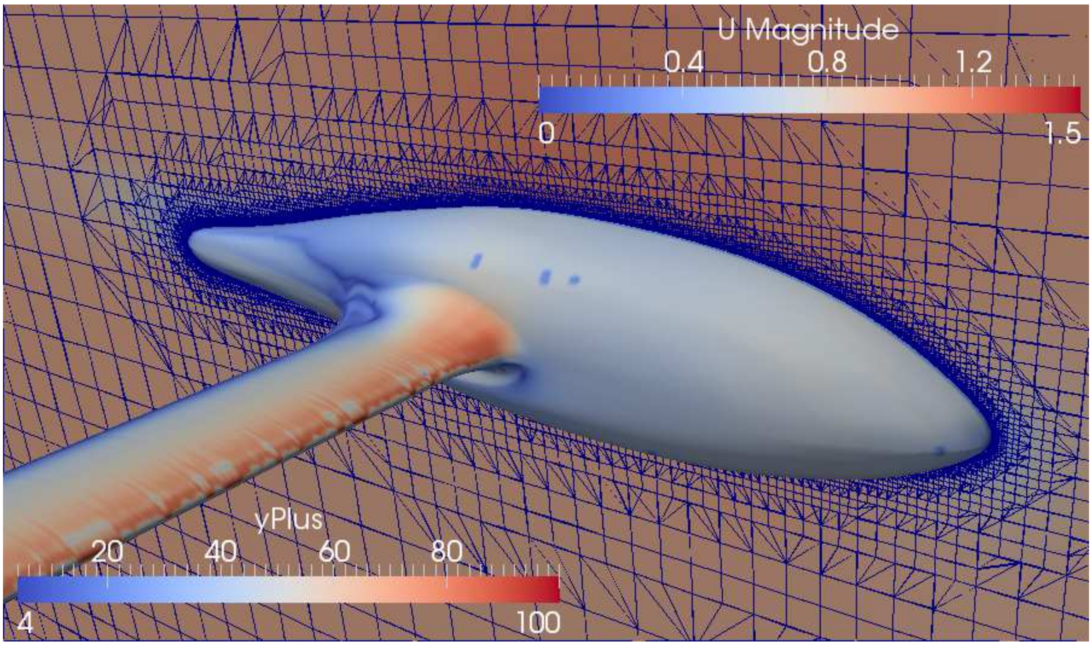

Figure 4.16: y^+ surface distribution and a slice through a mesh of a converged simulation of an airflow around one of the optimized surfaces at 8° angle of attack.

4.3.2 Results

The optimization of the fairing has been run at different combinations of two angles of attack, $\alpha_1 = 0°$ and $\alpha_2 = 8°$. The sum of cost function values at both angles has been weighted according to equation

$$(1 - w) \cdot F_{\alpha_1} + w \cdot F_{\alpha_2}. \tag{4.6}$$

If the weight w is equal to zero, the case is being optimized only at an angle of attack α_1, whereas if the weight is one, only the α_2 case is being optimized. Besides zero and one, three additional weights have been used in this work, 0.25, 0.5 and 0.75.

First, the optimized surfaces at weights $w = 0$ and $w = 1$ have been sought, where the original surface was used as an initial condition of the optimization process. These two optimized surfaces were then used as an initial condition at the rest of the values of weight w. Therefore, there are two families of solutions. One where the initial surface was the optimal surface at α_1 ($w = 0$) and the other with the initial surface being the optimal surface at α_2 ($w = 1$).

All optimized surface shapes at all values of weight together with the original surface have then been evaluated with CFD analysis. The relative difference of pressure, friction and total drag between the original and optimal shapes is at angle of attack $\alpha_1 = 0°$ presented in Fig. (4.17(a)) and at $\alpha_2 = 8°$ in Fig. (4.17(b)).

The two families of solutions are presented with the same colour, but with a different line style. Solutions that have a $w = 0$ optimal shape as an initial condition are connected with a solid line to their initial condition, and solutions with a $w = 1$ optimal shape as an initial condition are connected with a dash-dot line to their initial condition.

At both angles of attack, the solution $w = 0$ and the solutions that derive from it have smaller pressure and total drag, but larger friction drag compared to the solution $w = 1$ and solutions with $w = 1$ as an initial condition. It can be also seen from Fig. (4.17), that all solutions have larger friction drag compared to the original shape. In order to find an explanation for the friction drag increase after the optimization, the surface areas of the whole body (fuselage, wing and fairing) of all solutions have been plotted in Fig. (4.17) in order to compare them with the friction drag. It can be seen from the figures, that the two relative differences have a good correlation at $\alpha_1 = 0°$ and a poor one at $\alpha_2 = 8°$. The difference

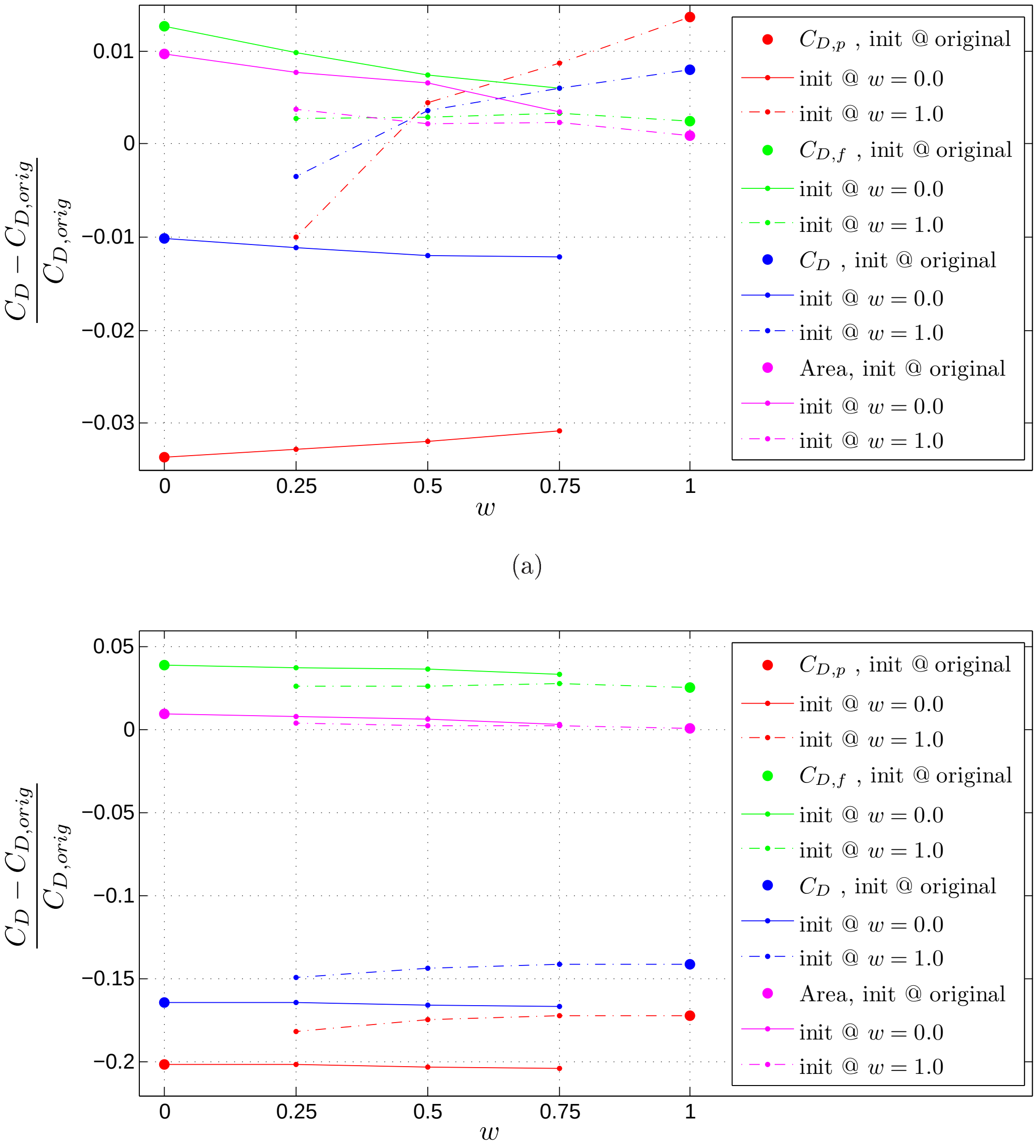

(a)

(b)

Figure 4.17: Relative difference of drag and surface area of all optimized surfaces compared to the original surface, computed with OpenFOAM at angle of attack equal to (a) $\alpha_1 = 0°$ and (b) $\alpha_2 = 8°$.

between the relative increase of the area and the friction drag is at α_1 smaller than 0.3%, whereas at α_2 approximately 3%. The frictional component of the drag at zero angle of attack therefore increases mainly because of the increase of the wetted surface.

On the other hand, at moderate angles of attack, where the separation occurs at the wing root region, the increase of the area only slightly influences the amount of the friction drag. At the separated region, the flow velocity at the surface is small or can even have an opposite direction. After optimization, the flow is attached to the surface, its velocity at the surface significantly increases, which produces the major part of the friction drag increase.

Even though the friction is amplified at all optimized shapes, the thinning of the boundary layer, as a result of the pressure gradient minimization, still influences the amount of total drag at both angles of attack by a larger extent. The boundary layer and the wake are much thinner at $\alpha_2 = 8°$ because of the reattachment of the flow, which results in more than 20% of decrease in pressure drag and consequently in more than 16.5% of decrease in total drag for $w = 0$ solution and all of its three derivatives.

The exceptions at zero angle of attack are the $w = 1$ solution and its two closer derivatives at $w = 0.5$ and $w = 0.75$. The optimized shape of these solutions bulked up on the upper front region of the fairing, which reduced the recovery region behind the new bulge and assured an attached flow. At zero angle of attack, on the other hand, this bulge increased the recovery region, which thickened the boundary layer and produced more pressure drag than the original surface.

It is also interesting to note that the optimized shape at $w = 1$ for the angle of attack $\alpha_2 = 8°$ is poorer than the solution at $w = 0$ and all of its derivatives. Since the problem has at least two local minima solutions, the choice of an initial condition plays an important role at optimization process.

Comparing pure drag data does not, however, reveal the whole picture. It must also be determined how the optimization effects the lift force. The data for three different surface shapes has been presented on the polar plot in Fig. (4.18). Besides the original shape, an optimal shape with a minimal total drag at both angles of attack ($w = 0.75$, initial condition at $w = 0$) and an optimal shape at $w = 1$ have been chosen to be compared. A surface area used in coefficient calculations is the area of a planform of the original wing stretched tangentially to the symmetry plane at the middle of the fuselage. The dots in the figure denote the drag and the lift coefficients at angles of attack equal to 0°, 6° and 8°. For the original surface additional simulations have been run at angles of attack equal to 7° and 9°, but the data for the latter angle is off the plot. A fit with a polynomial curve of degree of four for each data group was added to the figure, where data only at the smaller three angles of attack was used on the original surface. It can be seen from the Fig. (4.18), that the drag of the original shape dramatically increases and the lift decreases at angles greater than 7° ($C_D > 0.058$). At these angles the massive separation occurs, which completely changes the airflow over

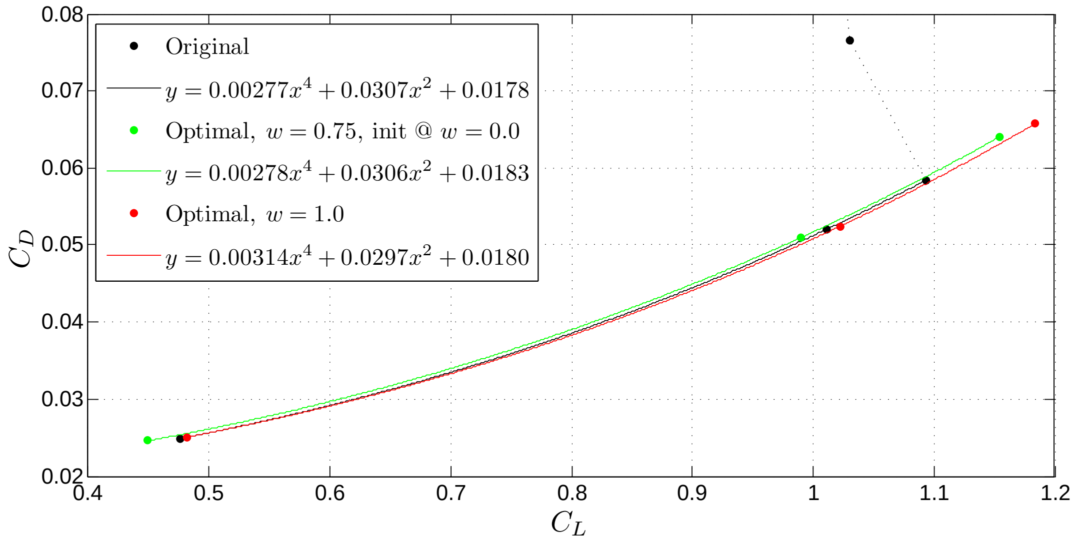

Figure 4.18: Polar plots for an original and two chosen optimal surface shapes. The data at different angles of attack is fitted with a polynomial curve of degree of four.

the fairing. At the optimized shapes, on the other hand, no separation occurs.

Even though the polar of the $w = 1$ solution is shifted to higher drag coefficients compared to the other two surfaces, it is also shifted to higher lift coefficients. By comparing the polar curves in the Fig. (4.18) it can be stated, that the solution at $w = 1$ produces the least drag of the three at the same amount of lift. Although the $w = 0.75$ solution has the smallest drag at all observed angles of attack, the $w = 1$ solution is still a preferred one to be used on the airplane due to its better polar. The fact that at the same lift a smaller drag can be achieved is the most important achievement at the surface optimization of a lifting body.

A comparison of a surface pressure distribution between the panel method computations and the CFD analysis for the original surface and the optimal surface at $w = 0.75$ (initial condition is a solution at $w = 0$) at zero angle of attack are presented in Fig. (4.19) and Fig. (4.20), respectively. Pressure distributions obtained with the panel method and CFD calculations are comparable even though a much coarser surface mesh is used at the former method. The surface optimization produced an indent fairing at the fuselage-wing junction, as can be seen from the shape of the white line in Fig. (4.20). Since the flow is accelerated around the wing and at the same time around the fuselage, an unnecessary high speed flow is achieved at the original fairing, which causes an additional amount of drag (Section 2.2). This effect is reduced at the optimized surface, where a slightly larger pressure is achieved at the observed region. The drag reduction

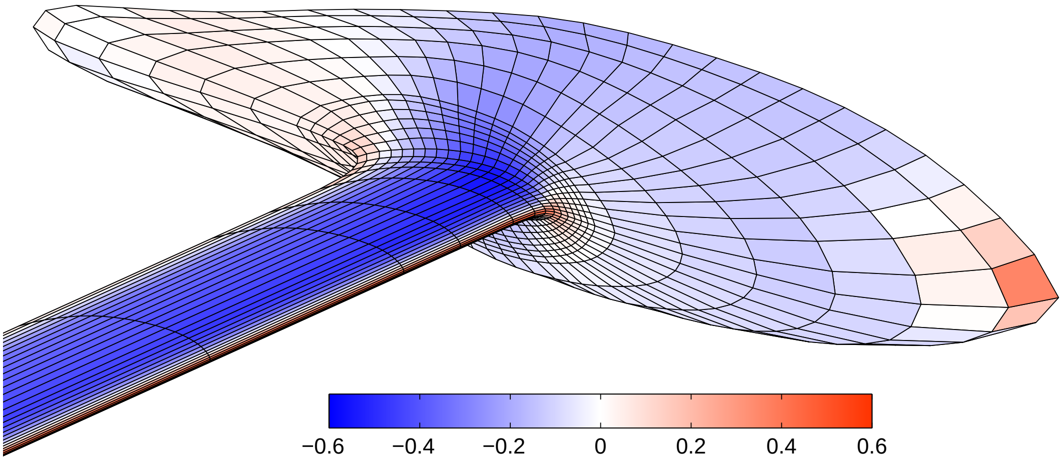

(a)

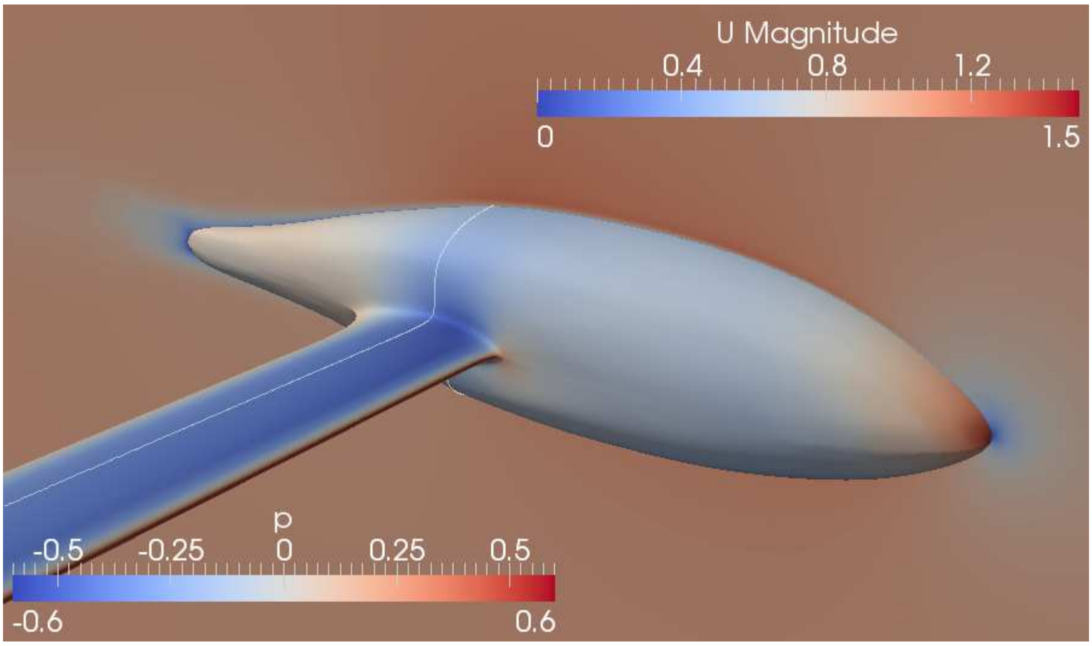

(b)

Figure 4.19: Surface pressure distribution of an original surface computed with (a) a panel method and (b) a CFD analysis at zero angle of attack.

can be observed in Fig. (4.17(a)).

The pressure distributions for the same two surface shapes and additionally also for the optimized shape at the $w = 1$, computed with the panel method and CFD calculations, but this time all at the angle of attack equal to 8°, are presented in Fig. (4.21), Fig. (4.22), and Fig. (4.23), respectively.

The pressure distributions between the panel method and the CFD analysis are again comparable, with an exception of the original shape around the fairing. The panel method predicts a smooth and attached potential flow (Fig. (4.21(a))),

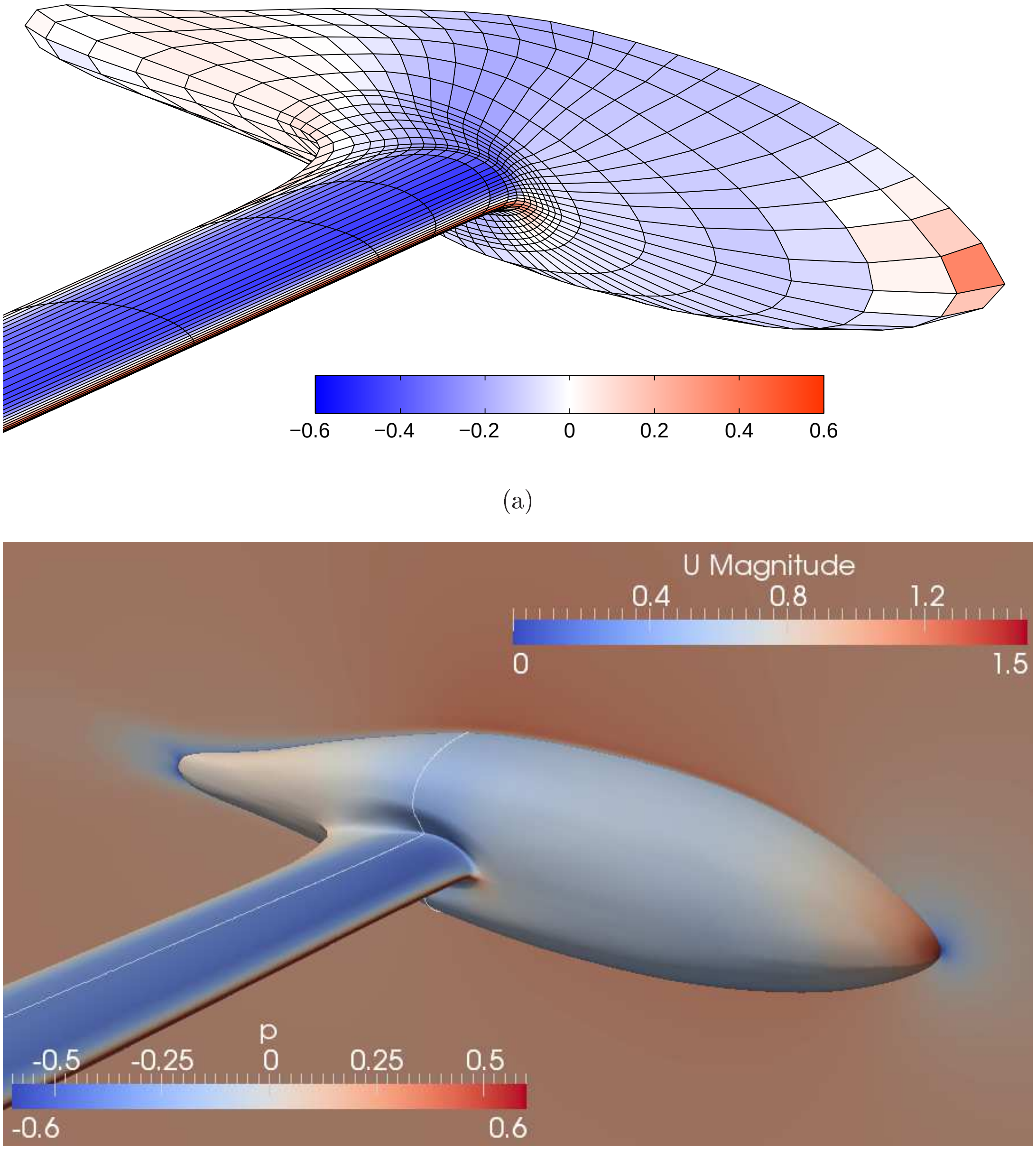

(a)

(b)

Figure 4.20: Surface pressure distribution of an optimal shape at $w = 0.75$ with an initial condition of a $w = 0$ shape, computed with (a) a panel method and (b) a CFD analysis at zero angle of attack.

whereas the CFD analysis calculates a huge separation at the wing-fuselage junction (Fig. (4.21(b))). A bundle of streamlines, coloured in a magnitude of velocity colour scheme, is added to all CFD analysis figures in order to emphasize the improvement of the optimized surfaces with respect to the original one at the 8° of angle of attack. For the original shape the streamlines detach from the surface already at the beginning of the wing, very close to the leading edge. At both optimized shapes, on the other hand, the streamlines remain attached all the way

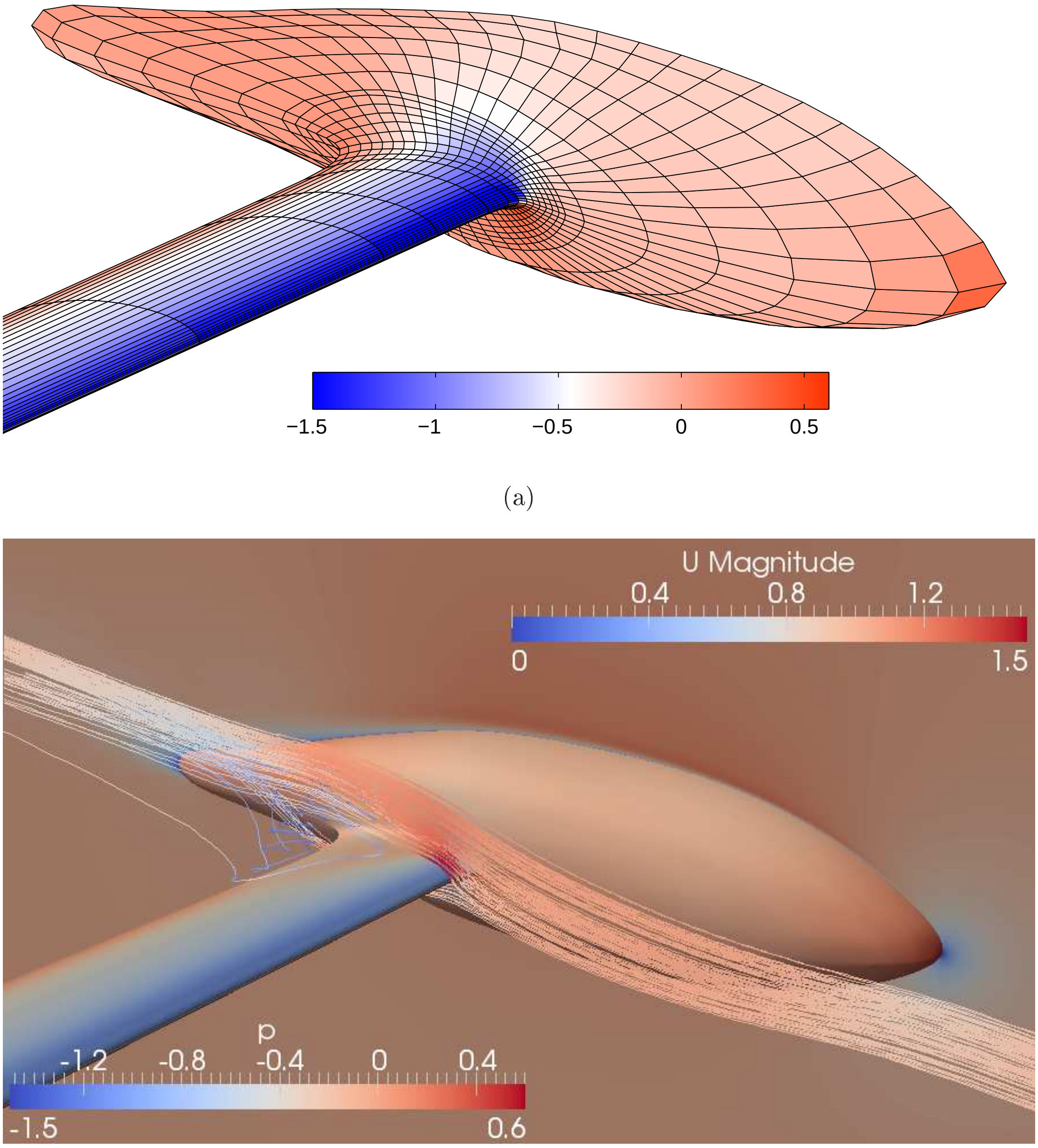

(a)

(b)

Figure 4.21: Surface pressure distribution of an original surface computed with (a) a panel method and (b) a CFD analysis at angle of attack equal to 8°.

to the trailing edge and only a small separation can be observed. Despite some separation, the flow is smoothly passing a major part of the body. The aerodynamics of the airplane are improved, as can be seen also from Figs. (4.17(b)) and (4.18).

At all the CFD calculation figures a slice, coinciding with the symmetry plane, with a velocity magnitude distribution is added. At some figures also a white line on the surface in a spanwise direction is added in order to have a better perception

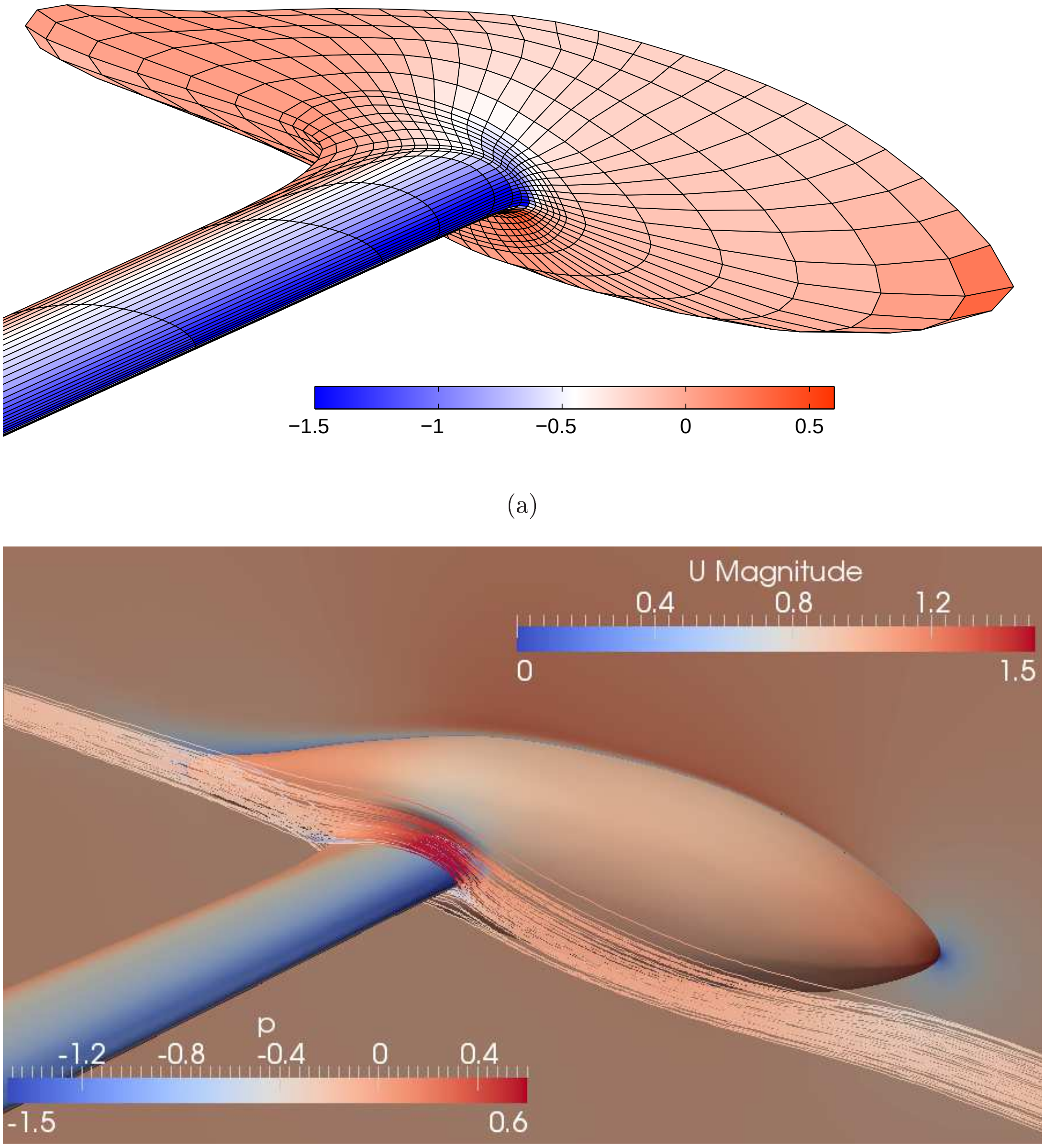

(a)

(b)

Figure 4.22: Surface pressure distribution of an optimal shape at $w = 0.75$ with an initial condition of a $w = 0$ shape, computed with (a) a panel method and (b) a CFD analysis at angle of attack equal to 8°.

of the surface shape. The shape of the fairing at the bottom side is qualitatively the same for all optimal cases. The surface at the fuselage is slightly indented compared to the original shape (Fig. (4.24)), which slows down the flow and helps to improve the characteristics of the fairing.

At this test case it was shown that the proposed optimization can be used to get rid of the massive separation in the wing root region. In this way, a significant reduction of drag is achieved. Whether the shape will indent in the fuselage in

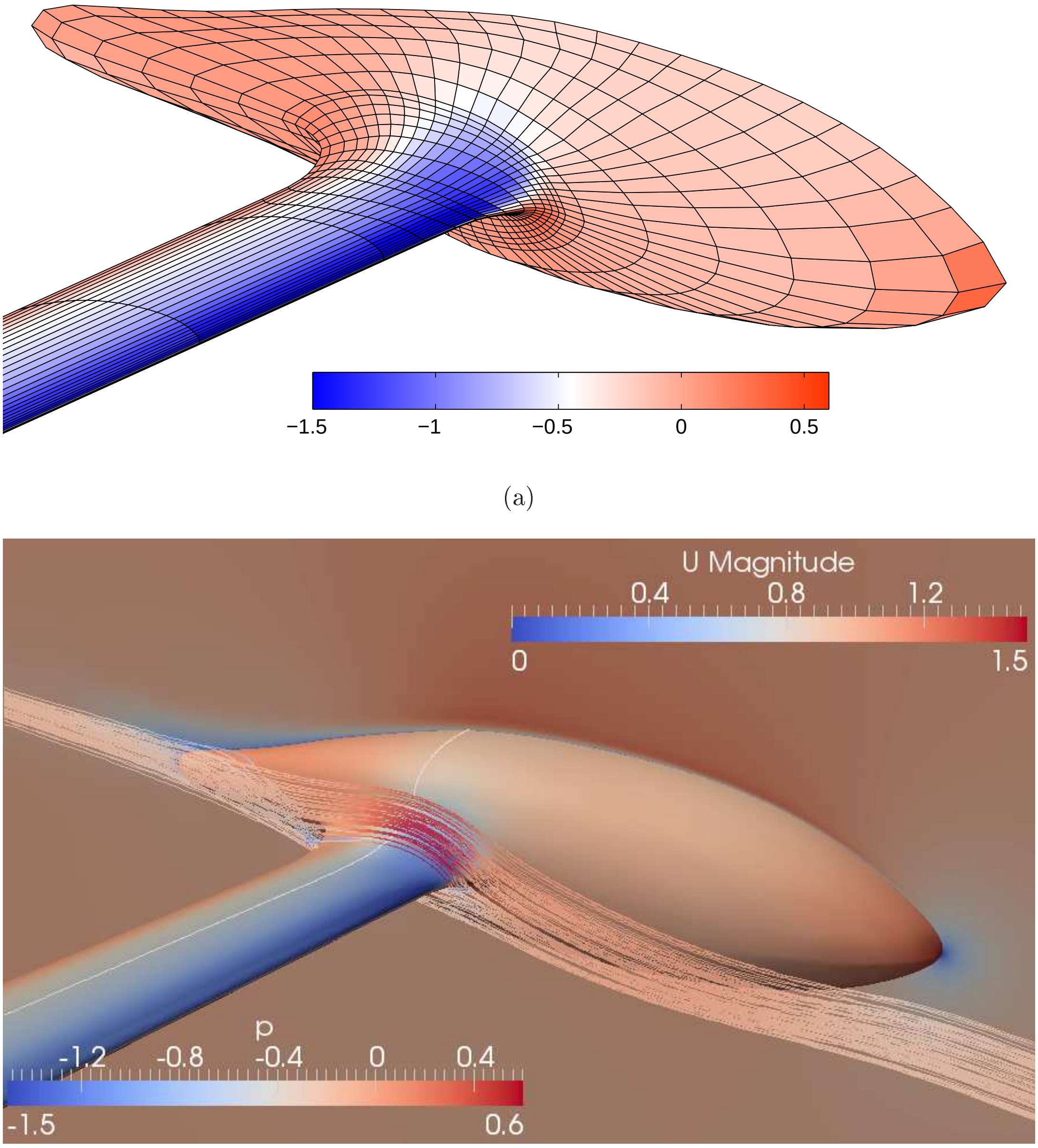

(a)

(b)

Figure 4.23: Surface pressure distribution of an optimal shape at $w = 1$ with an initial condition of an original shape, computed with (a) a panel method and (b) a CFD analysis at angle of attack equal to 8°.

order to decelerate the flow or bulge out in order to reduce the recovery region depends primarily on the shape used for the initial condition. In this work two families of solutions were encountered, which proves the importance of the initial condition in the optimization process.

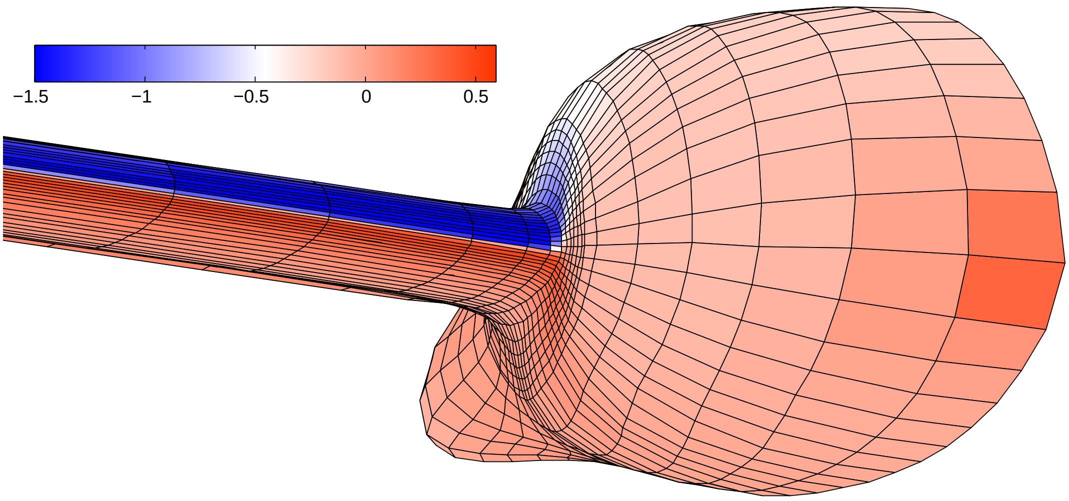

(a)

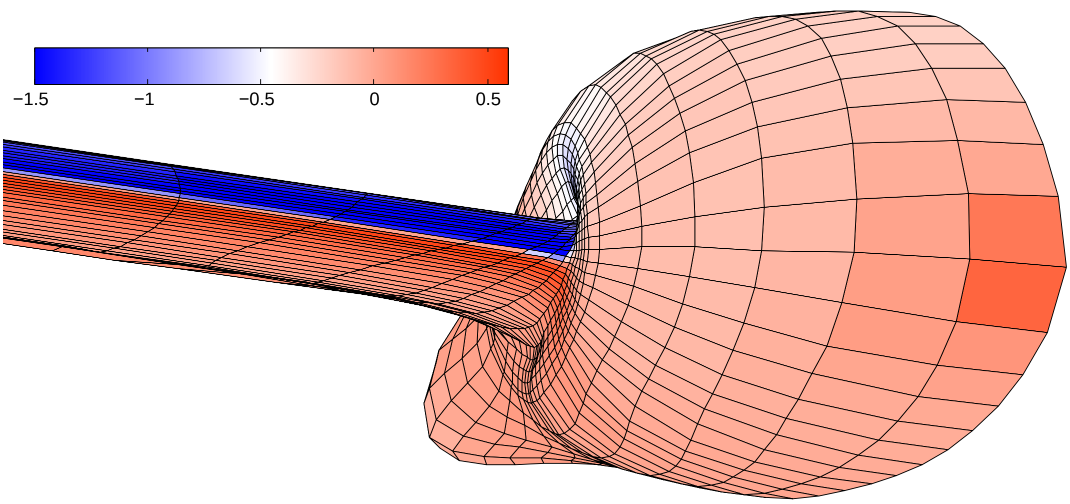

(b)

Figure 4.24: Surface pressure distribution of (a) an original shape and (b) an optimal shape at $w = 0.75$ with an initial condition of a $w = 0$ shape, computed with a panel method at an angle of attack equal to 8°.

4.4 Test Case No. 3: High Reynolds Number

In the last test case, the bulb keel of a sailboat is treated. More specifically, the two fairings between the hull and the fin and between the fin and the bulb are optimized. This test case distinguishes itself from the previous cases by having a greater Reynolds number. Even though a typical velocity is small compared to previous cases, because of the water as a medium of the flow, the Reynolds number is equal to or greater than 10^7. Large Re numbers cause an earlier transition than do smaller Re numbers, which means that turbulent flow is present more or less throughout the whole surface area. Because of this, the amount of wetted area and the surface velocity should be kept as small as possible in order to reduce the drag.

4.4.1 Verification

The body has a bilateral symmetrical shape which is preserved during surface optimization. The problem is treated at small angles of attack, $\alpha = 4^\circ$ and smaller, where typical cruise takes place. Only the surface of the hull under the waterline is taken into consideration, where the water level is considered as a symmetry plane. The waves aren't taken into account. The roll angle of the sailboat, as a consequence of the force in the sails, is also not taken into consideration in this work.

Since most of the flow is turbulent in this test case, its velocity should be as small as possible and unnecessary accelerations and decelerations should be avoided. That is why a basic cost function (Eq. (3.32)) is used, which causes almost an uniform pressure distribution and in this way the smallest negative pressure.

In all optimization computations 14×6 number of control points are used to compute the magnitude of change of the surface function (Eq. (3.28)). 14 are used in the streamwise direction around each of the two fairings and 6 are used in the spanwise direction. All control points are slightly constrained ($lb = -1.0$m and $ub = 1.0$m in Eq. (3.26)) in order to prevent coincidence of nodes and also to assure a physically acceptable surface shape.

Deformation vectors of all nodes of both fairings that are being optimized point in direction parallel to the spanwise direction of the fin (Fig. (4.25)), which preserves the geometry of the fin. Vectors in nodes, that lie close to the leading edge of the fin point in direction of the leading edge, whereas vectors that lie close to the trailing edge point parallel to the trailing edge direction. Deformation vector field of both junctions are normalized on both junction halves close to the fin, but gradually decrease to zero (Eq. (4.5)) toward the hull and the bulb, respectively. In this way both patches remain tangential to fixed surfaces.

A Stratford criterion (Eq. (3.35)) is used in order to prevent the flow separation in the pressure recovery region. Since the pressure recovery has a convex shape, a value of 0.39 is used as a critical Stratford number in order to constrain the value of G_M (Eq. (3.39)). In this case $a_0 = 100$ is used in order to compute G_M (Eq. (3.39)). Since the pressure recovery region starts at different streamwise

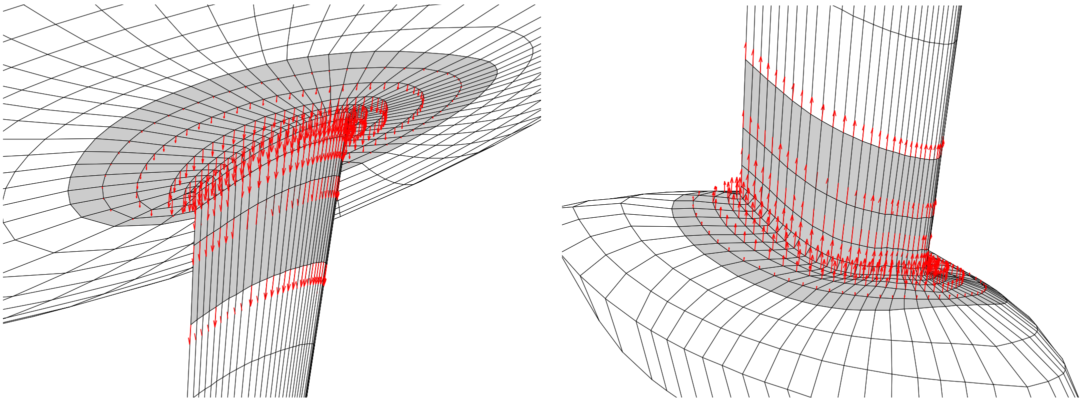
(a) (b)

Figure 4.25: Patches, (a) hull-fin and (b) fin-bulb fairing, that are being optimized (grey panels) and their deformation vector fields scaled by a factor of 0.25 (red vectors).

locations on the body, a linearly decreasing value of the integral from Eq. (3.36) is used for recovery region panels at both fairings. Maxima are at the hull and the bulb and minima at the fin. The minimal integral value of the upper fairing is computed as an integral over the streamline at the fin-fairing junction that runs from the point right next to the stagnation point (on the pressure suction side) to the pressure recovery region. The maximal integral value is, on the other hand, computed as an integral over the streamline that runs from the nose of the hull to the pressure recovery region on the fairing-hull junction. Similar integration is done for the fin-bulb fairing. All integrals are computed after a few steps of optimization (Subsection 3.2.3), averaged over all optimizations at the same angle of attack and used as a constant at all complete optimization procedures at the same angle of attack.

The wake is modeled behind the fin, but stretches also behind the hull and the bulb. The Kutta condition is met only along the trailing edge of the fin. For the hull and the bulb the assumption is made that they don't shed vorticity into the wake, with the exception of a single vortex at the end of the bulb (outer edge of the wake). The doublet distribution in the wake behind them is therefore constant. The wake coincides with the symmetry plane of the body at all observed angles of attack and it stretches approximately thirty fin chord lengths behind the body. A body and a wake doublet distribution, where only a part of the wake can be seen, is for the original shape at 4° angle of attack presented in Fig. (4.26).

A surface optimization of a case at an angle of attack equal to 4° has been

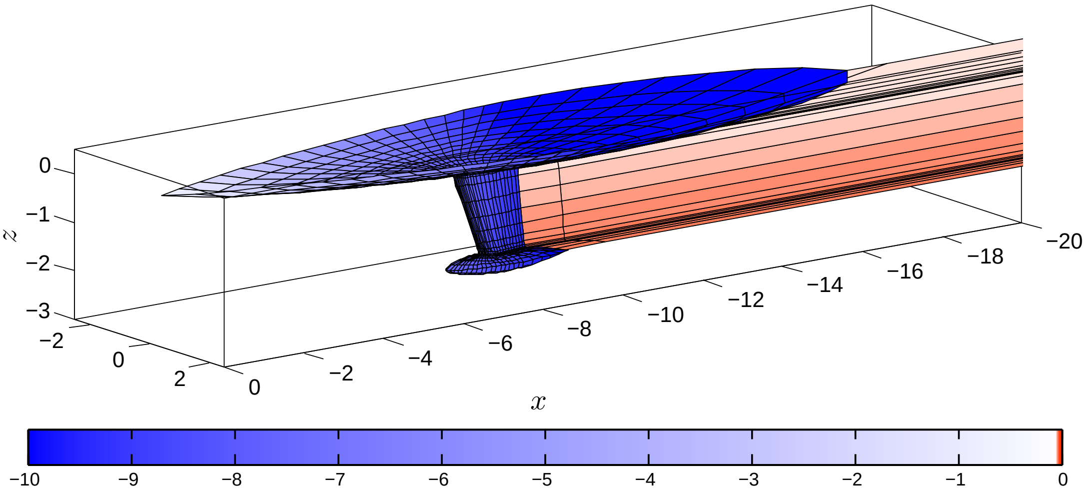

Figure 4.26: Body and wake doublet distribution at $\alpha = 4^\circ$, computed with a panel method. Only a part of the wake is presented.

run at three different surface mesh densities. After a comparison of the relative difference between the initial value of the cost function and its final converged value for different mesh densities (Fig. (4.27(a))), a mesh with a number of panels equal to $N_B = 1780$ has been chosen for all optimization computation. Compared to the finer mesh, the computation times are in this way reduced significantly and the results differ only for a few tenths of a percent.

For the CFD analysis a proper volume mesh density also had to be chosen. For one of the optimal shapes the flow passing the surface at angle of attack equal to 4° has been simulated with three different mesh densities. A relative difference of pressure and friction drag coefficient and lift coefficient between simulations with different mesh densities and a simulation with the highest mesh density is presented in Fig. (4.27(b)). The case with approximately 11 million cells is a reasonable choice for the simulation, since by refining the mesh even further, all the coefficients change for less than 0.4%. The same mesh density was used at the rest of the simulations of the sailboat keel. Since a high Reynolds number Spalart-Allmaras turbulence model was used, the same as at the airplane test case, a value of y^+ was checked after choosing the mesh density. A y^+ body surface distribution is presented in Fig. (4.28). A slice through a mesh coinciding with the symmetry plane is added to the figure. A proper mesh density at the surface is confirmed by the values of y^+.

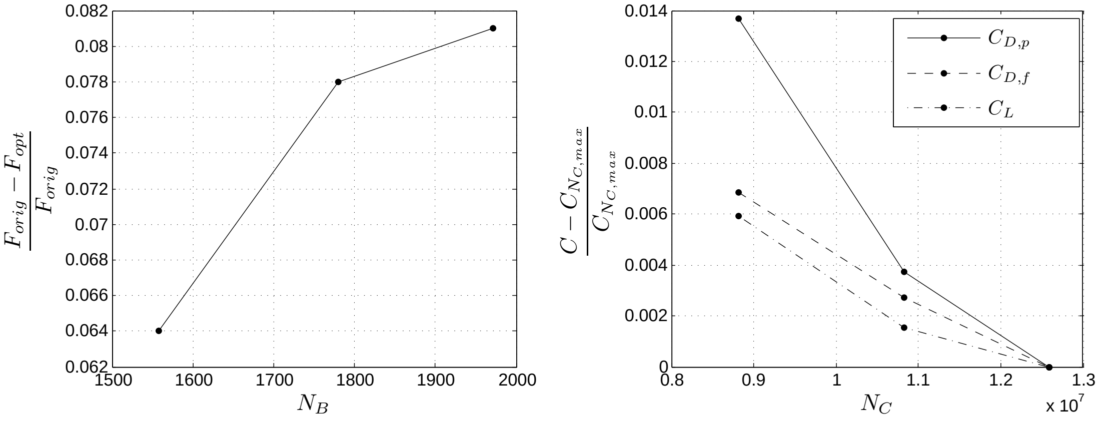

(a) (b)

Figure 4.27: (a) A convergence of a relative difference between initial cost function value and its minimized value, with respect to the body surface mesh density at optimization process. (b) A convergence of the force coefficients with respect to the volume mesh density at CFD analysis.

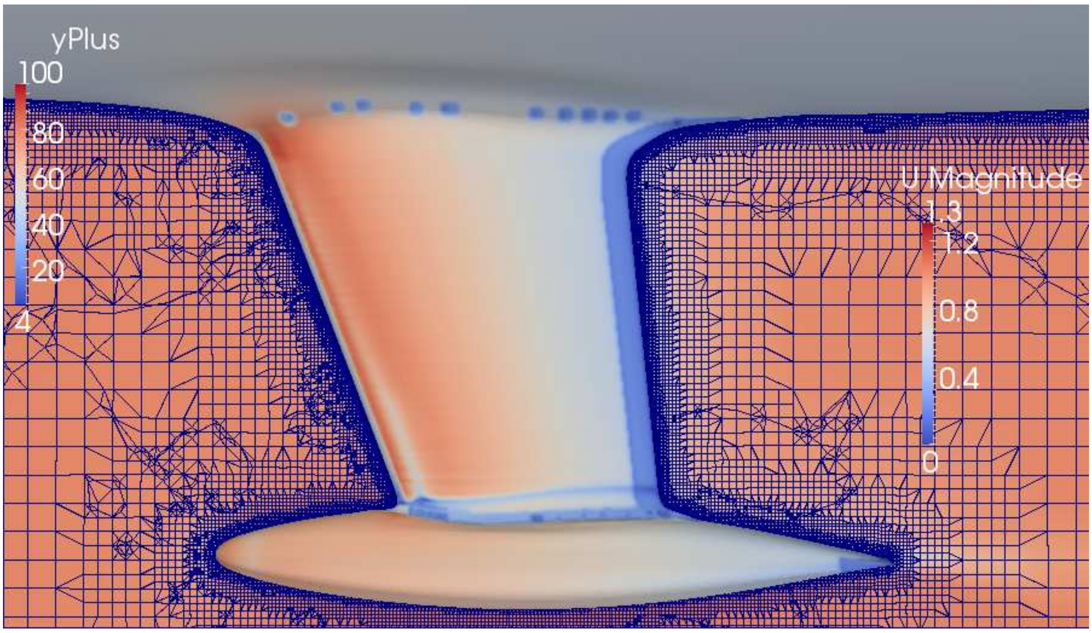

Figure 4.28: y^+ surface distribution and a slice through a mesh of a converged simulation of an airflow around one of the optimized surfaces at 4° angle of attack.

4.4.2 Results

Similar to the previous test case, the optimization of both fairings has been run at three different combinations of two angles of attack, $\alpha_1 = 0°$ and $\alpha_2 = 4°$, where the Eq. (4.6) has been used to compute the weighted sum. Again, if $w = 0$ or $w = 1$, the case is optimized only at the 0° or 4° angle of attack, respectively.

If $w = 0.5$, an optimal surface with a minimal sum of pressure gradient at both angles of attack together is being searched. The original surface was used as an initial condition at all weights. For $w = 0.5$ case different initial conditions were tried, but the optimization always converged to the same solution. The fairings were optimized successively. The upper fairing, that was optimized first, was used afterwards for the optimization of the bottom fairing. Since the patches are more than 1.5m apart in the spanwise direction, a negligible error was made because of this.

Each of the optimized surfaces was evaluated with a CFD analysis. The relative differences of forces and surface area values with respect to the simulation results of the original shape are presented in Fig. (4.29). Compared to the original shape, the total drag was reduced for all solutions. The smallest drag at both angles of attack, can be observed at $w = 1$ solution. For α_1 (Fig. (4.29(a))) the total drag is reduced by 0.5% and for α_2 (Fig. (4.29(b))) by approximately 0.43%. Even though the reductions of the drag are a few tenths of a percent compared to the original shape, the numbers are still notable, because of the large absolute value of the total drag. In Fig. (4.29) the relative changes of the complete body drag are presented. The percentage of the relative reduction of drag for only the fairings is much higher, since they cover only 11% of the total body surface. Besides that, approximately one third of the surface is due to the fin, which doesn't change the shape during optimization. Because of this, even though the relative reduction of the total drag of the whole body has the same

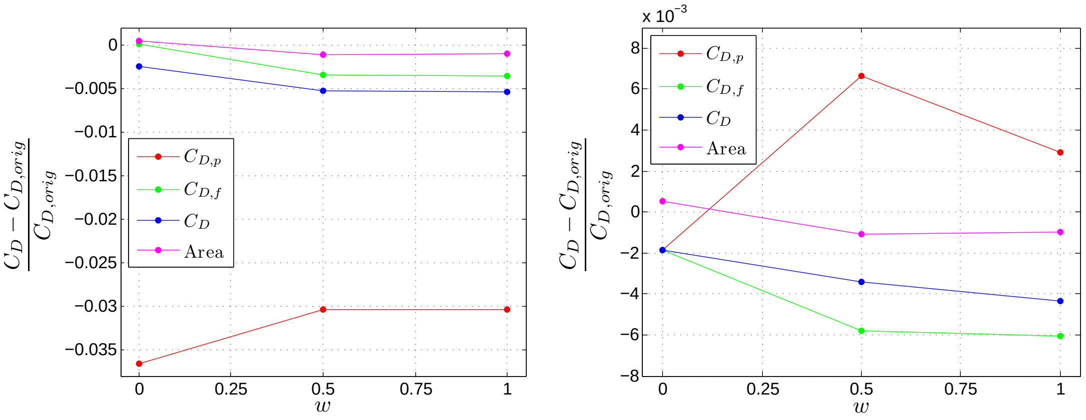

(a) (b)

Figure 4.29: Relative difference of drag and surface area of all optimized surfaces compared to the original surface, computed with OpenFOAM at angle of attack (a) $\alpha_1 = 0°$ and (b) $\alpha_2 = 4°$.

order of magnitude as the mesh density error (Fig. (4.27(b))), the results are still significant.

The absolute value of the friction drag is about 14 times larger than the pressure drag at zero angle of attack and 5 times larger than at an angle of attack equal to 4°. Even though the pressure drag at α_1 reduced by more than 3% for all solutions, the total drag still hardly exceeded the -0.5% change, because of the large contribution of the friction drag. Similar situation can be observed at α_2, where the pressure drag for $w = 0.5$ and $w = 1$ examples even increased compared to the original surface. The minimization of the friction drag component is therefore in this test case much more important compared to the pressure drag in order to optimize the shape of the surface. The surface area of body after each optimization changed for less than one tenth of a percent compared to the original body (Fig. (4.29)). The reduction of the surface area is therefore not the primary reason for friction drag reduction. The major contribution goes to the smoother and on average slower flow around an optimized surface.

During sailing, the sailboat rolls by an angle at which the moments produced by the wind in the sails and by the weight in the bulb equalize [65]. Since typically the sailboat also slightly drifts at an leeway angle (α angle at this test case), as a consequence of the wind, a lift force on the fin is generated, which offers an additional roll angle control of the sailboat. The lift force therefore acts in direction perpendicular to the streamwise and spanwise direction of the fin. Polar curves of the original and all optimized surfaces are presented in Fig. (4.30), where also the change of the lift coefficient can be observed as a consequence of the optimization. A surface area used in coefficient calculations is an area of the planform of the fin, cut at the hull, and stretched tangentially to the middle of the bulb.

The dots in the figure denote the drag and the lift coefficients at angles of attack equal to 0°, 3° and 4°. A fit with a polynomial curve of degree of four for each data group is added to the figure. From the Fig. (4.30) it can be seen, that all optimized surfaces have besides smaller drag also larger lift coefficient at all angles of attack greater than zero. The polar curves therefore shift in a favourable direction. The solution at $w = 1$ has the smallest drag at all lift coefficients, which makes it the one to use at the real case. The solution at $w = 0.5$ almost coincides with the optimal one, which is also in agreement with the data from the Fig. (4.29).

A comparison of a surface pressure distributions between the panel method

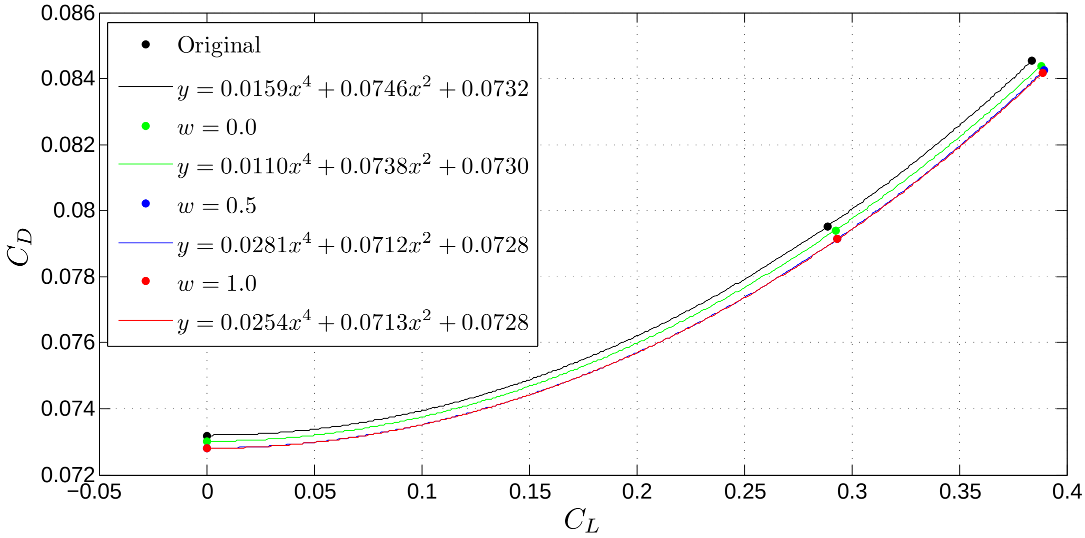

Figure 4.30: Polar plots for an original and optimal surface shapes. The data at different angles of attack is fitted with a polynomial curve of degree of four.

computations and the CFD analysis for the original surface and the optimal surface at $w = 1$ are at zero angle of attack presented in Fig. (4.31) and Fig. (4.32) and at 4° angle of attack in Fig. (4.33) and Fig. (4.34), respectively.

The figures are presented from the pressure "suction side" view. In all CFD computation figures a slice, coinciding with the symmetry plane, with a velocity magnitude distribution and a white line on the surface in a spanwise direction is added in order to have a better perception of the flow passing the body and the surface shape, respectively. The pressure distributions computed with the panel method are as in the previous two test cases (nonseparated flow examples) comparable with the CFD analysis. The surface optimization produced an indent surface at the sides of the hull-fin fairing (e.g. Fig. (4.32(b))), similar to the airplane test case at zero angle of attack (e.g. Fig. (4.20(b))). Since the fin and the hull have much more slender shape compared to the wing and the fuselage from the previous test case, the acceleration around the fairing is not so intense and as a consequence, the indent is not so severe. At the leading and trailing edge, on the other hand, the surface bulged. The sharp corner between the fin and the hull changed into a smooth surface transition, which is additionally presented in the body front view in Fig. (4.35). The interference of the hull and the fin on the flow passing the fairing is in this way reduced, which stabilizes and slows down the flow and indirectly reduces the drag.

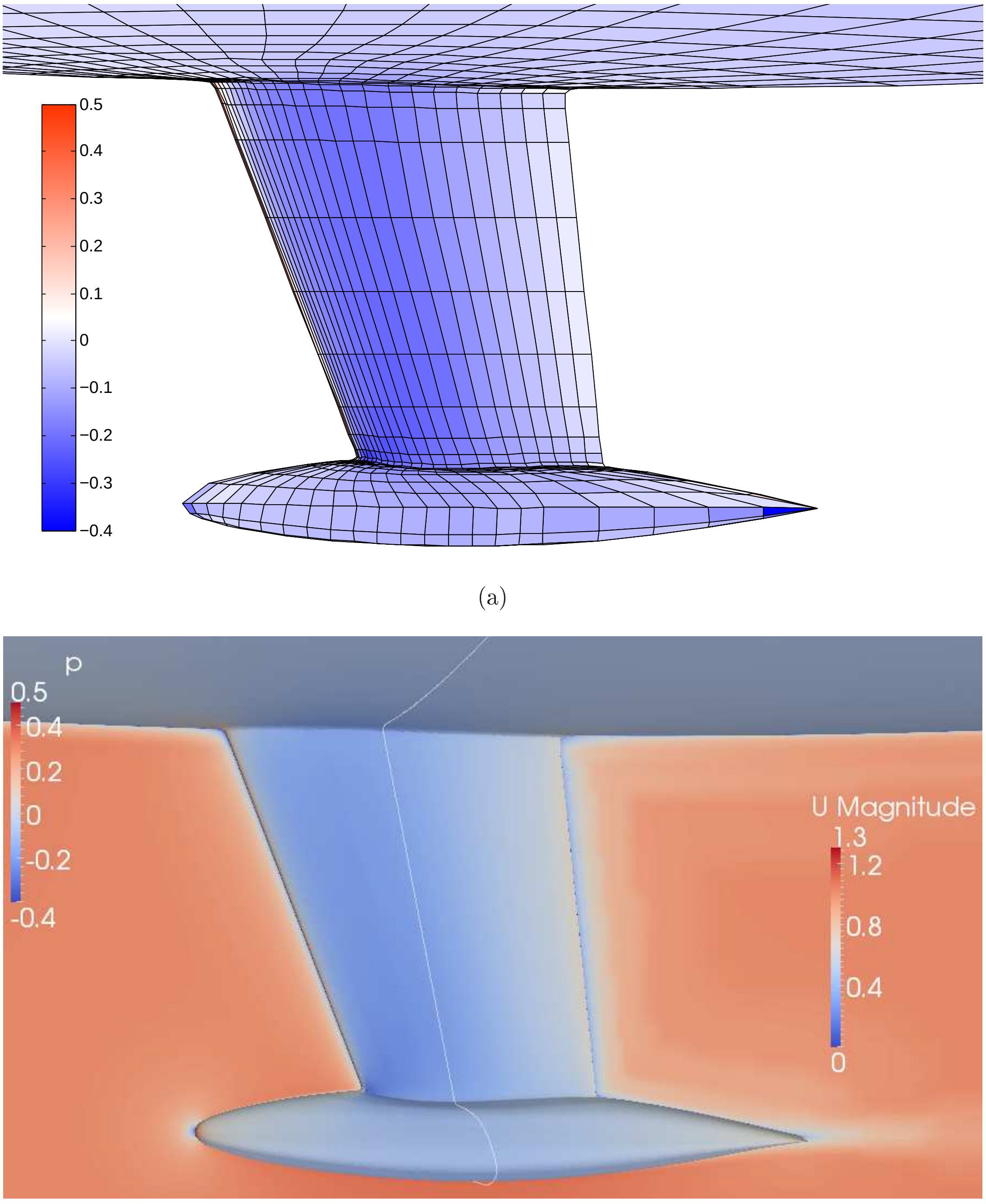

(a)

(b)

Figure 4.31: Surface pressure distribution of an original surface computed with (a) a panel method and (b) a CFD analysis at zero angle of attack.

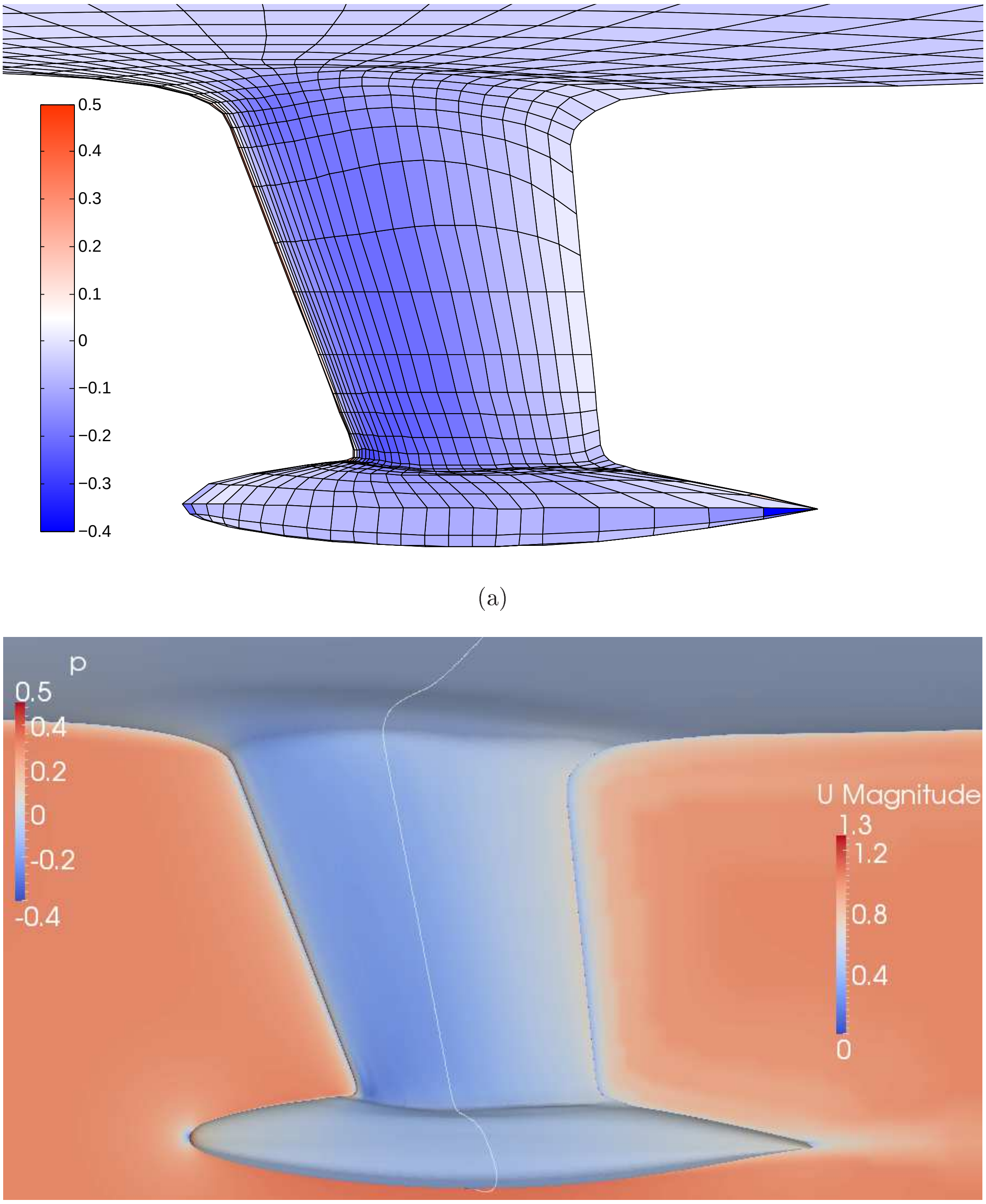

(a)

(b)

Figure 4.32: Surface pressure distribution of an optimal shape at $w = 1.0$, computed with (a) a panel method and (b) a CFD analysis at zero angle of attack.

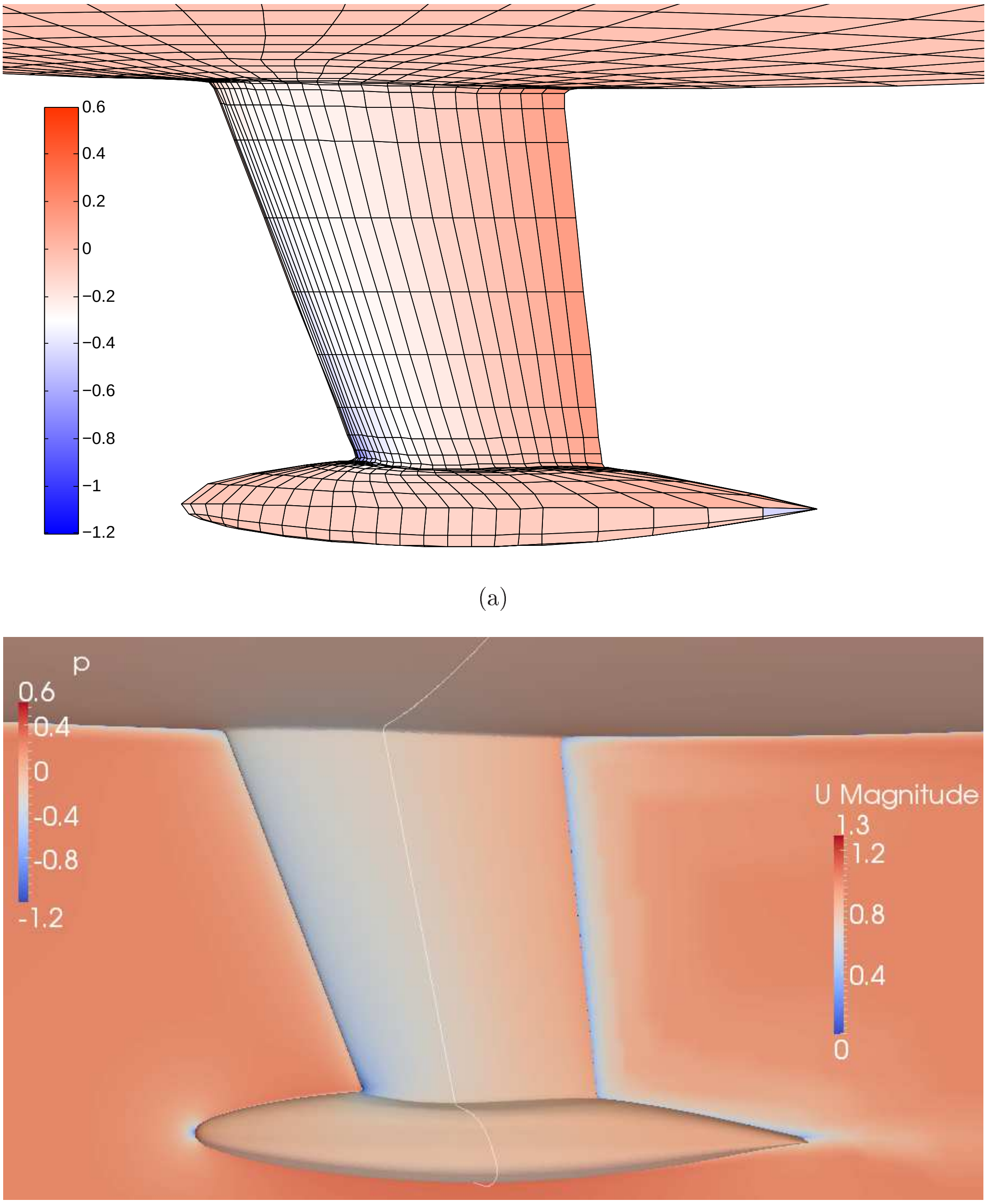

(a)

(b)

Figure 4.33: Surface pressure distribution of an original surface computed with (a) a panel method and (b) a CFD analysis at 4° angle of attack.

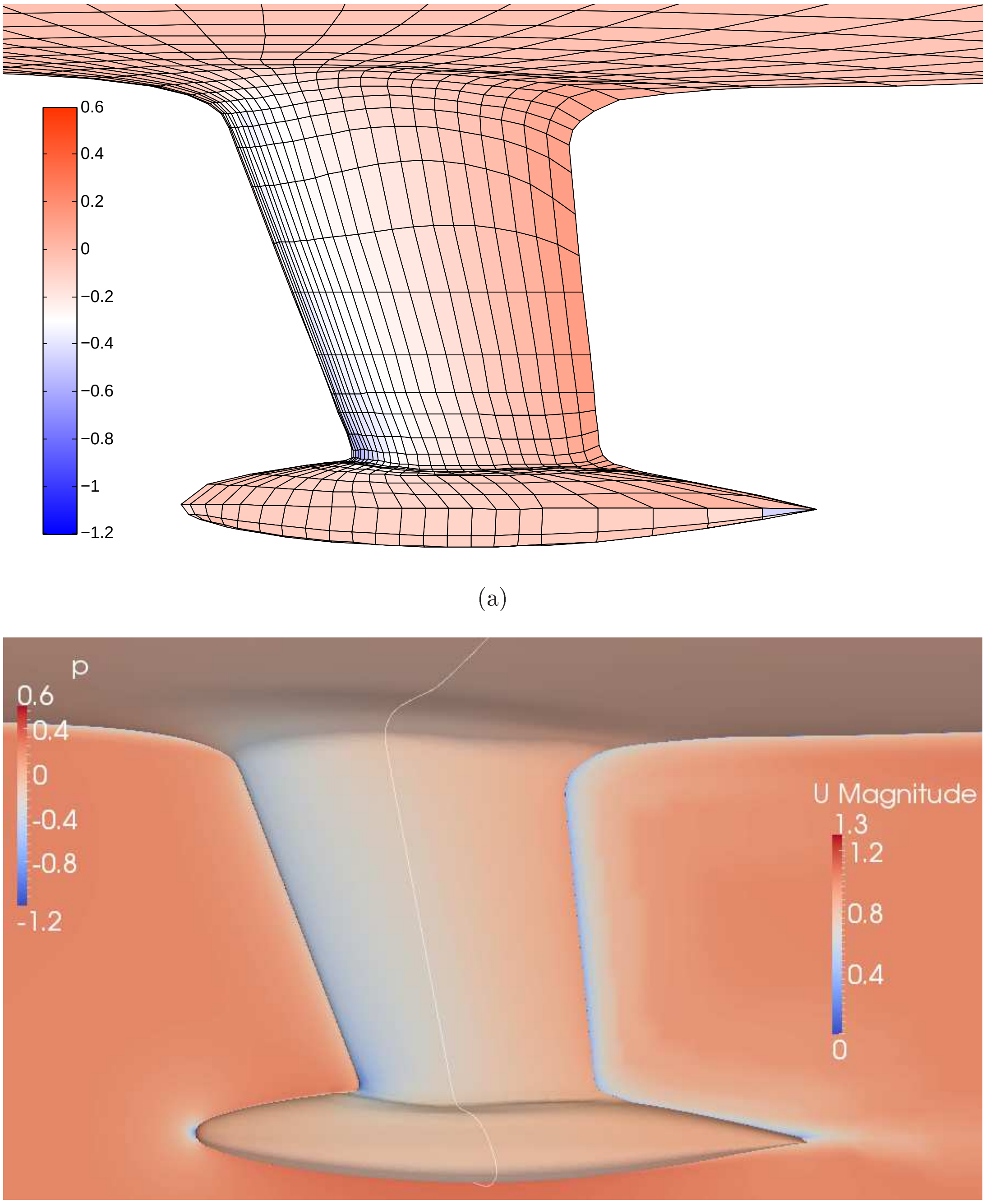

(a)

(b)

Figure 4.34: Surface pressure distribution of an optimal shape at $w = 1.0$, computed with (a) a panel method and (b) a CFD analysis at 4° angle of attack.

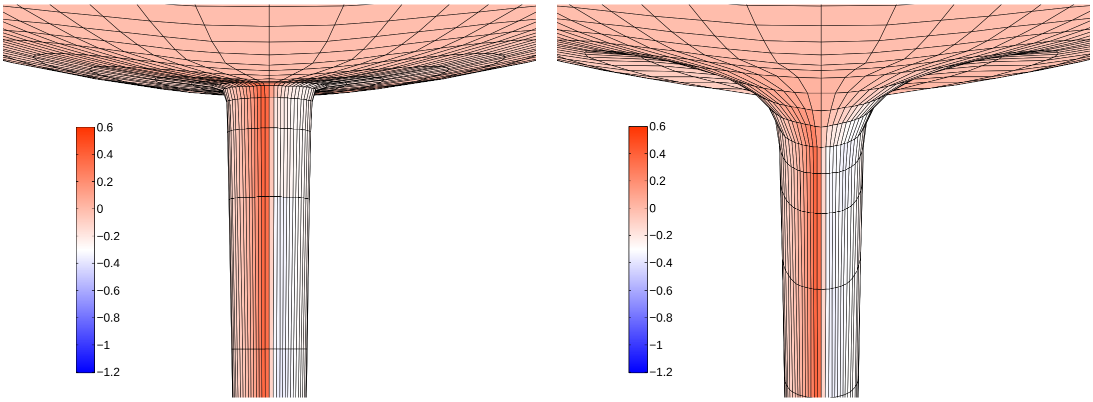

(a) (b)

Figure 4.35: Front view of the pressure surface distribution of the fin-hull fairing at 4° angle of attack computed with the panel method for (a) original surface and (b) optimized surface at $w = 1$.

The surface of the fin-bulb fairing went through similar changes during optimization, but in a much smaller extent. The surface of the original fairing apparently already had a shape close to the optimal one.

Chapter 5

Conclusion

A novel method for automatic optimization of aerodynamic surfaces using pressure based functionals is presented in this work. For this purpose, potential flow is used as a valid approximation of the attached flow passing over an arbitrary body. The outcome of the method is a favourable pressure distribution that indirectly results in a reduced drag. The minimization of a cost function is done using a sequential quadratic programming algorithm.

The proposed panel method that is used to compute pressure distribution is first validated using an example of a potential flow passing a sphere. The relative difference between the panel method solution and the analytical solution is shown to be inversely proportional to the number of panels the surface is discretized into. The proposed optimization method is then used in three conceptually different test cases. All cases are evaluated with results obtained by CFD analysis.

In the case of optimization of a fairing, enclosing a human powered vehicle, it is shown that the transition from laminar to turbulent flow is delayed and the boundary layer at the pressure recovery region is thinned. In this way, the total drag of the bicycle is reduced by more than 10%. In the second test case, where the fairing of the wing-fuselage junction on an airplane is optimized, a massive root flow separation at moderate angle of attack is eliminated. The total drag at angle of attack equal to 8° is reduced by more than 16.5%. Even though a great importance of the initial condition is shown in this case, the shape of the fuselage at the fairing is still in most optimization results indent in order to decelerate the flow. The resulting surface shape resembles similar test cases in the literature, as was presented in Chapter 4. The last test case represents an optimization of a bulb keel of a sailboat, where both fairings (hull-fin and fin-bulb) are being treated. In this high Re case the total drag is reduced by 0.5% and 0.43% at

0° and 4° angle of attack, respectively. The primary reason for reduction is a smoother and on average slower flow around optimized surfaces.

With the proposed method, satisfactory results can be obtained such that lower drag on the aerodynamic surfaces can be anticipated. The method is conceptually simple and computationally low demanding. Even though a structured mesh is used in present work, the method can be equivalently used also with an arbitrary unstructured mesh, which enables one to rearrange the panels in order to reduce their number. Beside geometrical constraints and Stratford criterion other constraints can be easily incorporated into the method such as e.g. a fixed wing lift, wing bending moment, surface area etc. This favourable pressure distribution based method can also be extended to reshape e.g. a wing in order to produce a maximal lift coefficient or even a shock-free surface [40] in case of a transonic flight. The method therefore enables one to tackle different aerodynamic problems with minor modifications.

On the other hand, the method still has some limitations that need to be adopted such as a need for a predefined patch and deformation vector field, a possibility of intersection of panels during the optimization process and a lack of information about the drag force. The latter drawback consequently means a need for a CFD evaluation of each optimization result in order to estimate the force with which the flow acts on the body. A logical upgrade of the method is therefore an introduction of the boundary layer equations into the method, which enables one to directly estimate displacement thickness and drag force [35]. The latter can be then used as an additional functional that in a combination with existing pressure based functionals offer an even wider spectrum of possible cost functions that need to be further researched and tested.

Pressure distribution resulting from the optimization process using the existing method can be simply explained as is shown in present work. By upgrading the method, on the other hand, one needs to realize that the conceptual simplicity of the method and consequently the understanding of results is being lost. Moreover, the drag computed with the boundary layer equations rely on the exactness of the turbulence model incorporated in the equations, whereas the pressure distribution is largely model independent.

Even though the results of the present method represent an improvement regarding the pressure distribution and consequently the drag force of the body, it would be also interesting to compare them with other optimization methods.

Original contributions in the present dissertation are

- A novel three dimensional potential flow optimization method where pressure based functionals are used to shape optimal aerodynamic surfaces.
- Functionals are found that, when minimized, reduce the growth of the Tollmien-Schlichting waves and cross-flow instabilities and consequently promote laminar boundary layer.
- An implementation of the Stratford separation criterion as a constraint in the three dimensional optimization procedure using a "soft" maximum principle and Heaviside pressure function weight.
- A new principle of reshaping the aerodynamic surface where a constant deformation vector field multiplied by the variable Bézier surface is added to the original shape and where the Bézier surface control points represent also the optimization variables.

The advancement of the science and engineering as a consequence of this dissertation is therefore:

- A fast, automatic, conceptually simple, and computationally low demanding optimization method that can be used already in the preliminary phase of aircraft design.
- The method enables one to design aerodynamic surfaces that promote laminar boundary layers and prevent flow separation in the pressure recovery regions together with different geometrical constraints.
- The usage and the efficiency of this simple method was shown on different test cases taken from real life engineering applications.

During authors graduate studies a paper with a related topic was published in the Journal of Aircraft

- Andrejašič, M., and Veble, G., “Shape Optimization of Nonplanar Lifting Surfaces and Planar-Nonplanar Break Points,” *Journal of Aircraft*, Vol. 50, No. 3, 2013, pp. 798-806.

The present work will be submitted as a paper to the Journal of Aircraft as

- Andrejašič, M., and Veble, G., “Optimization of Aerodynamic Surfaces using Pressure Based Functionals.” (Will be submitted in 2014)

Bibliography

[1] Miele, A., *Theory of Optimum Aerodynamic Shapes: External Problems in the Aerodynamics of Supersonic, Hypersonic, and Free-Molecular Flows*, Academic Press, New York, 1965.

[2] Lions, J. L., *Optimal Control of Systems Governed by Partial Differential Equations*, Springer-Verlag, New York, 1971, Translated by S.K. Mitter.

[3] Pironneau, O., *Optimal Shape Design for Elliptic Systems*, Springer-Verlag, New York, 1984.

[4] Jameson, A., "Aerodynamic Design via Control Theory," NASA CR-181749, 1988.

[5] Blackwell, J. A., Jr., "Numerical Method to Calculate the Induced Drag or Optimum Loading for Arbitrary Non-Planar Aircraft," NASA SP-405, May 1976.

[6] Kroo, I. M., "Design and Analysis of Optimally-Loaded Lifting Systems," AIAA Paper 84-2507, October 1984.

[7] Jansen, P. W., Perez, R. E., and Martins, J. R. R. A., "Aerostructural Optimization of Nonplanar Lifting Surfaces," *Journal of Aircraft*, Vol. 47, No. 5, September-October 2010, pp. 1490-1503.
doi:10.2514/1.44727

[8] Andrejašič, M., and Veble, G., "Shape Optimization of Nonplanar Lifting Surfaces and Planar-Nonplanar Break Points," *Journal of Aircraft*, Vol. 50, No. 3, 2013, pp. 798-806.
doi:10.2514/1.C031991

[9] Veble, G., "A Parameter Free Cost Function for Multi-Point Low Speed Airfoil Design," CMES: Computer Modeling in Engineering & Sciences, Vol.

36, No. 3, 2008, pp. 243-260.
doi:10.3970/cmes.2008.036.243

[10] Gamboa, P., Vale, J., Lau, F. J. P., and Suleman, A., “Optimization of a Morphing Wing Based on Coupled Aerodynamic and Structural Constraints,” AIAA Journal, Vol. 47, No. 9, 2009, pp. 2087-2104.
doi:10.2514/1.39016

[11] Dulikravich, G. S., “Aerodynamic Shape Design and Optimization: Status and Trends,” *Journal of Aircraft*, Vol. 29, No. 6, 1992, pp. 1020-1026.
doi:10.2514/3.46279

[12] Newman, J. C., III, Taylor, A. C., III, Barnwell, R. W., Newman, P. A., and Hou, G. J.-W., “Overview of Sensitivity Analysis and Shape Optimization for Complex Aerodynamic Configurations,” *Journal of Aircraft*, Vol. 36, No. 1, 1999, pp. 87-96.
doi:10.2514/2.2416

[13] Jameson, A., “CFD for Aerodynamic Design and Optimization: Its Evolution over the Last Three Decades,” *16th AIAA Computer Fluid Dynamics Conference*, Orlando, FL, USA, 2003.

[14] Jameson, A., Martinelli, L., and Pierce, N. A., “Optimum Aerodynamic Design using the Navier Stokes Equation,” *Theoret. Comput. Fluid Dynamics*, Vol. 10, Iss. 1-4, 1998, pp. 213-237.
doi:10.1007/s001620050060

[15] Leoviriyakit, K., Kim, S., and Jameson, A., “Aero-Structural Wing Planform Optimization Using the Navier-Stokes Equations,” *10th AIAA/ISSMO Multidisciplinary Analysis and Optimization Conference*, Albany, NY, USA, 2004.
doi:10.2514/6.2004-4479

[16] Peigin, S., and Epstein, B., “Robust Drag Minimization of Aerodynamic Wings in Engineering Environment,” *Journal of Aircraft*, Vol. 43, No. 4, 2006, pp. 1195-1204.
doi:10.2514/1.18634

[17] Epstein, B., Jameson, A., Peigin, S., Roman, D., Harrison, N., and Vassberg, J., “Comparative Study of Three-Dimensional Wing Drag Minimization by

Different Optimization Techniques," *Journal of Aircraft*, Vol. 46, No. 2, 2009, pp. 526-541.
doi:10.2514/1.38216

[18] Reuther, J. J., Cliff, S. E., Hicks, R. M., and van Dam, C. P., "Practical Design Optimization of Wing/Body Configurations Using the Euler Equations," *10th AIAA Applied Aerodynamics Conference*, Palo Alto, CA, USA, 1992, pp. 330-342.
doi:10.2514/6.1992-2633

[19] Reuther, J., Jameson, A., Farmer, J., Martinelli, L., and Saunders, D., "Aerodynamic Shape Optimization of Complex Aircraft Configurations via an Adjoint Formulation," *34th Aerospace Sciences Meeting and Exhibit*, Reno, NV, USA, 1996.
doi:10.2514/6.1996-94

[20] Reuther, J. J., Jameson, A., Alonso, J. J., Rimlinger, M. J., and Saunders, D., "Constrained Multipoint Aerodynamic Shape Optimization Using an Adjoint Formulation and Parallel Computers, Part 1," *Journal of Aircraft*, Vol. 36, No. 1, 1999, pp. 51-60.
doi:10.2514/2.2413

[21] Leoviriyakit, K., and Jameson, A., "Aero-Structural Wing Planform Optimization, " *42st Aerospace Sciences Meeting and Exhibit*, Reno, Nevada, USA, 2004.
doi:10.2514/6.2004-29

[22] Katz, J., and Plotkin, A., *Low-Speed Aerodynamics*, 2nd edition, Cambridge University Press, UK, 2001.

[23] Ragab, S. A., "Shape Optimization of Surface Ships in Potential Flow Using an Adjoint Formulation," *AIAA Journal*, Vol. 42, No. 2, 2004, pp. 296-304.
doi:10.2514/1.9094

[24] Sevant, N. E., Bloor, M. I. G., and Wilson, M. J., "Aerodynamic Design of a Flying Wing Using Response Surface Methodology," *Journal of Aircraft*, Vol. 37, No. 4, 2000, pp. 562-569.
doi:10.2514/2.2665

[25] Wang, X., and Shan, X., "Shape Optimization of Stratosphere Airship," *Journal of Aircraft*, Vol. 43, No. 1, 2006, pp. 283-287.
doi:10.2514/1.18295

[26] Dodbele, S., van Dam, C. P., Vijgen, P. M. H. W., and Holmes, B. J., "Shaping of Airplane Fuselages for Minimum Drag," *Journal of Aircraft*, Vol. 24, 1987, pp. 298-304.
doi:10.2514/3.45444

[27] Ahuja, V., and Hartfield, Jr., R. J., "Aero-Propulsive Optimization of the Boeing-737 Wing-Engine Integrated Geometry using Smart Panel Approaches and Modified Potential Theory," *29th AIAA Applied Aerodynamics Conference*, Honolulu, Hawaii, 2011.
doi:10.2514/6.2011-3805

[28] Hess, J. L., "Calculations of Potential Flow about Bodies of Revolution having Axes Perpendicular to the Free-Stream Direction," *Journal of the Aerospace Sciences*, Vol. 29, No. 6, 1962, pp. 726-742.

[29] Hess, J. L., and Smith, A. M., "Calculations of Nonlifting Potential Flow about Arbitrary Three-Dimensional Bodies," *Journal of Ship Research*, Vol. 8, 1964, pp. 22-44.

[30] Cheng, A. H. D., and Cheng, D. T., "Heritage and Early History of the Boundary Element Method," *Engineering Analysis with Boundary Elements*, Vol. 29, 2005, pp. 268-302.

[31] Chen, C. S., Karageorghis, A., and Smyrlis, Y. S., *The Method of Fundamental Solution - A Meshless Method*, Dynamic Publishers, Inc., Atlanta, USA, 2008.

[32] Šarler, B., "Solution of Potential Flow Problems by the Modified Method of Fundamental Solutions: Formulations with the Single Layer and the Double Layer Fundamental Solutions," *Engineering Analysis with Boundary Elements*, Vol. 33, Iss. 12, 2009, pp. 1374-1382.
doi:10.1016/j.enganabound.2009.06.008

[33] Chen, W., and Wang, F. Z., "A Method of Fundamental Solutions without Fictitious Boundary," *Engineering Analysis with Boundary Elements*, Vol.

34, Iss. 5, 2010, pp. 530-532.
doi:10.1016/j.enganabound.2009.12.002

[34] Nocedal, J., and Wright, S. J., *Numerical Optimization*, 2nd edition, Springer, USA, 2006.

[35] Schlichting, H., and Gersten, K., *Boundary Layer Theory*, 8th revisited and enlarged edition, Springer-Verlag, Germany, 2000.

[36] Secanell, M., and Suleman, A., "Sequential Optimization Algorithms for Aerodynamic Shape Optimization," *10th AIAA/ISSMO Multidisciplinary Analysis and Optimization Conference*, Albany, New York, USA, 2004.
doi:10.2514/6.2004-4631

[37] Secanell, M., and Suleman, A., "Numerical Evaluation of Optimization Algorithms for Low-Reynolds-Number Aerodynamic Shape Optimization," *AIAA Journal*, Vol. 43, 2005, pp. 2262-2267.
doi:10.2514/1.12563

[38] Prandtl, L., Über Flüssigkeitsbewegungen bei sehr kleiner Reibung. Verhandlg. III. Intern. Math. Kongr. Heidelberg, 484-491, 1904. See also: L. Prandtl: Gesammelte Abhandlungen zur angewandten Mechanik, Hydro- und Aerodynamik, in 3 Teilen (1961).

[39] Kroo, I. M., "Drag due to Lift: Concepts for Prediction and Reduction," *Annual Review of Fluid Mechanics*, Vol. 33, January 2001, pp. 587–617.
doi:10.1146/annurev.fluid.33.1.587

[40] Anderson, Jr., J. D., *Fundamentals of aerodynamics*, 4th edition, McGraw-Hill, Inc., New York, 2007.

[41] Blasius, H., Grenzschichten in Flüssigkeiten mit kleiner Reibung. Z. Math. Physik, Bd. 56, 1-37. Engl. translation in NACA-TM-1256, 1908.

[42] Dini, P., and Maughmer, M. D., "Locally Interactive Laminar Separation Bubble Mode," *Journal of Aircraft*, Vol. 31, 1994, pp. 802-810.
doi:10.2514/3.46564

[43] Ovchinnikov, V., Choudhari, M. M., and Piomelli, U., "Numerical Simulations of Boundary-Layer Bypass Transition due to High-Amplitude Free-Stream Turbulence," *J. Fluid Mech.*, Vol. 613, 2008, pp. 135-169.
doi:10.1017/S0022112008003017

[44] Morkovin, M. V., "Recent Insights into Instability and Transition to Turbulence in Open-Flow Systems - Final Report," NASA-CR-181693, 1988.

[45] Reshotko, E., "Progress, Accomplishments and Issues in Transition Research," AIAA Paper 97-1815, 1997.
doi: 10.2514/6.1997-1815

[46] Saric, W. S., Reed, H. L., and White, E. B., "Stability and Transition of Three-Dimensional Boundary Layers," *Annu. Rev. Fluid Mech.*, Vol. 35, 2003, pp. 413-440.
doi: 10.1146/annurev.fluid.35.101101.161045

[47] Schrader, L. U., Amin, S., and Brandt, L., "Transition to Turbulence in the Boundary Layer over a Smooth and Rough Swept Plate Exposed to Free-Stream Turbulence," *J. Fluid Mech.*, Vol. 646, 2010, pp. 297-325.
doi:10.1017/S0022112009993284

[48] Lewellen, D. C., Lewellen, W. S., Poole, L. R., DeCoursey, R. J., Hansen, G. M., Hostetler, C. A., and Kent, G. S., "Large-Eddy Simulations and Lidar Measurements of Vortex-Pair Breakup in Aircraft Wakes," *AIAA Journal*, Vol. 36, 1998, pp. 1439-1445.
doi:10.2514/2.535

[49] Sinigoj, A. R., *Osnove Elektromagnetike*, 3rd edition, Fakulteta za elektrotehniko, Ljubljana, Slovenia, 1999.

[50] Epton, M. A., and Magnus, A. E., "PAN AIR - A Computer Program for Predicting Subsonic or Supersonic Linear Potential Flows about Arbitrary Configurations Using a Higher Order Panel Method, Vol. I. Theory Document (Version 3.0)," NASA CR-3251, 1990.

[51] Hess, J. L., "Calculation of Potential Flow About Arbitrary Three-Dimensional Lifting Bodies," McDonnell Douglas Rept. No MDC J5679-01, 1972.

[52] Farin, G., *Curves and Surfaces for CAGD: A Practical Guide*, 5th edition, Morgan Kaufmann Publishers, San Francisco, USA, 2001.

[53] Stratford, B. S., "The Prediction of Separation of the Turbulent Boundary Layer," *J. Fluid Mech.*, Vol. 5, Iss. 1, 1959, pp. 1-16.
doi:10.1017/S0022112059000015

[54] Chmielewski, G. E. , “Boundary-Layer Considerations in the Design of Aerodynamic Contractions, “ *Journal of Aircraft*, Vol. 11, 1974, pp. 435-438. doi:10.2514/3.60363

[55] Gill, P. E., Murray, W., and Wright, M. H., *Numerical Linear Algebra and Optimization, Vol. 1,* Addison Wesley, 1991.

[56] Walters, D. K., and Cokljat, D., “A Three-Equation Eddy-Viscosity Model for Reynolds-Averaged Navier–Stokes Simulations of Transitional Flow,” *J. Fluids Eng.*, Vol. 130, Iss. 12, 2008, pp. 1-14
doi:10.1115/1.2979230

[57] Spalart, P. R., and Allmaras, S. R., “A one-equation turbulence model for aerodynamic flows,” AIAA Paper 92-0439, 1992.
doi:10.2514/6.1992-439

[58] Paciorri, R., Di Mascio, A., and Favini, B., “A Comparative Study of Turbulence Models for Junction Flow, “ *32nd AIAA Fluid Dynamics Conference and Exhibit*, St. Louis, Missouri, USA, 2002.
doi:10.2514/6.2002-2964

[59] Maughmer, M., Hallman, D., Ruszkowski, R., Chappel, G., and Waitz, I., “Experimental Investigation of Wing/Fuselage Integration Geometries,” *Journal of Aircraft*, Vol. 26, 1989, pp. 705-711.
doi:10.2514/3.45828

[60] Van Oudheusden, B. W., Steenaert, C. B., and Boermans, L. M. M., “Attachment-Line Approach for Design of a Wing-Body Leading-Edge Fairing,” *Journal of Aircraft*, Vol. 41, 2004, pp. 238-246.
doi:10.2514/1.353

[61] Li, C., Ye, Z., and Wang, G., “Simulation of Flow Separation at the Wing-Body Junction with Different Fairings,” *Journal of Aircraft*, Vol. 45, 2008, pp. 258-266.
doi:10.2514/1.26638

[62] Song, W., and Lv, P., “Two-Level Wing-Body-Fairing Optimization of a Civil Transport Aircraft,” *Journal of Aircraft*, Vol. 48, 2011, pp. 2114-2121.
doi:10.2514/1.C031472

[63] Raymer, D. P., *Aircraft Design: A Conceptual Approach*, 4th edition, AIAA Education Series, Virginia, USA, 2006.

[64] Cebeci, T., and Cousteix, J., *Modeling and Computation of Boundary-Layer Flows*, 2th revisited and enlarged edition, Horizons Publishing, Long Beach, California, USA, 2005.

[65] Fossati, F., *Aero-Hydrodynamics and the Performance of Sailing Yachts: The Science Behind Sailboats and Their Design*, Adlard Coles Nautical, London, UK, 2009.